Experimental growth of Schrödinger kitten states

Dissertation
zur Erlangung des Doktorgrades
an der Fakultät für Mathematik, Informatik und Naturwissenschaften
Fachbereich Physik
der Universität Hamburg

vorgelegt von

Julian Göttsch

Hamburg

2022

Gutachter der Dissertation:	Prof. Dr. Roman Schnabel Prof. Dr. Henning Moritz
Zusammensetzung der Prüfungskommission:	Prof. Dr. Roman Schnabel Prof. Dr. Henning Moritz Prof. Dr. Ludwig Mathey Prof. Dr. Peter Schmelcher Prof. Dr. Oliver Gerberding
Vorsitzender der Prüfungskommission:	Prof. Dr. Ludwig Mathey
Datum der Disputation:	12.04.2022
Vorsitzender des Fach-Promotionsausschusses PHYSIK:	Prof. Dr. Wolfgang Hansen
Leiter des Fachbereichs PHYSIK:	Prof. Dr. Günter H. W. Sigl
Dekan der Fakultät MIN:	Prof. Dr. Heinrich Graener

Kurzfassung

Im Bereich der Quantenphysik werden nichtklassische Zustände wie Überlagerung und Verschränkung untersucht. Ein Beispiel für eine Überlagerung ist der quantenoptische Schrödinger-Katzen-Zustand, der als Qubit im Bereich der Quanteninformatik verwendet werden könnte. Eine Möglichkeit, einen solchen Zustand zu erzeugen, ist die Subtraktion eines einzelnen Photons von einem schwach gequetschten Lichtzustand. Allerdings ist die resultierende Amplitude α dieses Zustands sehr klein und liegt bei nur ungefähr 1. Für eine Anwendung als Qubit ist ein α über 2 erforderlich. Dies kann erreicht werden, indem die erzeugten Katzenzustände auf einem 50/50 Strahlteiler mit 2 Wiederholungen probabilistisch überlagert werden. Ein solches Experiment erfordert einen anspruchsvollen Aufbau mit 4 Quetschlichtquellen und einer 4 übereinstimmenden Einzelphotonendetektion, um den Erfolg des Wachsens anzukündigen. In dieser Arbeit wurde ein anderer Ansatz getestet, der es erlaubt, das Ergebnis des zuvor beschriebenen Experiments mit nur einer Quetschlichtquelle und einem Einzelphotonendetektor zu emulieren. Dazu wurde eine 8-Port-Homodyn-Detektion eines Katzenzustands mit einem α von 1,1 experimentell realisiert. Die Überlagerung an einem 50/50 Strahlteiler mit 2 Wiederholungen wurde in einer Datennachbearbeitung durchgeführt. Es konnte ein Katzenzustand mit einem α von 2,6 emuliert werden. Damit wurde die erforderliche Schwelle für Qubit-Anwendungen erreicht, aber der Katzenzustand ist nur in Form von bereits gemessenen Datenpunkten verfügbar, die in einem Computer gespeichert sind. Ob unsere emulierten Katzenzustände für weitere Anwendungen genutzt werden können, wird derzeit untersucht. Der Aufbau für die Erzeugung der Katzenzustände wird für ein zukünftiges Projekt über Verschränkungsdestillation wiederverwendet, welches den Abstand für die Quantenschlüsselverteilung im Bereich der Quantenkryptographie verbessern könnte.

Abstract

Quantum physics allows to investigate nonclassical states like superpositions and entanglement. One example for a superposition is the quantum optical Schrödinger cat state, which might be used as a qubit in the area of quantum computation. One way of producing such a state is the subtraction of a single photon from a weakly squeezed state of light. The resulting amplitude α of this state is small and just around 1. For an application as qubit, an α above 2 is required. This can be achieved by probabilistically overlapping the created cat states on a 50/50 beam splitter with 2 iterations. Such an experiment needs a challenging setup with 4 squeezed-light sources and a 4 coincident single photon detection for heralding success of the growth. In this thesis another approach was tested, which allows to emulate the outcome of the previously described experiment by using only 1 squeezed-light source and 1 single photon detector. For that an 8-port homodyne detection of a cat state with an α around 1.1 was experimentally realized. The interference on a 50/50 beam splitter with 2 iterations was done in post processing. It was possible to emulate a cat state with an α around 2.6. Hence the required threshold for qubit applications was reached, but the cat state is only available in form of already measured data points inside a computer. If our emulated cat states can be used for further applications is under investigation. The cat state setup will be repurposed for a future project about entanglement distillation, which might be able to improve the possible distance for quantum key distribution in the field of quantum cryptography.

Contents

List of Figures

List of Abbreviations

APD	**A**valanche **p**hoto **d**iode
BHD	**B**alanced **h**omodyne **d**etector
BS	**B**eam **s**plitter
dB	**D**eci**b**el
DBS	**D**ichroic **b**eam **s**plitter
DMC	**D**iagnostic **m**ode **c**leaner
EOM	**E**lectro **o**ptic **m**odulator
FC	**F**ilter **c**avity
FSR	**F**ree **s**pectral **r**ange
FWHM	**F**ull **w**idth at **h**alf **m**aximum
LO	**L**ocal **o**scillator
MC	**M**ode **c**leaner
PBS	**P**olarizing **b**eam **s**plitter
PD	**P**hoto **d**iode
PID	**P**roportional **i**ntegral **d**erivative
PIN	**P**ositive **i**ntrinsic **n**egative
PS	**P**hase **s**hifter
RBW	**R**esolution **b**and**w**idth
SHG	**S**econd **h**armonic **g**eneration
SNSPD	**S**uperconducting **n**anowire **s**ingle **p**hoton **d**etector
SQZ	**Sq**uee**z**er
UNBF	**U**tra **n**arrow **b**andpass **f**ilter
VBW	**V**ideo **b**and**w**idth

Chapter 1

Introduction

In 1935 an astonishing thought experiment was published by Erwin Schrödinger to demonstrate the strange properties of quantum physics [1]. This thought experiment is called "Schrödinger's cat" and describes a cat which is dead and alive at the same time. Figure 1.1 visualizes the thought experiment of Schrödinger's cat.

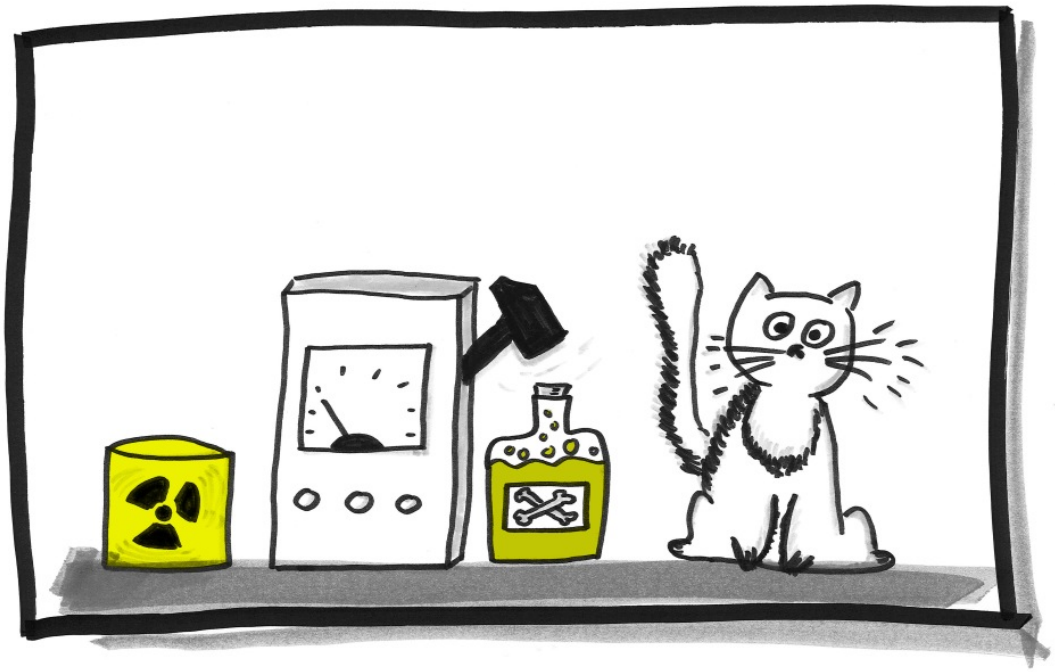

Figure 1.1: Schrödinger's cat. A cat is placed inside a box, which is completely isolated from the environment. Additionally, a toxic substance is placed inside the box, which can kill the cat. The toxic substance will be released by an atomic decay, which is a random event. Therefore, without a measurement process it is unknown if the atom is decayed and the cat is dead or if the atom is not decayed and the cat is alive. Hence, the cat is in a superposition of dead and alive until someone opens the box to observe the state of the cat. In the moment of observation, the superposition collapses and the cat is either dead or alive. Picture received from Joachim Herz Stiftung / Jenny Meßinger-Koppelt.

To achieve this superposition of two different states, the cat is placed inside a box, which is completely isolated from the environment. Inside the box is also a toxic substance, which can be released by a mechanism, which is triggered by a random event like an atomic decay. This leads to two possibilities: the atom is decayed and the cat is dead or the atom is not decayed and the cat is alive. Without a measurement process, the state of the cat is unknown and can be interpreted as a superposition of dead and alive. If someone opens the box, to observe the state of the cat, the superposition collapses and the cat is either dead or alive. Of course, it is not possible to isolate a living object completely from the environment because, therefore, ultra cold temperatures and an ultra high vacuum are needed, which cannot be realized for a living object. Hence, the Schrödinger's cat remains a thought experiment and cannot be done in a real experiment. But quantum physics allows to create other superposition states in an experimental way, for example, by using atom-light interactions [2][3][4].

In this thesis a method is shown to create a quantum optical cat state, which is defined as a superposition of two coherent states $|\alpha\rangle$ with opposite phases [5, p.174]. The basic idea is to subtract a single photon from a weakly squeezed state of light. Therefore, a small part of the weakly squeezed state is tapped off to a single photon detector, which is used as a trigger to do a conditional measurement. This procedure was already done in [6][7] and delivered a state with a high fidelity to a cat state. The amplitude α is only in the order around 1. Hence, it is a very small cat state, which is sometimes labeled as "Schrödinger kitten state" [7].

In [6][7] the state characterization was done with a conventional balanced homodyne detection. For this thesis another detection method was used, the so called "8-port homodyne detection", which measures two non commuting observables simultaneously [8]. Therefore, two balanced homodyne detectors are used. The signal is divided on a beam splitter into two equal parts and with one detector the amplitude quadrature is read out while the other detector measures the phase quadrature at the same time. With this detection scheme the Q-function of the Schrödinger kitten state can be measured. Additionally, the 8-port homodyne detection allows to use the measured data for a post processing.

Schrödinger kitten states with larger amplitudes can be created by overlapping two indistinguishable Schrödinger kitten states on a 50/50 beam splitter. The procedure is similar to the Hong-Ou-Mandel effect [5, p.217-219][9], where indistinguishable Fock $|1\rangle$ states are superimposed on a 50/50

beam splitter. The result is a Fock $|2\rangle$ state in one of the beam splitter outputs, randomly distributed between the beam splitter output ports. While in the Hong-Ou-Mandel effect the Fock number increases, for cat states the amplitude α gets larger. This was already done in a pure experimental way and resulted in a cat state with an α of 1.85 [10]. This idea was previously proposed in [11] and further developed by [12]. The resulting grown states can be overlapped again to further increase the amplitude. But the experimental effort with 4 squeezing resonators and 4 single photon detectors would be quite high. The success rate is also very small due to the necessary 4 coincident trigger. The 8-port homodyne detection allows to emulate the outcome of the experiment with 4 squeezed-light sources and a 4 coincident single photon detection by using only 1 squeezed-light source and 1 single photon detection.

A possible application for Schrödinger kitten states is the usage as qubit in the field of quantum computation [13]. A qubit can be in a superposition of the logical states $|0\rangle$ and $|1\rangle$ [14, p.13-16]. Therefore, quantum computers can solve some specific problems more efficiently compared to a classical computer [15]. To work fine as qubit the cat state amplitude α should be at least 2 [13, p.1]. So, the amplitude of the photon subtracted states is too small and after one iteration of overlapping it is still too small, but the amplitude after the 2. iteration should be large enough for this application.

Also other experiments were already done with the combination of single photon detection and balanced homodyne detection. For example, the generation of Fock states [16][17][18] or an entanglement distillation [19][20]. Such combination of continuous and discrete variables is called "hybrid quantum optics" [21]. The basic idea for the Fock state generation is the same as for the cat state generation, but even smaller initial squeezing values were taken [17, p.3573]. For the entanglement distillation, an entangled state was created by overlapping a squeezed state with a vacuum state on a beam splitter [19, p.178]. This introduces nonclassical correlations between the beam splitter output ports. The basic idea of a distillation is to extract a low amount of strong nonclassical states from a high amount of weak nonclassical states [22]. Such extraction can be done by conditioning to a single photon detection. Distillation could be useful for quantum cryptography [23][24][25] by increasing the possible distance of quantum key distribution [19][26].

This thesis has following structure. Chapter 2 gives the quantum theory of light, which is necessary for understanding the thesis. Afterwards in chapter 3 the experimental methods are explained, especially the generation

of squeezed states of light and Schrödinger kitten states are thematized. Additionally, the detection of light is introduced. In chapter 4 an optimization of the squeezed-light source is presented. Thereafter a method called "noise envelope locking" is shown in chapter 5, which allows to stabilize the phases in the experiment without using a coherent field. Chapter 6 is about a characterization of avalanche photo diodes, which are needed to apply a single photon subtraction from the squeezed-light. In chapter 7, finally, the measurement of Schrödinger kitten states with an 8-port homodyne detection is shown and the post processing to increase the amplitude of the kitten states is done. The thesis ends with a discussion and outlook in chapter 8.

Chapter 2

Quantum theory of light

In this chapter the quantum theory of light is introduced. A lot of quantum optics books are available, which explain the theoretical principles in detail [5][27][28][29]. This chapter only gives a short summary about the central concepts, which are necessary to understand the following chapters of this thesis. For example, quadrature operators are defined, Heisenberg's uncertainty principle is shown and the properties of different states of light are discussed and visualized. For the visualization the Python package "QuTiP" was used [30][31].

2.1 Field quantization

The field quantization follows the description in [5, p.10-15]. Starting from Maxwell's equations without sources and taking the boundary conditions of a resonator leads to the field operator $\hat{E}(z,t)$:

$$\hat{E}(z,t) = \sqrt{\frac{2\omega^2}{V\epsilon_0}}\hat{q}(t)\sin(kz)\,. \tag{2.1}$$

It describes a field which propagates in z-direction and is polarized along the x-direction. The frequency of the mode is given by ω, k is the wave number, ϵ_0 is the dielectric constant, V is an effective volume and $\hat{q}(t)$ is a time depended operator.
The Hamilton operator $\hat{H}$ is given by

$$\hat{H} = \frac{1}{2}(\hat{p}^2 + \omega^2\hat{q}^2)\,, \tag{2.2}$$

where $\hat{q}$ and $\hat{p}$ are the quantum mechanical position and momentum operators.

The annihilation operator $\hat{a}$ and the creation operator $\hat{a}^\dagger$ are introduced:

$$\hat{a} = \frac{1}{\sqrt{2\hbar\omega}}(\omega\hat{q} + i\hat{p})\,, \tag{2.3}$$

$$\hat{a}^\dagger = \frac{1}{\sqrt{2\hbar\omega}}(\omega\hat{q} - i\hat{p})\,. \tag{2.4}$$

They have a non vanishing commutator:

$$[\hat{a}, \hat{a}^\dagger] = 1\,. \tag{2.5}$$

The Hamilton operator $\hat{H}$ can be written as

$$\hat{H} = \hbar\omega(\hat{a}^\dagger\hat{a} + \frac{1}{2}) = \hbar\omega(\hat{n} + \frac{1}{2})\,. \tag{2.6}$$

The $\hbar$ is the reduced Planck constant and $\hat{n}$ represents the photon number operator:

$$\hat{n} = \hat{a}^\dagger\hat{a}\,. \tag{2.7}$$

2.2 Quadrature operators

The quadrature operators are defined analog to [5, p.17/152]. The annihilation operator $\hat{a}$ and the creation operator $\hat{a}^\dagger$ are non hermitic operators. Therefore, they cannot be observed. But with $\hat{a}$ and $\hat{a}^\dagger$ a hermitic operator can be created, the so called generic quadrature operator $\hat{X}(\Theta)$ defined as

$$\hat{X}(\Theta) = \frac{1}{2}(\hat{a}e^{-i\Theta} + \hat{a}^\dagger e^{i\Theta})\,. \tag{2.8}$$

For $\Theta = 0^\circ$ this leads to the amplitude quadrature $\hat{X}$:

$$\hat{X} = \frac{1}{2}(\hat{a} + \hat{a}^\dagger) \tag{2.9}$$

and for $\Theta = 90^\circ$ this leads to the phase quadrature $\hat{Y}$:

$$\hat{Y} = \frac{1}{2\mathrm{i}}(\hat{a} - \hat{a}^\dagger). \tag{2.10}$$

The field operator $\hat{E}(z,t)$ from equation 2.1 can be rewritten as

$$\hat{E}(z,t) = 2\epsilon_0 \sin(kz)[\hat{X}\cos(\omega t) + \hat{Y}\sin(\omega t)]\,, \tag{2.11}$$

and the Hamilton operator $\hat{H}$ from equation 2.6 can be rewritten as

$$\hat{H} = \hbar\omega(\hat{X}^2 + \hat{Y}^2)\,. \tag{2.12}$$

2.3 Heisenberg uncertainty principle

The Heisenberg uncertainty principle can be found in [5, p.150-151]. For two operators $\hat{A}$ and $\hat{B}$ with the commutator relation $[\hat{A}, \hat{B}] = \mathrm{i}\hat{C}$ following uncertainty relation is given:

$$\Delta^2\hat{A}\,\Delta^2\hat{B} \geq \frac{1}{4}|\left\langle\hat{C}\right\rangle|^2\,. \tag{2.13}$$

$\Delta^2\hat{O}$ is the variance of an operator $\hat{O}$

$$\Delta^2\hat{O} = \left\langle\hat{O}^2\right\rangle - \left\langle\hat{O}\right\rangle^2\,, \tag{2.14}$$

and $\left\langle\hat{O}\right\rangle$ represents the expectation value:

$$\left\langle\hat{O}\right\rangle = \langle\psi|\hat{O}|\psi\rangle\,. \tag{2.15}$$

For the amplitude quadrature $\hat{X}$ and the phase quadrature $\hat{Y}$ the commutator is called:

$$[\hat{X}_I, \hat{Y}_I] = \frac{\mathrm{i}}{2}\,. \tag{2.16}$$

Equation 2.13 and equation 2.16 lead to the uncertainty relation of the quadrature operators:

$$\Delta^2\hat{X}\,\Delta^2\hat{Y} \geq \frac{1}{16}\,. \tag{2.17}$$

The Heisenberg uncertainty principle shows that the product of the variances is limited. Therefore, it is not possible to measure the amplitude quadrature $\hat{X}$ and the phase quadrature $\hat{Y}$ precisely at the same time.

2.4 Wigner function

Information about the Wigner function are taken from [28, p.37-54][32]. The Wigner function is a phase space quasi-probability distribution, which can fully describe a quantum state of light. It can have negative values, which indicates that a state is nonclassical, for example, the Fock states in section 2.6.

But it is also possible to have a nonclassical state without observing negativities in the Wigner function. For example, the squeezed states in section 2.8 are nonclassical states without negativities in the Wigner function. The Wigner function is defined as:

$$W(X,Y) = \frac{1}{2\pi} \int_{-\infty}^{\infty} e^{iYz} \left\langle X - \frac{z}{2} | \hat{\rho} | X + \frac{z}{2} \right\rangle \, dz \,, \tag{2.18}$$

where $\hat{\rho}$ is the density matrix:

$$\hat{\rho} = |\psi\rangle \langle\psi| \,. \tag{2.19}$$

The Wigner function is normalized:

$$\int_{-\infty}^{\infty} \int_{-\infty}^{\infty} W(X,Y) \, dX \, dY = 1 \,. \tag{2.20}$$

Furthermore, the Wigner function is real for Hermitian operators $\hat{\rho}$:

$$W(X,Y)^{\star} = W(X,Y) \,. \tag{2.21}$$

2.5 Vacuum state

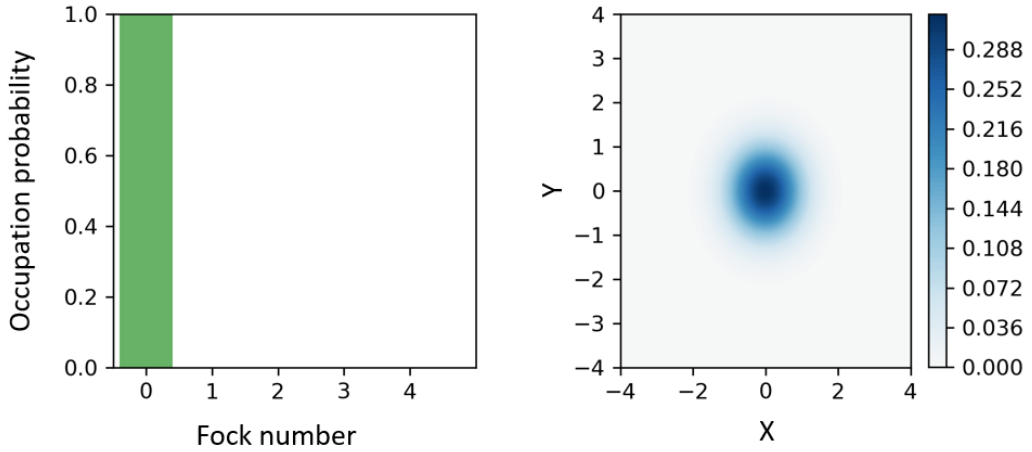

Figure 2.1: Photon statistics (left) and Wigner function (right) are shown for a vacuum state. The vacuum state contains no photons. The quadrature distributions are symmetric Gaussians around the origin with a minimal uncertainty product. Plots created with the Python package "QuTiP".

The vacuum state is introduced in [5, p.29]. For the vacuum state $|0\rangle$ the expectation values for the quadrature operators is zero. Hence, there is no electric field on average:

$$\langle 0|\hat{X}|0\rangle = 0\,, \tag{2.22}$$

$$\langle 0|\hat{Y}|0\rangle = 0\,. \tag{2.23}$$

Whereas the variances of the quadrature operators are non zero:

$$\Delta^2\hat{X} = \left\langle 0|\hat{X}^2|0\right\rangle - \langle 0|\hat{X}|0\rangle^2 = \frac{1}{4}\,, \tag{2.24}$$

$$\Delta^2\hat{Y} = \left\langle 0|\hat{Y}^2|0\right\rangle - \langle 0|\hat{Y}|0\rangle^2 = \frac{1}{4}\,. \tag{2.25}$$

Therefore, the vacuum state has a certain noise around zero. When the variances are put into the Heisenberg uncertainty principle from equation 2.17 the minimal possible value of $1/16$ comes out. So, the vacuum state is a state of minimal uncertainty. The value of $1/16$ is a normalization constant, which can be chosen differently. Another typical value is a vacuum normalization to 1. Figure 2.1 shows the photon statistics of a vacuum state, which is constant zero. The Wigner function of a vacuum state is also shown in figure 2.1 and has following formula [28, p.45]:

$$W_{|0\rangle}(X,Y) = \frac{1}{\pi}e^{(-X^2-Y^2)}\,. \tag{2.26}$$

2.6 Fock state

The Fock state properties are presented in [5, p.14-15]. The Fock states $|n\rangle$ are created from the vacuum state $|0\rangle$:

$$|n\rangle = \frac{(\hat{a}^\dagger)^n}{\sqrt{n!}}|0\rangle\,. \tag{2.27}$$

The mean photon number of a Fock state is given by

$$\langle n|\hat{n}|n\rangle = n\,. \tag{2.28}$$

The variance of the photon number is zero:

$$\Delta^2\hat{n} = \left\langle n|\hat{n}^2|n\right\rangle - \langle n|\hat{n}|n\rangle^2 = 0\,. \tag{2.29}$$

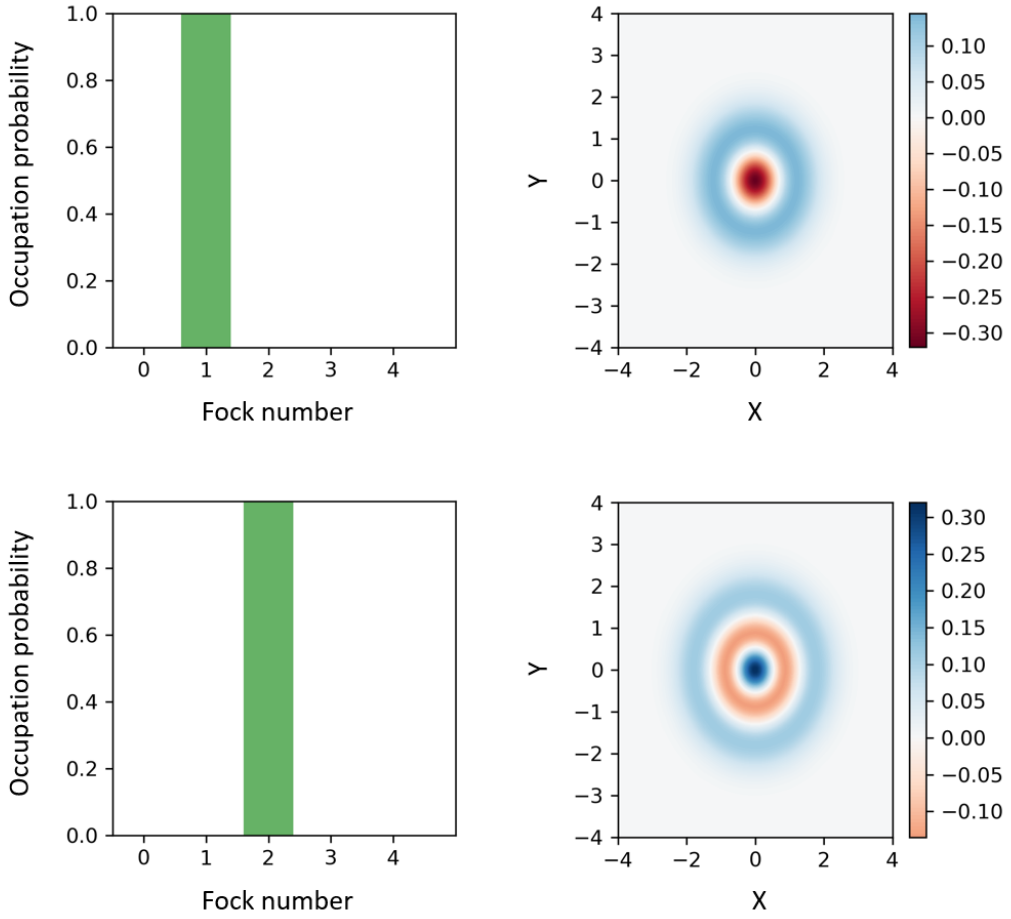

Figure 2.2: Photon statistics (left) and Wigner function (right) are shown for a Fock state with n = 1 (top) and n = 2 (bottom). Fock states have exactly the number of photons as their Fock number. The quadrature distributions are symmetric around the origin. They have a non Gaussian shape and contain negativities, which indicates the nonclassicality of Fock states. Plots created with the Python package "QuTiP".

Hence, Fock states have a fixed photon number as can be seen in figure 2.2. The Wigner function of a Fock state is also shown in figure 2.2 and has following formula [33, p.9]:

$$W_{|n\rangle}(X,Y) = \frac{1}{\pi} e^{(-X^2-Y^2)} (-1)^n L_n^{(0)}[2(X^2+Y^2)]\,, \tag{2.30}$$

where $L_n^{(0)}$ are generalized Laguerre polynomials.

The Wigner function of a Fock $|1\rangle$ state looks like a crater with a negativity at the origin. Hence, it is a nonclassical state of light.

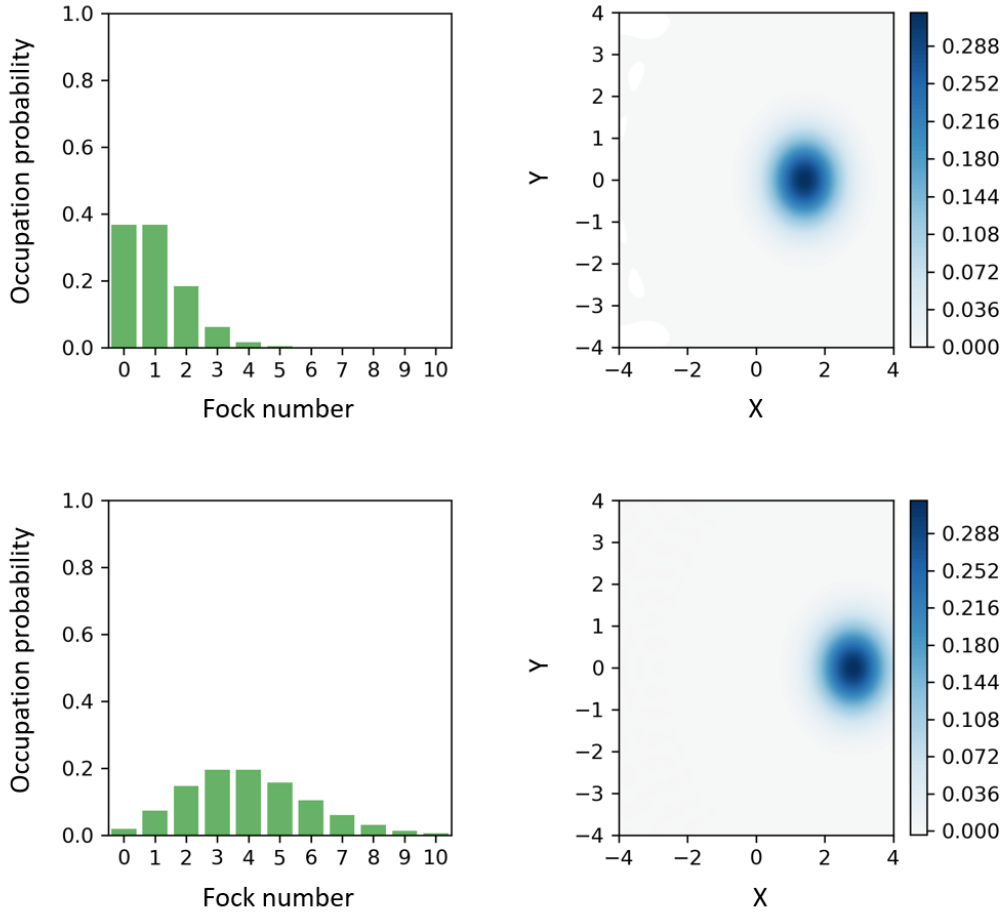

Figure 2.3: Photon statistics (left) and Wigner function (right) are shown for a coherent state with $\alpha = 1$ (top) and $\alpha = 2$ (bottom). Coherent states have a Poissonian photon distribution. The quadrature distributions are symmetric Gaussians displaced from the origin with a minimal uncertainty product. Plots created with the Python package "QuTiP".

2.7 Coherent state

The properties of a coherent state are taken from [5, p.43-71]. Coherent states $|\alpha\rangle$ can be presented as a sum over Fock states $|n\rangle$:

$$|\alpha\rangle = e^{\frac{-|\alpha|^2}{2}} \sum_{n=0}^{\infty} \frac{\alpha^n}{\sqrt{n!}} |n\rangle \,. \tag{2.31}$$

The photon statistics of a coherent state is a Poissonian as can be seen in figure 2.3. A characteristic of a Poisson statistics is that the expectation value is equal to the variance:

$$\langle \alpha | \hat{n} | \alpha \rangle = |\alpha|^2 = \Delta^2 \hat{n} \,. \tag{2.32}$$

The coherent states $|\alpha\rangle$ are eigenstates to the annihilation operator $\hat{a}$, where $\alpha = |\alpha|e^{i\Theta}$ is a complex number.
The expectation value of the amplitude quadrature $\hat{X}$ and the phase quadrature $\hat{Y}$ are:

$$\langle\alpha|\hat{X}|\alpha\rangle = |\alpha|\cos(\Theta)\,, \tag{2.33}$$

$$\langle\alpha|\hat{Y}|\alpha\rangle = |\alpha|\sin(\Theta)\,. \tag{2.34}$$

The variances are the same as for the vacuum state $|0\rangle$. Hence, they are also states of minimal uncertainty:

$$\Delta^2\hat{X} = \left\langle\alpha|\hat{X}^2|\alpha\right\rangle - \langle\alpha|\hat{X}|\alpha\rangle^2 = \frac{1}{4}\,, \tag{2.35}$$

$$\Delta^2\hat{Y} = \left\langle\alpha|\hat{Y}^2|\alpha\right\rangle - \langle\alpha|\hat{Y}|\alpha\rangle^2 = \frac{1}{4}\,. \tag{2.36}$$

Coherent states $|\alpha\rangle$ can be presented as a shifted vacuum state $|0\rangle$:

$$|\alpha\rangle = \hat{D}(\alpha)|0\rangle\,, \tag{2.37}$$

where $\hat{D}$ is the shifting operator:

$$\hat{D}(\alpha) = \exp(\alpha\hat{a}^\dagger - \alpha^*\hat{a})\,. \tag{2.38}$$

The Wigner function of a coherent state is shown in figure 2.3 and has following formula [28, p.49]:

$$W_{|\alpha\rangle}(X,Y) = \frac{1}{\pi}e^{(-(X-X_0)^2-(Y-Y_0)^2)}\,. \tag{2.39}$$

2.8 Squeezed state

The description of squeezed states follows [5, p.150-165]. The squeezing operator is called:

$$\hat{S}(\xi) = \exp\left[\frac{1}{2}(\xi^*\hat{a}^2 - \xi\hat{a}^{\dagger 2})\right]\,. \tag{2.40}$$

When it is applied to a vacuum state $|0\rangle$, a squeezed vacuum state $|0,\xi\rangle$ is created. When it is applied to a coherent state $|\alpha\rangle$, a squeezed coherent state $|\alpha,\xi\rangle$ is created. For ξ following relation is given:

$$\xi = re^{i\theta}\,, \tag{2.41}$$

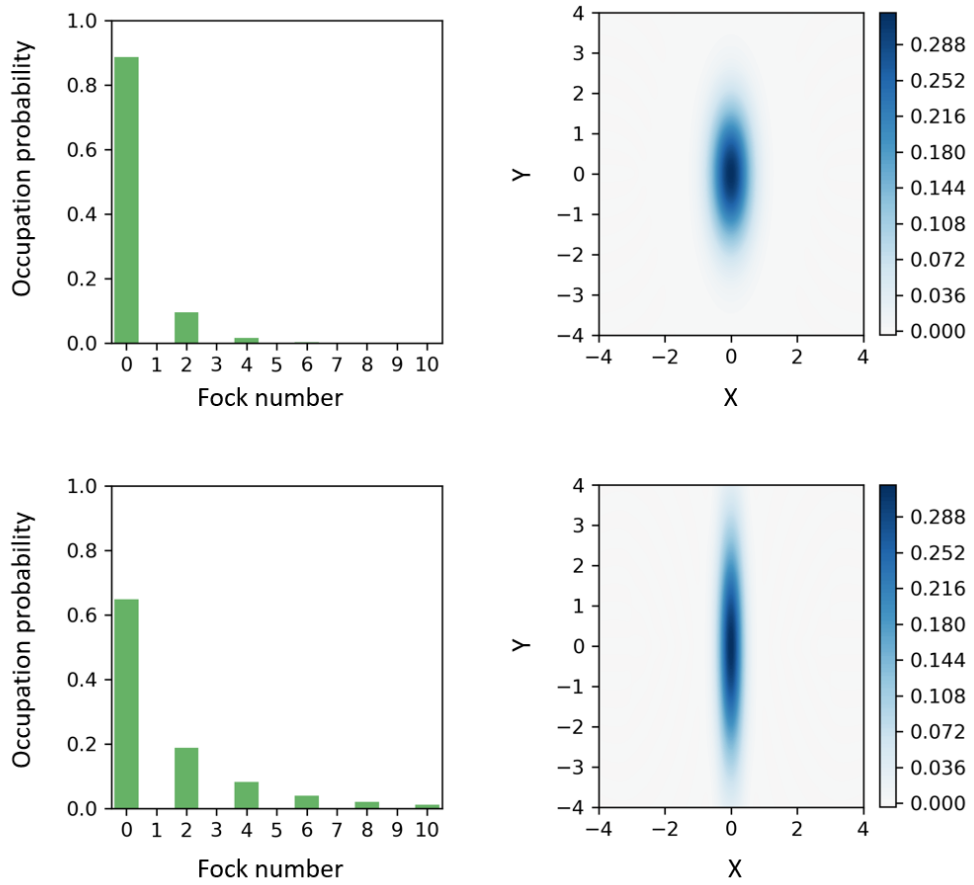

Figure 2.4: Photon statistics (left) and Wigner function (right) are shown for a squeezed vacuum state with r = 0.5 (top) and r = 1 (bottom). Squeezed vacuum states have a photon distribution where only even Fock numbers are populated. The quadrature distributions are Gaussians with an elliptic shape around the origin. The squeezed quadrature has a lower uncertainty as the vacuum state. The orthogonal anti-squeezed quadrature has a larger uncertainty as the vacuum state. The uncertainty product is limited by Heisenberg's uncertainty principle. Plots created with the Python package "QuTiP".

with r as squeeze parameter in the interval of $0 \leq r \leq \infty$ and Θ as squeeze angle in the interval of $0 \leq \Theta \leq 2\pi$. For squeezed states there is an angle Θ where the generic quadrature operator $\hat{X}(\Theta)$ from equation 2.8 gives a smaller variance as the vacuum state has. The orthogonal quadrature is anti-squeezed because it has a larger variance as the vacuum state to fulfill the Heisenberg's uncertainty principle from section 2.3. Therefore, a squeezed state looks like an ellipse and can be seen in figure 2.4 as Wigner function, which has following formula [28, p.48]:

$$W_{|0,\xi\rangle}(X,Y) = \frac{1}{\pi} e^{\left(-e^{2\xi}X^2 - e^{-2\xi}Y^2\right)}. \tag{2.42}$$

The Wigner function of a squeezed state shows no negativity, but it is still a nonclassical state of light [5, p.150/165]. The photon statistics of a squeezed state is also shown in figure 2.4 and contains only even numbers. The reason for this characteristic is a pairwise creation of photons, as it is explained in chapter 3.1.

2.9 Schrödinger cat state

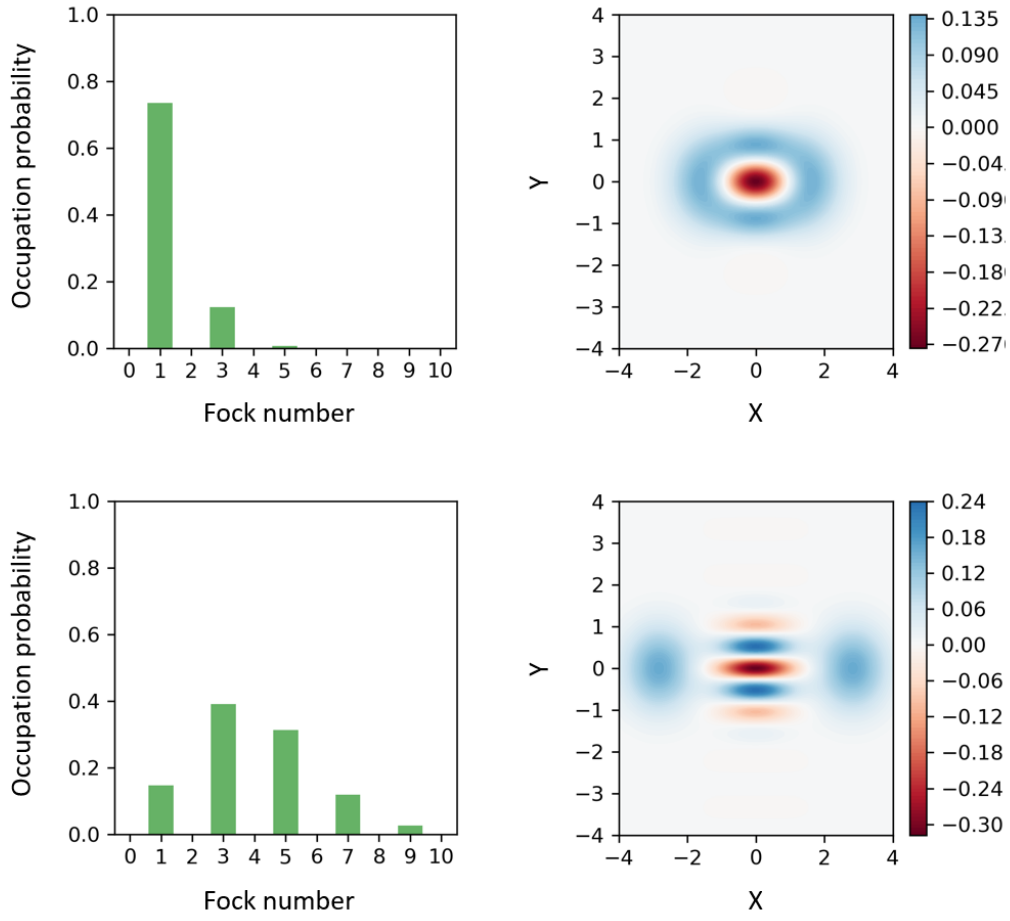

Figure 2.5: Photon statistics (left) and Wigner function (right) are shown for an odd cat state with $\alpha = 1$ (top) and $\alpha = 2$ (bottom). Odd cat states have a photon distribution where only odd Fock numbers are populated. The quadrature distributions contain negativities, which indicates the nonclassicality of odd cat states. For small amplitudes an odd cat state approximates to a Fock $|1\rangle$ state and has a negativity at the origin. For high amplitudes an interference pattern is visible and two Gaussian hills at the edges can be observed. Plots created with the Python package "QuTiP".

The description of Schrödinger cat states is taken from [5, p.174-182]. A cat state in quantum optics is a superposition of two coherent states $|\alpha\rangle$ with

opposite phases:

$$\psi_{cat} \propto (|\alpha\rangle \pm |-\alpha\rangle)\,. \tag{2.43}$$

Equation 2.43 is called "odd cat" for the superposition with "-" because only odd photon numbers appear in the photon statistics:

$$\psi_{cat,odd} \propto e^{\frac{-|\alpha|^2}{2}} \sum_{n=0}^{\infty} \frac{\alpha^{2n+1}}{\sqrt{(2n+1)!}} |2n+1\rangle\,. \tag{2.44}$$

In figure 2.5 the photon statistics of an odd cat is visualized. The Wigner function of an odd cat is also shown in figure 2.5 and has following formula [5, p.178]:

$$\begin{aligned} W_{cat,odd}(X,Y) = \frac{1}{\pi(1+e^{-2\alpha^2})}[&e^{-2(X-\alpha)^2-2Y^2} + e^{-2(X+\alpha)^2-2Y^2} \\ &-2e^{-2X^2-2Y^2}\cos(4Y\alpha)]\,. \end{aligned} \tag{2.45}$$

The Wigner function of an odd cat state looks for small amplitudes α similar to a Fock $|1\rangle$ state. Consequentially it has the crater shape and a negativity at the origin. Hence, it is also a nonclassical state of light. For higher amplitudes an interference pattern appears with more negativity stripes.

Equation 2.43 is called "even cat" for the superposition with "+" because only even photon numbers appear in the photon statistics:

$$\psi_{cat,even} \propto e^{\frac{-|\alpha|^2}{2}} \sum_{n=0}^{\infty} \frac{\alpha^{2n}}{\sqrt{2n!}} |2n\rangle\,. \tag{2.46}$$

In figure 2.6 the photon statistics of an even cat is visualized. The Wigner function of an even cat is also shown in figure 2.6 and has following formula [5, p.177]:

$$\begin{aligned} W_{cat,even}(X,Y) = \frac{1}{\pi(1+e^{-2\alpha^2})}[&e^{-2(X-\alpha)^2-2Y^2} + e^{-2(X+\alpha)^2-2Y^2} \\ &+2e^{-2X^2-2Y^2}\cos(4Y\alpha)]\,. \end{aligned} \tag{2.47}$$

The Wigner function of an even cat state also indicates the nonclassicality of the state because it has negativities. For small amplitude α there are 2 negativities, which are beside the origin. For higher amplitudes an interference pattern appears with more negativity stripes.

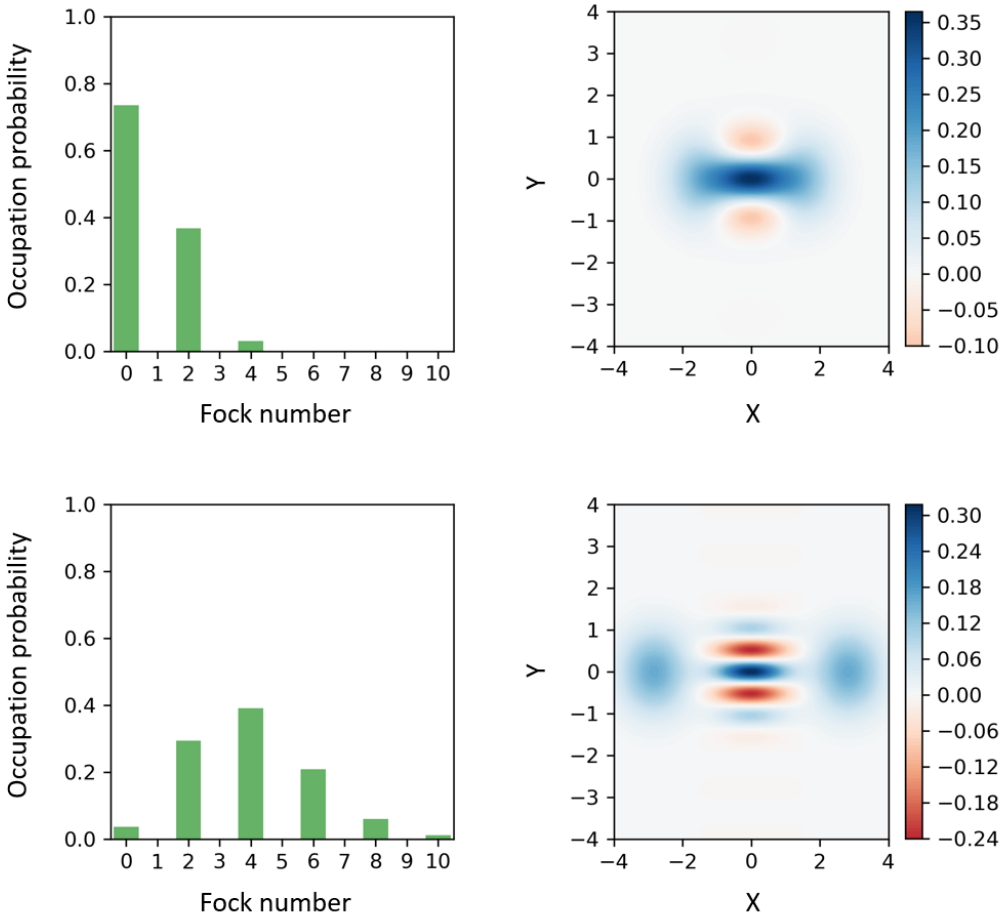

Figure 2.6: Photon statistics (left) and Wigner function (right) are shown for an even cat state with $\alpha = 1$ (top) and $\alpha = 2$ (bottom). Even cat states have a photon distribution where only even Fock numbers are populated. The quadrature distributions contain negativities beside the origin, which indicates the nonclassicality of even cat states. For high amplitudes an interference pattern is visible and two Gaussian hills at the edges can be observed. Plots created with the Python package "QuTiP".

2.10 Q-function

Information about the Q-function are taken from [28, p.54-56]. The Q-function is the convolution of the Wigner function with the vacuum state:

$$Q(X,Y) = \frac{1}{\pi} \int_{-\infty}^{\infty} \int_{-\infty}^{\infty} W(X',Y') e^{(-(X-X')^2-(Y-Y')^2)} \, dX' \, dY' \, . \tag{2.48}$$

The connection to the density matrix from equation 2.19 is given by:

$$Q(\alpha) = \frac{1}{2\pi} \langle \alpha | \hat{\rho} | \alpha \rangle \, . \tag{2.49}$$

The Q-function is also a quasi-probability distribution, which can be used to characterize a state of light. The Q-function is non negative and normalized to unity. The Q-function can be measured via an 8-port homodyne detection, which is explained in chapter 3.4.2. Figure 2.7 shows the Q-function for different states of light.

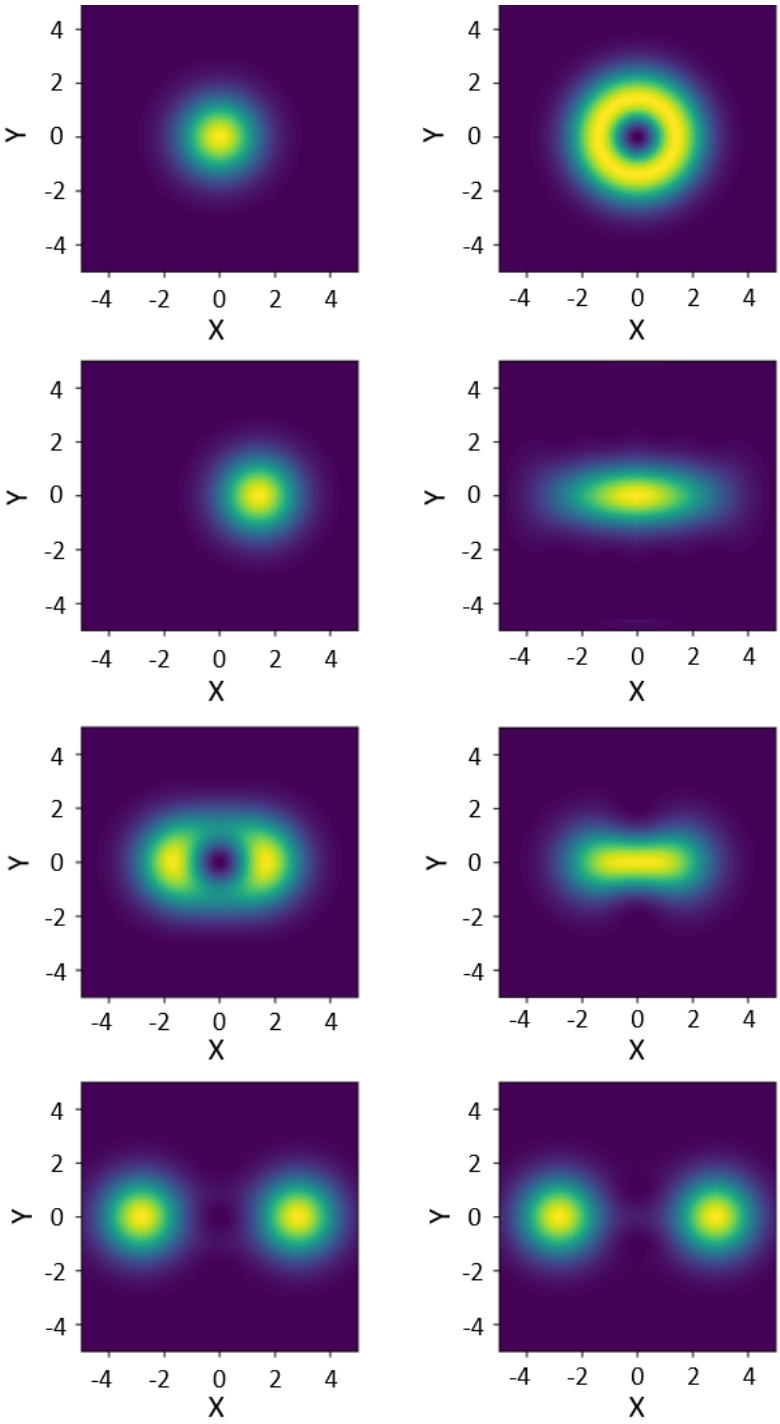

Figure 2.7: Q-functions for different states of light. First row: vacuum state (left) and Fock state with $n = 1$ (right). Second row: coherent state with $\alpha = 1$ (left) and squeezed state with $r = 1$ (right). Third row: odd cat state with $\alpha = 1$ (left) and even cat state with $\alpha = 1$ (right). Last row: odd cat state with $\alpha = 2$ (left) and even cat state with $\alpha = 2$ (right). Plots created with the Python package "QuTiP".

Chapter 3

Experimental methods

In this chapter the experimental methods are introduced. At the beginning, the generation of squeezed states of light by using a nonlinear effect are explained. Afterwards the generation of Schrödinger kitten states is shown. The basic idea to create such states is to subtract a single photon from a weakly squeezed state of light. Therefore, a single photon detector is necessary. Hence, the concept of a single photon detection is part of this chapter. Finally, the balanced homodyne detection is thematized, which makes it possible to measure and characterize the different states of light.

3.1 Generation of squeezed states of light

The properties of squeezed states of light were already shown in chapter 2.8. Here some background information about the generation are presented. This chapter is based on following literature [34][35, p.23-57][36, p.84-88].

The generation of squeezed states of light is done in a nonlinear process called "spontaneous parametric down-conversion" or " optical parametric amplification". To activate this process, a laser beam of a certain wavelength is sent into a nonlinear crystal as pump field. Inside the crystal the pump field is converted to light with the doubled wavelength. According to energy conversation a pump photon at 532 nm can decay to 2 photons at 1064 nm. The process in opposite direction is also possible, where light of the doubled frequency is produced by combining 2 photons at 1064 nm to 1 photon at 532 nm. This case is called "second harmonic generation" (SHG). More details about the SHG process can be found in [36, p.96-105].

For both directions a phase matching between the two wavelength is necessary to get a high conversion efficiency. In this thesis a periodically poled potassium titanyl phosphate (PPKTP) crystal is used for the squeezing generation, therefore, a quasi-phase matching has to be done via controlling the

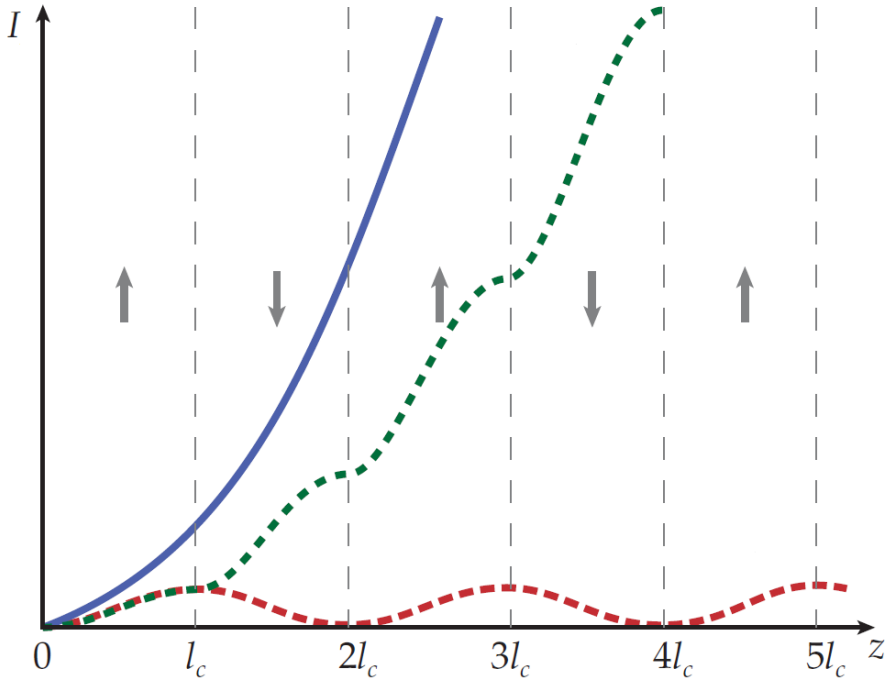

Figure 3.1: Phase matching conditions. The intensity of a converted light field is shown in dependence of the crystal length for different phase matching conditions. Perfect phase matching (blue), which shows a continuously increasing intensity. No phase matching (red), only very small intensities are reachable. Quasi-phase matching (green), where the intensity increases stepwise. The reason for this behavior is the periodic poling of the crystal, which is indicated by the arrows. Picture taken from [37, p.32] referring to [38, p.2632].

crystal temperature. Figure 3.1 shows the quasi-phase matching and compares it to the cases of perfect phase matching and no phase matching. The characteristic shape of the quasi-phase matching is a stepwise enlargement of the intensity caused by the periodic poling.

The PPKTP crystal is placed inside a resonator to achieve higher squeezing values. Figure 3.2 shows such squeezing resonator. The cavity is formed by a coupling mirror and the backside of the PPKTP crystal, which is curved and coated for high reflectivity. The length of the cavity can be controlled with a piezoelectric element on the coupling mirror. Furthermore, the squeezing resonator contains Peltier elements to control the temperature of the PPKTP crystal to achieve the necessary quasi-phase matching. The pump field is coupled into the squeezing resonator through the coupling mirror together with a vacuum mode of the doubled wavelength. Inside the crystal the vacuum mode is squeezed and a squeezed vacuum mode is coupled out through

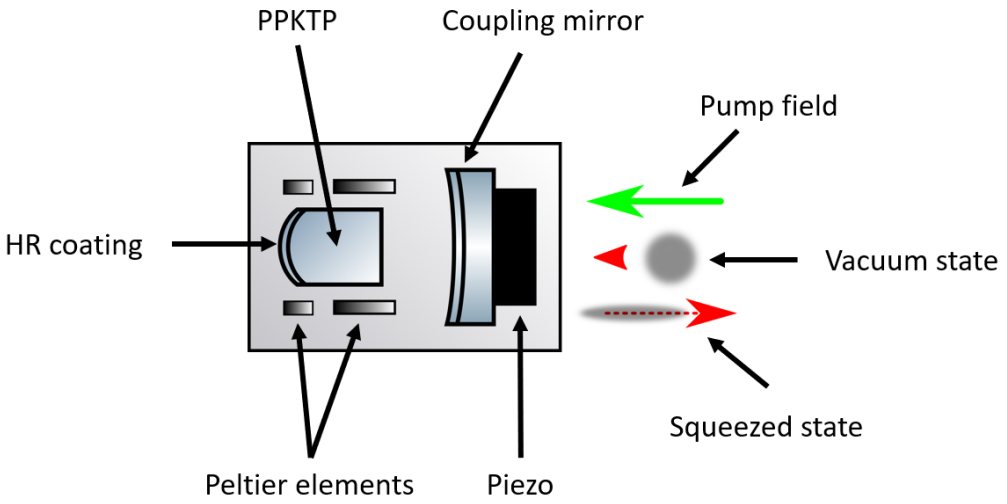

Figure 3.2: A squeezing resonator is shown. It is a linear cavity composed of a high reflected (HR) coated nonlinear crystal (PPKTP) and a coupling mirror. The temperature of the PPKTP crystal can be stabilized with Peltier elements to the required quasi-phase matching temperature. The coupling mirror is connected with a piezoelectric element to be able to control the cavity length. A pump field at 532 nm enters the squeezing resonator through the coupling mirror together with a vacuum mode at 1064 nm. Inside the PPKTP crystal the vacuum mode is squeezed by optical parametric down conversion. The squeezed state leaves the squeezing resonator through the coupling mirror. Picture created with Microsoft Power Point.

the coupling mirror. Theoretically due to destructive interference at the coupling mirror infinity squeezing would be possible. But in practice the reachable squeeze values are limited by optical loss. Optical loss can be seen as mixing in a vacuum state, which reduces the amount of squeezing. Following formula describes the variance of a squeezed state $\Delta^2\hat{X}_\epsilon(\Theta)$ with optical loss ϵ:

$$\Delta^2\hat{X}_\epsilon(\Theta) = (1-\epsilon)\Delta^2\hat{X}_{Initial}(\Theta) + \epsilon\Delta^2\hat{X}_0\,. \tag{3.1}$$

$\Delta^2\hat{X}_0$ is the variance of the vacuum state and $\Delta^2\hat{X}_{Initial}(\Theta)$ indicates the variance of the initial created squeezed state. Equation 3.1 can be converted to a formula for the optical loss ϵ and the initial squeezing $\Delta^2\hat{X}_{Initial}(\Theta)$:

$$\epsilon = \frac{1-\Delta^2\hat{X}\Delta^2\hat{Y}}{2-\Delta^2\hat{X}-\Delta^2\hat{Y}}\,, \tag{3.2}$$

$$\Delta^2\hat{X}_{Initial}(\Theta) = \frac{\Delta^2\hat{X}_\epsilon(\Theta)-\epsilon\Delta^2\hat{X}_0}{1-\epsilon}\,. \tag{3.3}$$

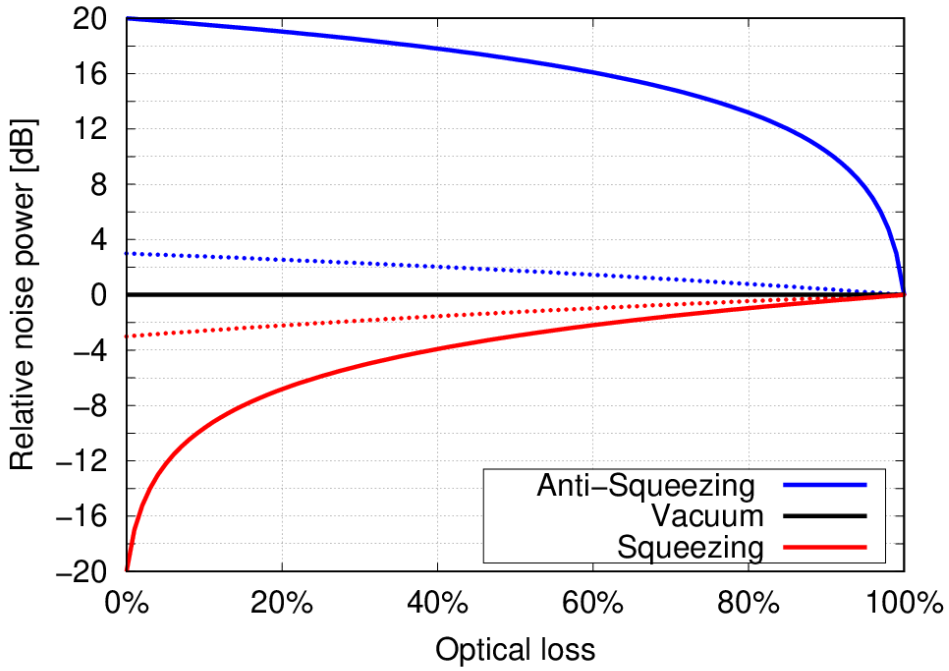

Figure 3.3: Squeezed state with optical loss. The relative noise power in dB is plotted against the optical loss for different initial squeeze values. The solid lines represent an initial squeeze value of 20 dB and the dashed lines represent an initial squeeze value of 3 dB. It is visible that the squeezed quadrature is more vulnerable for optical loss than the anti-squeezed quadrature and higher squeeze values are more vulnerable for optical loss than lower squeeze values. The plot was created with a gnuplot script written by Jan Südbeck.

Squeeze values can be represented in decibel (dB):

$$x\ dB = -10 \log_{10} \left(\frac{\Delta^2 \hat{X}(\Theta)}{\Delta^2 \hat{X}_0} \right) . \tag{3.4}$$

Alternatively, the squeeze value can be expressed as r value, as it was introduced in chapter 2.8. The connection between r and dB is

$$r = -\frac{1}{2} \ln(10^{-\frac{x\ dB}{10}}) . \tag{3.5}$$

Figure 3.3 shows a simulation of different squeezed states with optical loss. The squeezed and anti-squeezed quadrature get smaller for higher optical loss. The squeezed quadrature reacts stronger to optical loss than the anti-squeezed quadrature and higher squeeze values are more vulnerable than smaller squeeze values.

3.2 Generation of Schrödinger kitten states

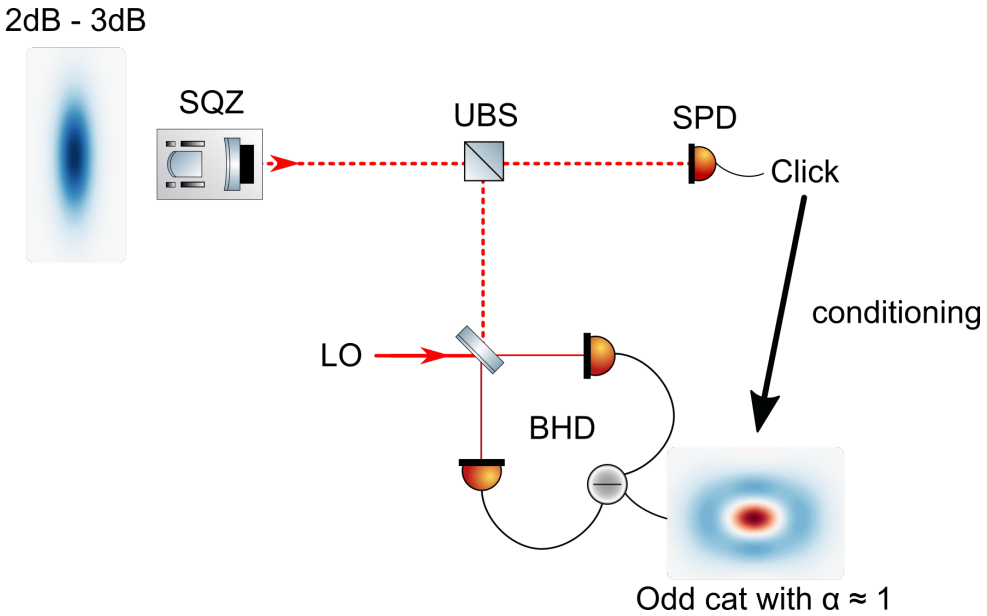

Figure 3.4: Schrödinger kitten state generation. A weakly squeezed state (around 2 dB - 3 dB) is generated in a squeezing resonator (SQZ) and is sent to an unbalanced beam splitter (UBS). The UBS reflects most of the squeezed signal to a balanced homodyne detector (BHD), but a small part of the squeezed signal is transmitted to a single photon detector (SPD). The SPD signal indicates that a single photon (Fock $|1\rangle$ state) was subtracted from the squeezed state. By conditioning the BHD signal to the SPD signal, an odd cat sate can be detected from the BHD. The reachable cat state amplitude α with this method is only around 1. Therefore, the generated states are called "Schrödinger kitten states". Picture created with Inkscape referring to [7, p.84].

The properties of quantum optical cat states were already shown in chapter 2.9. Here some background information about the generation are presented. This chapter is based on following literature [6][7][39].

The basic idea is to subtract a single photon from a weakly squeezed state of light. Therefore, a squeezed state of light is generated as described in the previous section 3.1. Only a small pump power of a few mW is used to generate an initial squeeze value around 2 dB - 3 dB. The squeezed field is sent to an unbalanced beam splitter, which sent a small part of the squeezed signal to a single photon detector and the rest of the signal to a balanced homodyne detector. The single photon detector signal acts as a trigger, which indicates that a single photon was subtracted from the squeezed signal. The balanced homodyne detector signal is conditioned to this trigger to measure a quantum state of light, which looks very similar to an odd cat state. The amplitude α of this state is only around 1, therefore, the generated states do

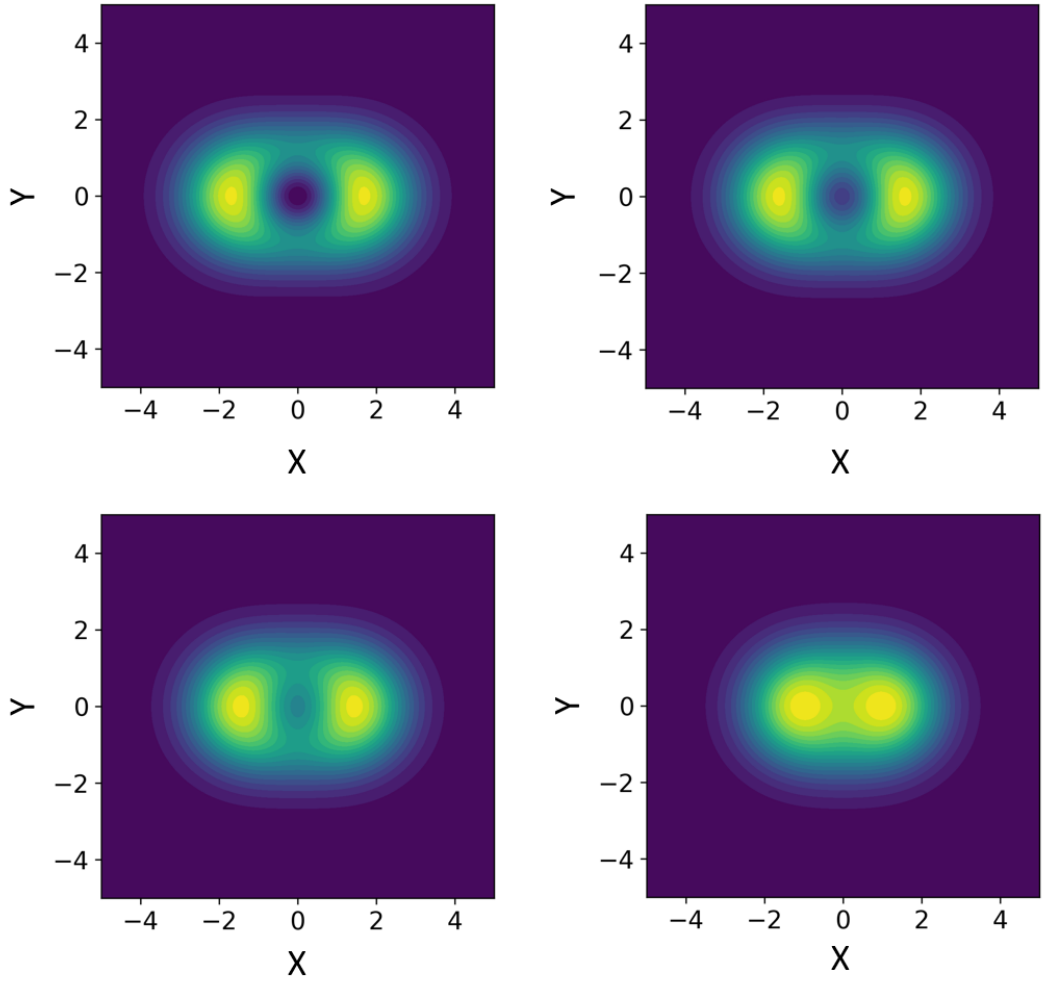

Figure 3.5: Q-functions of an odd cat state with $\alpha = 1$ are shown for different loss values. Top left no loss, top right 10 % loss, bottom left 25 % loss and bottom right 50 % loss. With increasing loss, the odd cat state is smoothed out by a vacuum state and the characteristic hole in the middle of the Q-function vanishes. The plots were created with a Python script written by Felix Pein.

not represent a macroscopic cat state. In the literature such cat states with small amplitudes are called "Schrödinger kitten states". Figure 3.4 visualizes the Schrödinger kitten state generation.

As discussed in chapter 2.9 the cat states are nonclassical states of light and, therefore, they are vulnerable for decoherence sources like optical loss. Hence, an increasing loss destroys the cat state properties as can be seen in figure 3.5 for an odd cat with $\alpha = 1$. The plots of the lossy Q-function were created with a Python script written by Felix Pein. The model behind this script is explained in [40, p.16-18].

3.3 Single photon detection

For the single photon detection different kind of detectors can be used. Two types of single photon detectors are explained. On the one hand an avalanche photo diode (APD) and on the other hand a superconducting nanowire single photon detector (SNSPD).

3.3.1 Avalanche photo diode

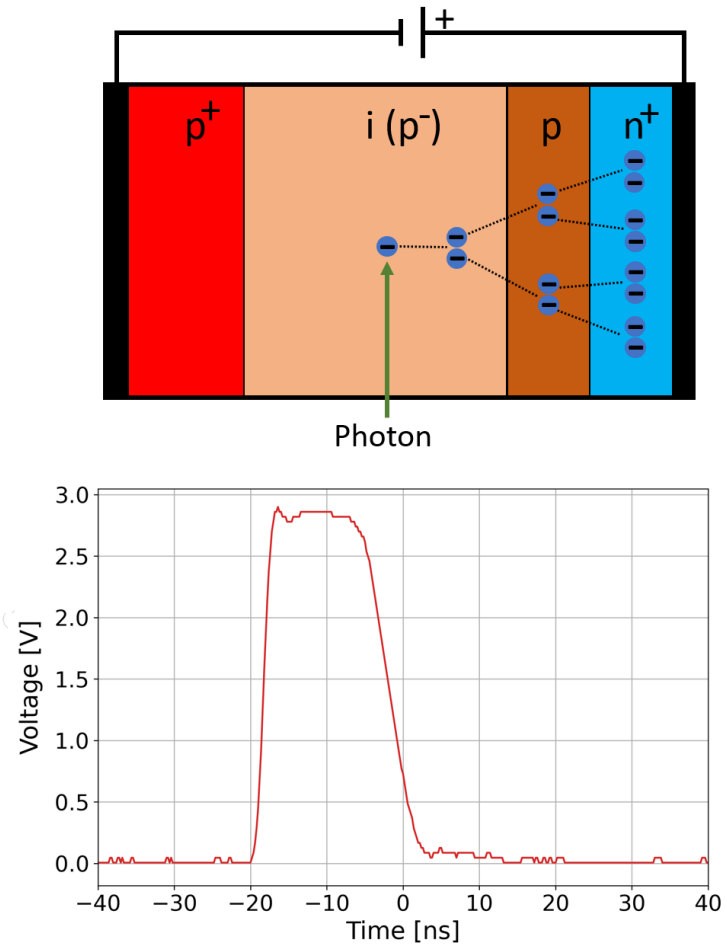

Figure 3.6: On the top side the working principle of an APD is shown. A photon creates an electron. This electron is accelerated by an applied voltage and triggers an avalanche of secondary electrons. On the bottom side an example of an APD signal is shown. It is a self-made measurement of the COUNT 50N-FC signal with an oscilloscope. More details about this detector can be found in chapter 6.3 and in the data sheet [41]. Top picture created with Microsoft Power Point referring to [42, p.3]. The bottom picture is an oscilloscope data plot done in Python with a script written by Felix Pein.

An introduction about APDs can be found in [43]. The APD is a detector based on a semiconducting material, for example, silicon or InGaAs. A single photon creates a single electron. The single electron is accelerated by an applied bias voltage and creates a secondary electron. The secondary electrons can create further electrons, which results in an avalanche of electrons which produce a measurable signal. Figure 3.6 shows the working principle of an APD and illustrates the resulting signal on an oscilloscope. After such an avalanche process the detector needs a certain recovery time before the next photon can be measured. The time where the detector is blind is called "dead time". Even without a photon, an APD can generate a signal, for example, because a thermal excitation releases an electron, which activates an avalanche. Signals which are created without a photon are called "dark counts". Another relevant effect is the process of after pulsing. After an avalanche an electron might stuck in the detector material which triggers a new avalanche.

Not every photon activates an avalanche. Hence, the quantum efficiency of an APD is an interesting parameter. A rough estimation of the quantum efficiency η can be calculated by dividing the measured count rate $R_{detected}$ through the incoming photon rate $R_{incident}$:

$$\eta = \frac{R_{detected}}{R_{incident}}. \tag{3.6}$$

Thereby the incoming photon rate $R_{incident}$ is defined as:

$$R_{incident} = \frac{P\lambda}{hc}, \tag{3.7}$$

with the wavelength λ, power P, speed of light c and Plank constant h. A more precise quantum efficiency $\eta_{corrected}$ can be determined by using a count rate $R'_{detected}$ which is corrected from dark counts R_{dark} and dead time τ:

$$R'_{detected} = \frac{R_{detected}}{1 - R_{detected}\tau} - \frac{R_{dark}}{1 - R_{dark}\tau}, \tag{3.8}$$

$$\eta_{corrected} = \frac{R'_{detected}}{R_{incident}}. \tag{3.9}$$

3.3.2 Superconducting nanowire single photon detector

An introduction about SNSPDs can be found in [44]. The SNSPD consists of a thin and narrow superconducting nanowire. The nanowire is cooled below the critical temperature for a superconducting state. If a photon hits

the nanowire, the superconductivity is disturbed by a hotspot, which has a finite electrical resistance and leads to a measurable signal. Figure 3.7 visualizes the working principle of an SNSPD and shows the resulting signal on an oscilloscope.

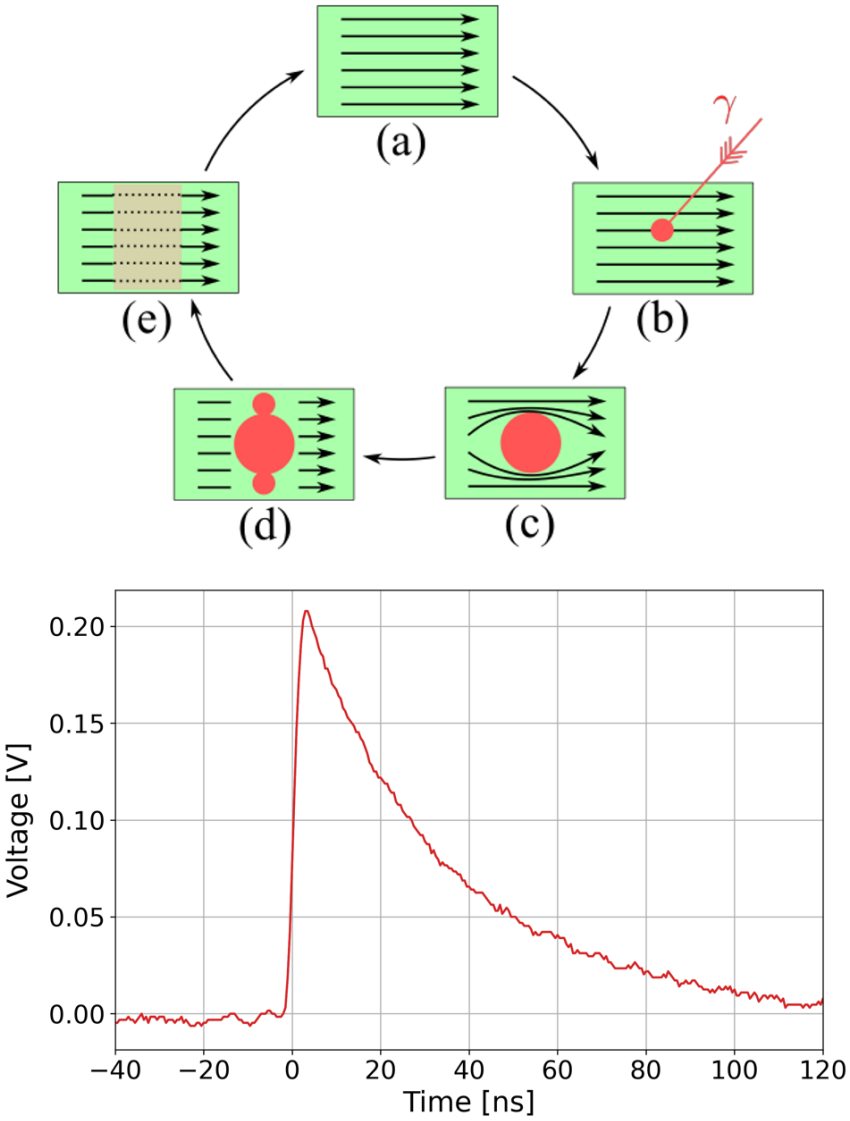

Figure 3.7: On the top side the working principle of an SNSPD is shown. Starting point (a), a photon is absorbed by the nanowire and creates a hotspot (b). The supercurrent flows around the hotspot (c). A barrier across the nanowire is created (d). The bias current goes to a readout amplifier and creates a measurable output voltage. The hotpot cools down and the detector recovers for the next detection (e). On the bottom side an example is shown how a SNSPD signal looks like. It is a self-made oscilloscope measurement of the detector used in chapter 7.4. Top picture taken from [40, p.23] referring to [44, p.4]. The bottom picture is an oscilloscope data plot done in Python with a script written by Felix Pein.

SNSPD also have a non perfect quantum efficiency and a certain dark count rate, but typically the quantum efficiency reaches much higher values than a commercial APD and the dark count rates are quite small. Hence, the performance of a SNSPD beats an APD, but the price of an SNSPD is much higher.

3.4 Balanced homodyne detection

In this thesis different methods of balanced homodyne detection are used. The conventional homodyne detection with one balanced homodyne detector and the 8-port homodyne detection, which requires two balanced homodyne detectors measuring at the same time. The theoretical background for both methods is introduced.

3.4.1 Conventional homodyne detection

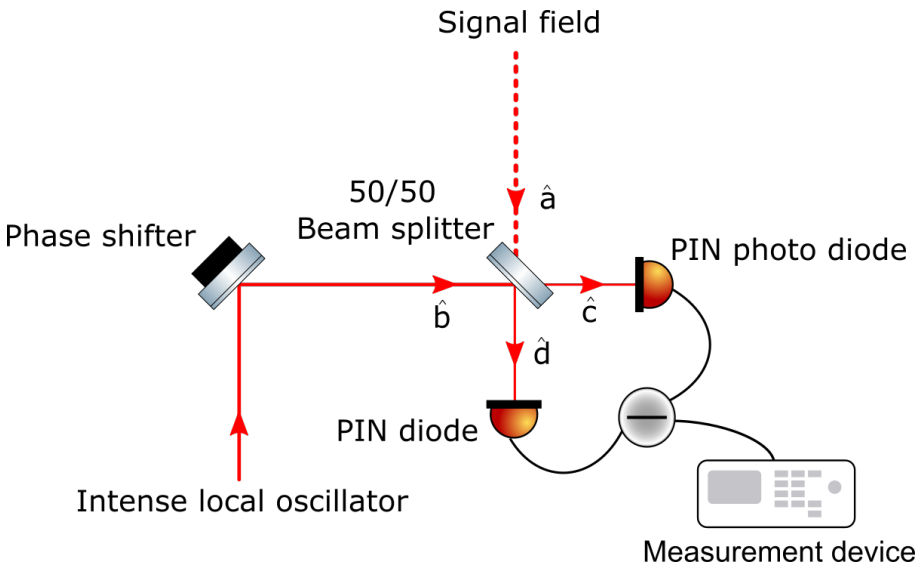

Figure 3.8: A balanced homodyne detector is shown. The signal field is overlapped with an intense local oscillator on a 50/50 beam splitter. The beam splitter output ports are measured with positive intrinsic negative (PIN) photo diodes. The difference signal of the PIN photo diode signals is created and can be read out with a measurement device. As measurement device either a spectrum analyzer or a data acquisition card are used. The measured quadrature can be defined with the phase shifter in the local oscillator path. Picture created with Inkscape referring to [5, p.168].

The conventional balanced homodyne detection is described in [5, p.167-169]. A signal field is overlapped with an intense local oscillator of the same

wavelength on a 50/50 beam splitter. Thereby the spatial modes of the signal field and local oscillator have to be matched to each other to reach a good interference contrast (visibility). In the output ports of the beam splitter, positive intrinsic negative (PIN) photo diodes are placed and the difference signal is created. The difference signal can be read out with a measurement device for example a spectrum analyzer or a data acquisition card. The phase of the local oscillator can be changed with a phase shifter and allows to decide which quadrature is measured. Figure 3.8 shows a balanced homodyne detector. The mathematical description follows.

The relation between input $(\hat{a}, \hat{b})$ and output $(\hat{c}, \hat{d})$ modes is given by:

$$\hat{c} = \frac{1}{\sqrt{2}}(\hat{a} + i\hat{b}) \,, \tag{3.10}$$

$$\hat{d} = \frac{1}{\sqrt{2}}(\hat{b} + i\hat{a}) \,. \tag{3.11}$$

The photo diode in mode $\hat{c}$ measures the intensity $I_c = \langle \hat{c}^\dagger \hat{c} \rangle$ and the photo diode in mode $\hat{d}$ measures the intensity $I_d = \left\langle \hat{d}^\dagger \hat{d} \right\rangle$. Hence, the differential signal has following formula:

$$I_c - I_d = \langle \hat{n}_{cd} \rangle = \left\langle \hat{c}^\dagger \hat{c} - \hat{d}^\dagger \hat{d} \right\rangle \,. \tag{3.12}$$

The differential signal can be expressed in terms of the incoming modes $(\hat{a}, \hat{b})$ by using equation 3.10 and equation 3.11:

$$\langle \hat{n}_{cd} \rangle = i \left\langle \hat{a}^\dagger \hat{b} - \hat{a} \hat{b}^\dagger \right\rangle \,. \tag{3.13}$$

Mode $\hat{b}$ is the intense local oscillator, which can be represented as a coherent state. Hence, the differential signal is:

$$\langle \hat{n}_{cd} \rangle = |\beta| (\hat{a} e^{i\omega t} e^{-i\Theta} + \hat{a}^\dagger e^{-i\omega t} e^{i\Theta}) \,, \tag{3.14}$$

with $\beta = |\beta| e^{-i\psi}$ and $\Theta = \psi + \frac{\pi}{2}$. The ω is the frequency of the local oscillator mode $\hat{b}$. For a homodyne detection the signal mode $\hat{a}$ should have the same frequency as the local oscillator and can be set to $\hat{a} = \hat{a}_0 e^{-i\omega t}$. The differential signal can be written as

$$\langle \hat{n}_{cd} \rangle = 2|\beta| \left\langle \hat{X}(\Theta) \right\rangle \,, \tag{3.15}$$

with the quadrature operator

$$\hat{X}(\Theta) = \frac{1}{2}(\hat{a}_0 e^{-i\Theta} + \hat{a}_0^\dagger e^{i\Theta}) \,. \tag{3.16}$$

The measured quadrature can be determined by controlling the phase Θ with the phase shifter in the local oscillator path.

3.4.2 8-port homodyne detection

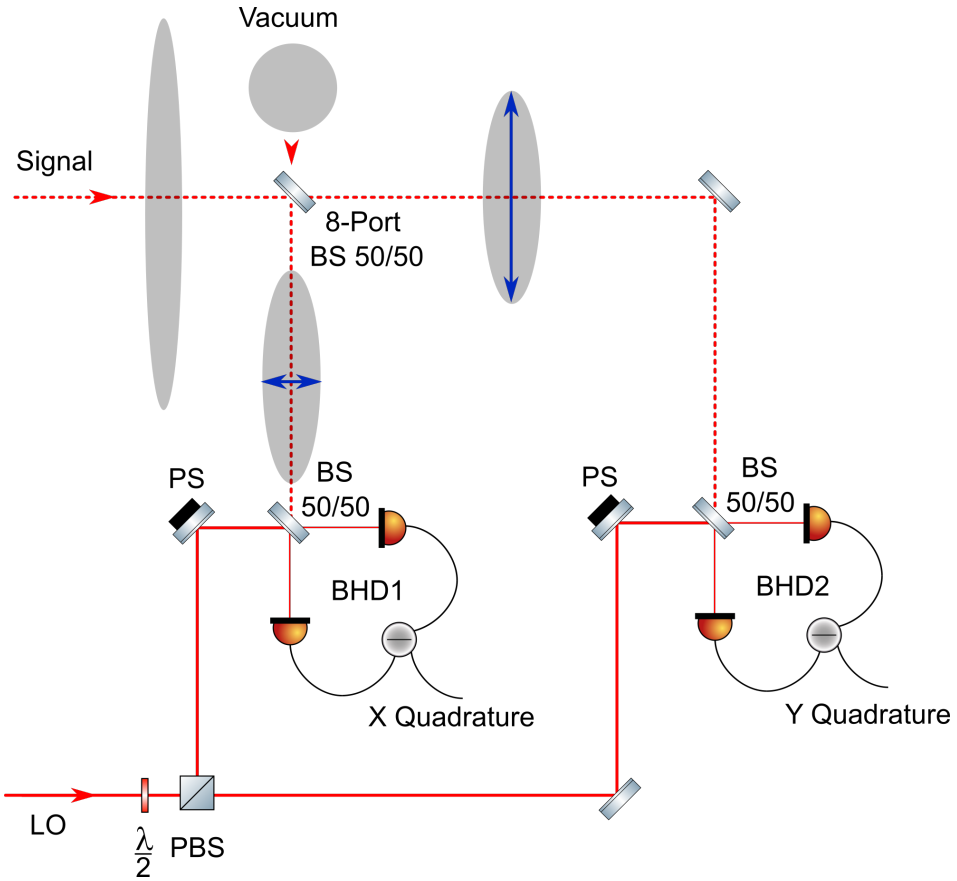

Figure 3.9: An 8-port homodyne detector is shown. It consists of two balanced homodyne detectors (BHD) from figure 3.8. The signal field is split on the 8-port beam splitter (BS) in two equal parts to be available for both BHDs at the same time. The splitting of the signal field introduces 50 % loss in each 8-port BS output port because a vacuum state couples in through the open 8-port BS input port. The local oscillator (LO) is also split with a half-wave plate ($\frac{\lambda}{2}$) and polarizing beam splitter (PBS) to be available for both detectors. The LO phase in BHD1 is stabilized to the squeezed quadrature while the phase in BHD2 is stabilized to the orthogonal anti-squeezed quadrature. The phases can be controlled with phase shifters (PS) in the local oscillator paths. The 8-port detection scheme allows to measure the Q-function of the signal field. Picture created with Inkscape referring to [28, p.150].

Information about the 8-port homodyne detection are taken from [8][28, p.144-171][45, p.49-51]. The central idea of 8-port homodyne detection is to split the signal in two equal parts and use two balanced homodyne detectors to read out orthogonal quadratures simultaneously. Of course, the splitting of the signal introduces 50 % loss. Hence, the simultaneous measurement of orthogonal quadratures is performed on vacuum smoothed out states. The 8-port detection scheme allows to measure the Q-function of the signal field. Figure 3.9 shows an 8-port homodyne detector. The mathematical description follows.

The relation between output $(\hat{c}, \hat{d})$ and input $(\hat{a}, \hat{v})$ modes on the 8-port beam splitter is given by:

$$\begin{pmatrix} \hat{c} \\ \hat{d} \end{pmatrix} = \frac{1}{\sqrt{2}} \begin{pmatrix} 1 & -1 \\ 1 & 1 \end{pmatrix} \begin{pmatrix} \hat{a} \\ \hat{v} \end{pmatrix} . \tag{3.17}$$

With equation 2.9 the amplitude quadrature measured at BHD1 can be expressed by

$$\hat{X}_c = \frac{1}{2}(\hat{c} + \hat{c}^\dagger) = \frac{1}{\sqrt{2}}(\hat{X}_a - \hat{X}_v) . \tag{3.18}$$

With equation 2.10 the phase quadrature measured at BHD2 can be expressed by

$$\hat{Y}_d = \frac{1}{2}(\hat{d} + \hat{d}^\dagger) = \frac{1}{\sqrt{2}}(\hat{Y}_a + \hat{Y}_v) . \tag{3.19}$$

The commutator for the vacuum smoothed out amplitude quadrature measurement at BHD1 and phase quadrature measurement at BHD2 vanishes:

$$[\hat{X}_c, \hat{Y}_d] = [(\hat{X}_a - \hat{X}_v), (\hat{Y}_a + \hat{Y}_v)] = 0 . \tag{3.20}$$

The probability distribution prd of X_c and Y_d represents the Q-function of the signal in front of the 8-port beam splitter.

$$prd(X_c, Y_d) = Q(X_a, Y_a) \tag{3.21}$$

The variances of the amplitude quadrature $\Delta^2\hat{X}_c$ and phase quadrature $\Delta^2\hat{Y}_d$ are:

$$\Delta^2\hat{X}_c = \frac{1}{2}(\Delta^2\hat{X}_a + \Delta^2\hat{X}_v) , \tag{3.22}$$

$$\Delta^2\hat{Y}_d = \frac{1}{2}(\Delta^2\hat{Y}_a + \Delta^2\hat{Y}_v) , \tag{3.23}$$

The variance before the 8-port beam splitter can be received by calculating out the in coupled vacuum state:

$$\Delta^2 \hat{X}_a = 2\Delta^2 \hat{X}_c - \Delta^2 \hat{X}_v \,, \tag{3.24}$$

$$\Delta^2 \hat{Y}_a = 2\Delta^2 \hat{Y}_d - \Delta^2 \hat{Y}_v \,. \tag{3.25}$$

Chapter 4

Optimization of the squeezed-light source

In my master thesis a squeezed-light source was built together with Daniela Abdelkhalek and Lorena Rebón [45, p.95-116][46]. In the course of this thesis the squeezed-light source could be improved. The optimization was part of the bachelor thesis from Maximilian Faden [47]. We found a way to decrease the optical loss and got higher squeeze levels than I had in my master thesis. In this chapter the experimental setup for a conventional squeezing measurement with one balanced homodyne detector is introduced. Furthermore, the characterization of the squeezed-light source with two balanced homodyne detectors is shown. The chapter ends with a v-class entanglement measurement, which was also part of Malte Lautzas master thesis [48, p.55].

4.1 Experimental setup

Figure 4.1 shows the setup for a conventional squeezing measurement. For greater clarity not every used component is shown. A Nd:YAG laser at a wavelength of 1064 nm was used. It was bought from the company "Innolight". The laser had an integrated second harmonic generation where a certain amount of 1064 nm light was converted to 532 nm light. The out coupled laser power at a wavelength of 1064 nm was around 350 mW. The available power of the 532 nm light was around 800 mW. The reported powers in this whole thesis were measured with a power meter (Ophir Nova II). It was a pretty old device, the last calibration was many years ago and some parts on the active area were damaged. Therefore, all given powers in this thesis have an estimated relative error of $\pm 10\,\%$. More information about the laser can be found in [49, p.43-46]. The spatial modes of the laser beams were not perfectly in a TEM 00 mode. For the 532 nm light this was no problem, but for the 1064 nm light it was important to have a clean TEM 00 mode, therefore,

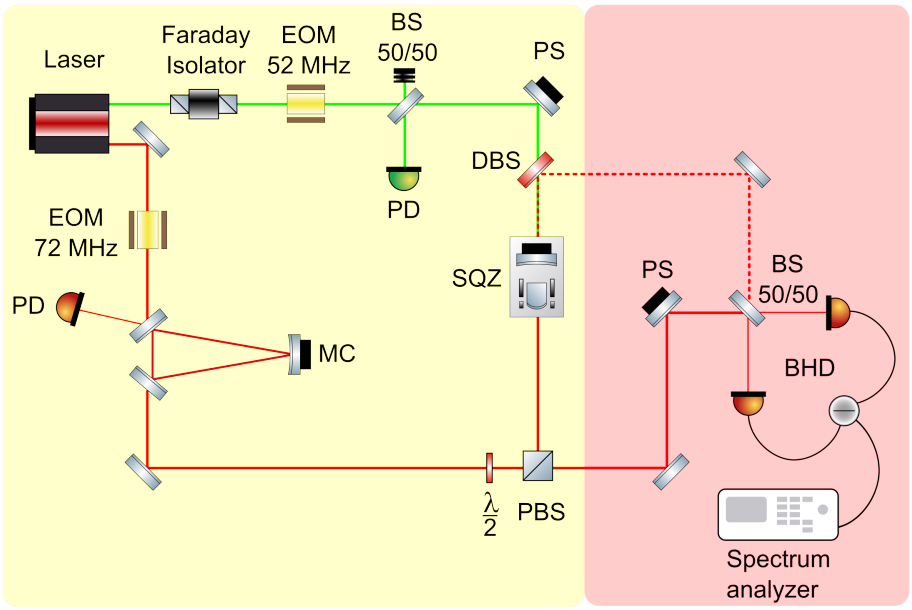

Figure 4.1: Simplified setup for a conventional squeezing measurement. The yellow area shows the squeezing generation and the red area shows a conventional balanced homodyne detector. The red light (1064 nm) was sent through an electro optical modulator (EOM) and passed a mode cleaner (MC), which was stabilized to resonance by a photo diode (PD) in reflection with the Pound-Drever-Hall technique. The red light was split with a half-wave plate ($\frac{\lambda}{2}$) and a polarizing beam splitter (PBS). One part was sent as control field to the squeezing resonator (SQZ) the other part was sent as local oscillator to the balanced homodyne detector (BHD). The phase of the local oscillator could be controlled with a phase shifter (PS). The green light (532 nm) was sent through a Faraday isolator and an EOM. Then it passed a beam splitter (BS), a PS and a dichroic beam splitter (DBS). The green light was converted inside the SQZ to squeezed-light at 1064 nm. The SQZ was stabilized to resonance by a PD in reflection. The squeezed signal was reflected by the DBS and was sent into the BHD where it was overlapped with the local oscillator. The difference signal of the BHD PDs was read out with a spectrum analyzer. Picture created with Inkscape.

a ring cavity (mode cleaner) was used. To stabilize the length of the mode cleaner to resonance of the TEM 00 mode, the Pound-Drever-Hall technique was used by detecting light in reflection of the mode cleaner [50]. Therefore, a phase modulation far away from the linewidth of the mode cleaner was necessary. The modulation frequency was 72 MHz, it was imprinted on the 1064 nm light by sending it through an electro optical modulator. The linewidth (full width half maximum: FWHM) of the mode cleaner was 751 kHz for s-polarized light with a finesse of 950 and a roundtrip length of 42 cm. For p-polarized light the finesse was lower and the linewidth was

accordingly larger, but all optics in the experiment were optimized for s-polarized light so the mode cleaner was always stabilized to the s-polarized mode. Because of the ring cavity geometry, the mode cleaner also acted as polarization filter. The modes for s-polarized light and p-polarized light were on resonance for different resonator lengths. When the mode cleaner length was stabilized to the s-polarized mode, the p-polarized mode was filtered out. Furthermore, the resonator acted as a low pass filter in the frequency domain and suppressed laser noise outside its linewidth. The filtered 1064 nm light was divided into two parts by using a half-wave plate and a polarizing beam splitter. One part was sent into the balanced homodyne detector as local oscillator, the other part was sent to the squeezer as control field.

The 532 nm light traveled through a Faraday isolator to avoid back reflections in the second harmonic generation. A phase modulation of 52 MHz was imprinted by an electro optical modulator to be able to use the Pound-Drever- Hall method to stabilize the length of the squeezing resonator with the light in reflection. The squeezing resonator had the geometry of a linear cavity, so the reflected light had to be separated from the incoming light. Therefore, a 50/50 beam splitter was used, which threw away 50 % of the incoming power, but made it also possible to detect 50 % of the back reflected light on a photo diode for the Pound-Drever-Hall stabilization. After this 50/50 beam splitter the 532 nm light was sent to a mirror, which could be moved with a piezoelectric element and acted as a phase shifter. In front of the squeezing resonator was a dichroic beam splitter (DBS), which transmitted the 532 nm light. The 532 nm light was coupled in the squeezing resonator as pump field and created a squeezed vacuum with a wavelength around 1064 nm by a nonlinear process in a periodically poled potassium titanyl phosphate (PPKTP) crystal with the dimensions of 1 mm x 2 mm x 5 mm. The squeezed vacuum was coupled out on the same side where the 532 nm light was coupled in. The coupling mirror had a reflectivity of 89 % for 1064 nm and 97.5 % for 532 nm. The DBS separated the squeezed field from the pump by reflecting 1064 nm light while the 532 nm back reflected light was transmitted. The squeezed-light had only a very small intensity, so it was not possible to use it for aligning the optical paths. Therefore, the control field could be used. It was sent to the high reflective backside of the squeezing resonator. The PPKTP crystal itself acted as a mirror by having coatings for both wavelength and a curvature of r = 10 mm. A small amount of the control field could be transmitted through the squeezing resonator and it propagated in the same mode as the squeezed field. If the control field was

good aligned, the squeezed field was also be good aligned. The squeezed field was sent into a balanced homodyne detector where it was overlapped with the local oscillator of the same wavelength on a 50/50 beam splitter. This allowed to measure and characterize the amount of squeezing by detecting the overlapped signal with two photo diodes. Their differential signal was read out with a spectrum analyzer to achieve the noise of the signal scaled with the power of the local oscillator. In the local oscillator path a mirror, which could be moved with a piezoelectric element, was placed to be able to control the phase of the local oscillator. This gave the opportunity to define the quadrature which was measured. For the theoretical background of a balanced homodyne detection see chapter 3.4.

4.2 Squeezing measurement preparations

Before a squeezing measurement could be done, a few preparations were necessary. The Pound-Drever-Hall locks had to be activated, the temperature of the PPKTP crystal needed the right value to fulfill the quasi-phase matching condition and the mode of the squeezed field had to be overlapped with the mode of the local oscillator to get a good interference contrast.

4.2.1 Pound-Drever-Hall locks

The theoretical background about the Pound-Drever-Hall technique can be found in [50]. In this subsection only the experimental realization is described. Figure 4.2 visualizes the Pound-Drever-Hall technique for the stabilization of the mode cleaner and squeezing resonator lengths. Both locks follow the same idea: a phase modulation was imprinted on the incoming laser beam with an electro optical modulator. A photo diode was placed in reflection of the resonator. The signal of the photo diode was mixed with the same frequency as was used for the electro optical modulator. This generated an error signal, which could be sent into a proportional-integral-derivative (PID) controller. The PID controller was connected with a high voltage amplifier, which controlled the length of the resonator through a piezoelectric actuated mirror. The stabilization point was set to have a minimal possible signal on the photo diode in reflection.

To activate a Pound-Drever-Hall lock, the resonator length was manually tuned to the resonance of the TEM 00 mode. Then the PID controller was switched on, that stabilized the resonator length to the TEM 00 mode

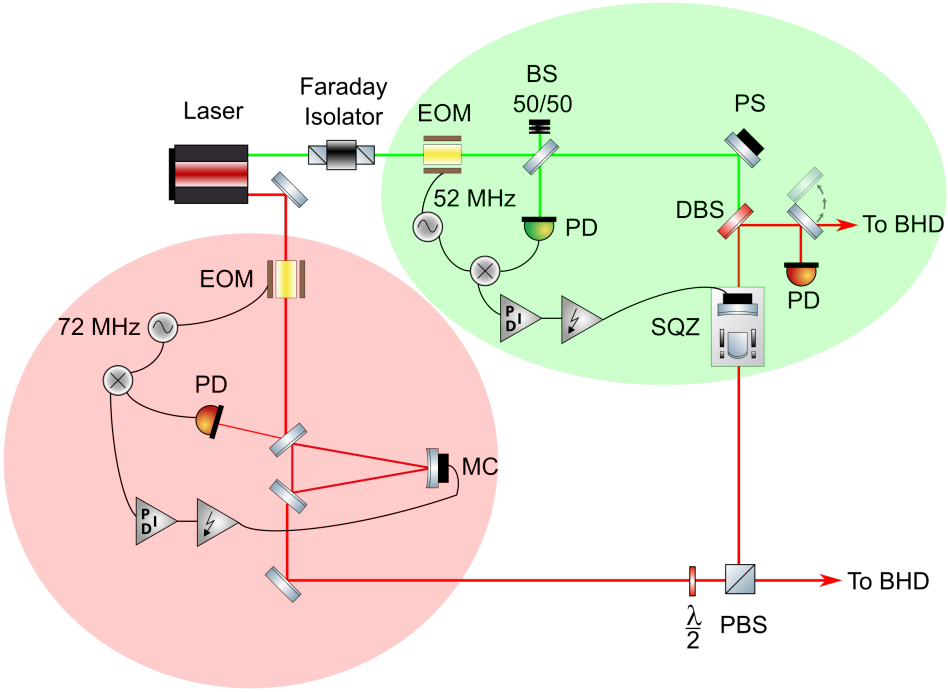

Figure 4.2: Simplified setup for the Pound-Drever-Hall locks. The red area indicates the Pound-Drever-Hall lock of the mode cleaner (MC) length. The green area indicates the Pound-Drever-Hall lock of the squeezing resonator (SQZ) length. The principle idea was exactly the same for both resonators, only different modulations frequencies were used (72 MHz for the MC and 52 MHz for the SQZ). The modulation frequency was imprinted on the incoming laser beam with an electro optical modulator (EOM). In reflection of the resonator a photo diode (PD) was placed. The signal of the photo diode was mixed with the same frequency as used for the EOM. This generated an error signal, which could be sent into a proportional-integral-derivative (PID) controller. The PID controller was connected with a high voltage amplifier, which controlled the length of the resonator through a piezoelectric actuated mirror. The stabilization point was set to have a minimal possible signal on the photo diode in reflection. Picture created with Inkscape.

automatically. For the mode cleaner lock any resonator length which was resonant for the 1064 nm TEM 00 mode could be used. But for the squeezing resonator lock it was important to choose the correct length. The squeezing resonator was stabilized with the 532 nm pump field, but should also be on resonance for the squeezed field at 1064 nm. Therefore, the cavity length had to be chosen to a length which fulfilled the resonance condition for both wavelengths simultaneously. That was only every second resonance of the 532 nm TEM 00 mode. Figure 4.3 shows which resonances of the 532 nm pump field could be used for the Pound-Drever-Hall lock to be on resonance with the 1064 nm field at the same time. Even when the 532 nm light was stabilized to the correct peak it was still possible that the 1064 nm light was

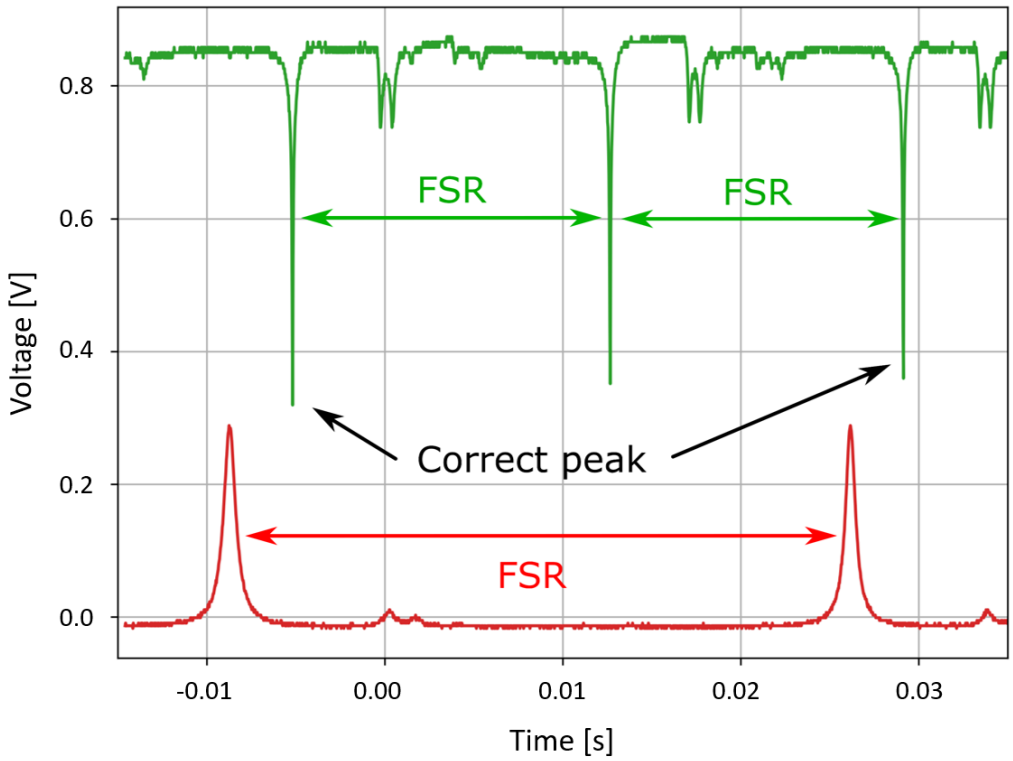

Figure 4.3: Oscilloscope signals for the squeezing resonator length stabilization via Pound-Drever-Hall technique. The modes from the 532 nm light to the squeezing resonator are visible (green), measured in reflection. The modes from the 1064 nm light to the squeezing resonator are visible (red), measured in transmission. In one FSR of the 1064 nm light field two FSRs of the 532 nm light field can be seen. The squeezing resonator should be on resonance for both wavelength at the same time. Therefore, the Pound-Drever-Hall lock, which used the green light, had to be activated with the correct peak. By fine tuning the squeezing-crystal temperature it was possible to overlap the correct green mode with the red mode. Oscilloscope data plot done in Python with a script written by Felix Pein.

not on resonance. To made 532 nm and 1064 nm simultaneously resonant, the temperature of the squeezing-crystal could be tuned, which is explained in the following subsection.

4.2.2 Squeezing-crystal temperature

The squeezing-crystal needed a certain temperature to fulfill the quasi-phase matching condition, which is explained in chapter 3.1. Additionally, the simultaneous resonance of 532 nm and 1064 nm was achieved with the temperature setting. A design with two temperature controllers was used, invented by Axel Schönbeck [51, p.39-43]. Figure 4.4 visualizes the two temperature

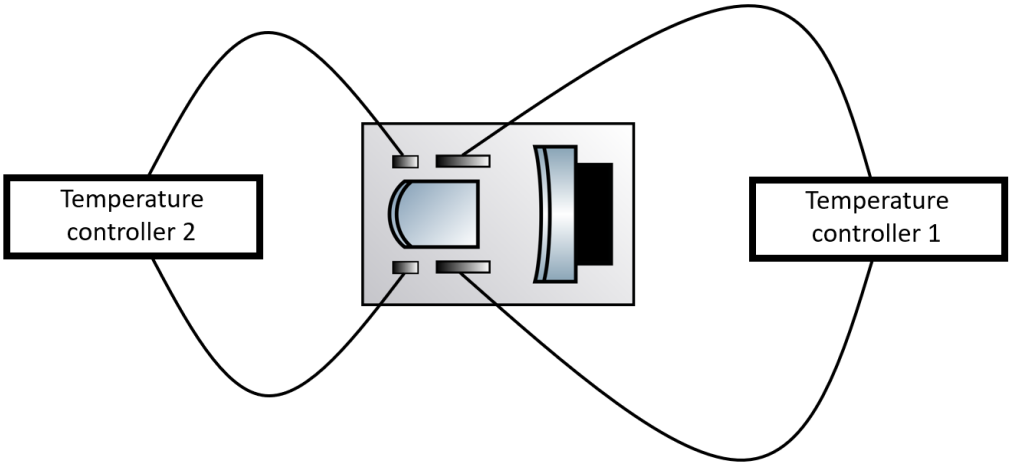

Figure 4.4: Squeezing-crystal temperature controllers. Two temperature controllers were used to stabilize the squeezing-crystal temperature. The first temperature controller was responsible for the central area of the crystal. In this zone the waist of the pump field arrived and did mainly the parametric down conversion. Therefore, the quasi-phase matching condition should be fulfilled by setting the necessary temperature on controller 1. The second temperature controller was responsible for the crystal backside where the coating was placed. The temperature for controller 2 was set in a way that both wavelength (532 nm +1064 nm) were simultaneously on resonance. The two temperature design was invented by Axel Schönbeck [51, p.39-43]. Picture created with Microsoft Power Point.

design for the squeezing-crystal temperature stabilization. Temperature controller 1 was used to achieve the quasi-phase matching in the central area of the crystal where the waist of the pump field arrived and did the mainly parametric down conversion. Temperature controller 2 was used for the simultaneous resonance of both wavelength (532 nm +1064 nm). Typically both temperature controllers were used with a temperature around 33 °C.

4.2.3 Mode matchings to a diagnostic mode cleaner

For experiments based on squeezed-light the optical loss is a limiting property, as can be seen in chapter 3.1. Beside the intrinsic loss sources of the used optics, the interference contrast (visibility) between squeezed field and local oscillator can strongly influence the total optical loss. To minimize the optical loss in the experiment the interference contrast should be as good as possible. In the ideal case the squeezed field and the local oscillator have exactly the same transversal mode at the 50/50 beam splitter of the balanced homodyne detector. To reach the same mode properties, a trick was used: both fields

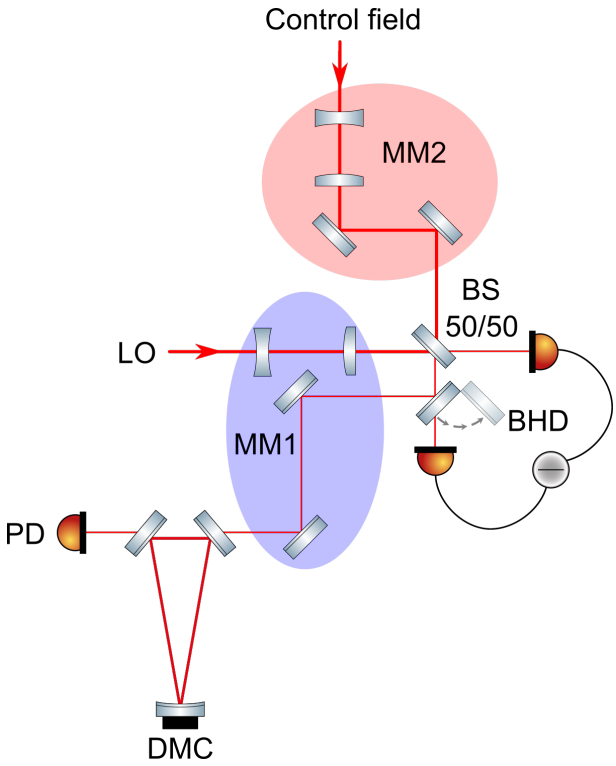

Figure 4.5: Diagnostic mode cleaner setup to reach a good interference contrast. At the beginning the local oscillator (LO) was sent via a flip mirror inside the balanced homodyne detector (BHD) to the diagnostic mode cleaner (DMC). The length of the DMC was periodically scanned and the modes could be read out with a photo diode (PD) in transmission of the DMC. The mode of the LO was matched to the DMC. Therefore, two mirrors and two lenses were used (MM1, blue area). Afterwards the control field was also matched to the DMC with two mirrors and two lenses (MM2, red area). When both fields were matched to the DMC, they were overlapped on the 50/50 beam splitter of the BHD. Picture created with Inkscape.

were sent via a flip mirror to a resonator (diagnostic mode cleaner). Figure 4.5 visualizes the setup for getting a good visibility. At the beginning, the local oscillator was matched to the diagnostic mode cleaner as good as possible. Therefore, two lenses and two mirrors were used to be able to control all necessary degrees of freedom of the spatial mode like height propagation, side propagation, waist size and waist position. To see the modes on the diagnostic mode cleaner a photo diode in transmission of the resonator was used and the length of the resonator was periodically scanned by applying an oscillating voltage to the piezoelectric element of the resonator mirror. When the mode matching from the local oscillator was done, the control field was also matched to the diagnostic mode cleaner as good as possible. When both fields were matched to the diagnostic mode cleaner in a very good way, then

the spatial modes were overlapped in the whole path and, consequently, they were also overlapped on the 50/50 beam splitter of the balanced homodyne detector. The mode matchings to the diagnostic mode cleaner in this thesis were typically in the area around 99 %. In figure 4.7, posterior this chapter, a mode matching to the diagnostic mode cleaner is shown.

The local oscillator mode matching was easy to do because a constant power level reached the diagnostic mode cleaner. For the control field the situation was more complicated. The control field was in s-polarization and to reach the diagnostic mode cleaner it had to be transmitted by the squeezing resonator, which was stabilized to resonance with a Pound-Drever-Hall lock. For this resonator length stabilization, the pump field in s-polarization was used. With this configuration the parametric down conversion process started and leaded to a phase sensitive amplification and deamplification of the control field. In the experiment was no phase stabilization for pump or control field available. Hence, phase fluctuations occurred, which leaded to a fluctuating control field intensity. Doing a mode matching with a fluctuating intensity was still possible, but required some practice.

4.3 Squeezing measurement with one balanced homodyne detector

When all preparations were done, the squeezing measurement could be executed. Therefore, the signal of the balanced homodyne detector was read out with a spectrum analyzer. The theoretical background about such a conventional homodyne detection can be read in chapter 3.4.1. Typical settings of the spectrum analyzer for a squeezing measurement were a sideband frequency of 5 MHz with a resolution bandwidth (RBW) of 300 kHz and a video bandwidth (VBW) of 300 Hz. The sweep time was set to 300 ms and 4 traces were recorded. One trace represented the dark noise and was measured while no light was sent to the balanced homodyne detector. Another trace was the vacuum level, which was measured while the local oscillator was sent to the balanced homodyne detector, but without any signal field. And of course the traces for the maximum squeezing and anti-squeezing were measured. Therefore, the signal field and the local oscillator were sent to the balanced homodyne detector at the same time and the phase of the local oscillator was set in a way that the signal on the spectrum analyzer was minimal (squeezed quadrature) or maximal (anti-squeezed quadrature). For the results in this

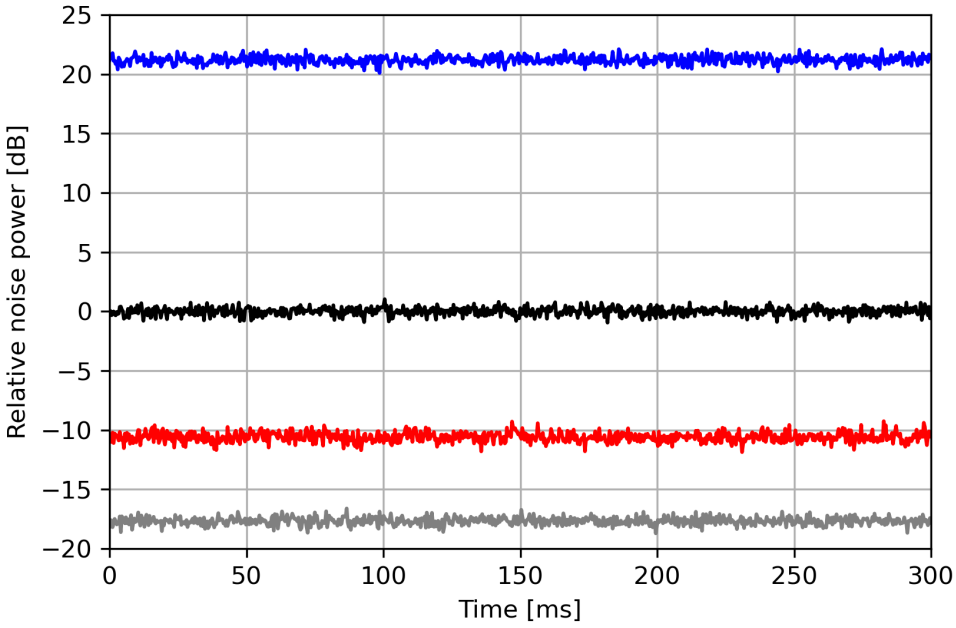

Figure 4.6: Result of the conventional squeezing measurement. The relative noise power in dB is plotted against the measurement time in ms. The anti-squeezed trace (blue) was 21.2 dB above the vacuum level (black). The squeezed trace (red) was 10.6 dB below the vacuum level. The dark noise (grey) was 17.7 dB below the vacuum level. The phase of the local oscillator was stabilized by hand. Settings for the measurement: sideband frequency = 5 MHz, RBW = 300 kHz, VBW = 300 Hz, sweep time = 300 ms and pump power in front of the squeezer = 25 mW. The setup for this measurement is shown in figure 4.1. Data evaluation done in Python with a script written by Malte Lautzas.

chapter the phase stabilization to the maximal or the minimal noise level was done by hand. In chapter 5 another phase locking technique is introduced, which allows to stabilize the phase for longer time scales automatically.

Figure 4.6 shows the result of a conventional squeezing measurement. All of the squeezing data evaluations and plots in this thesis were done with a Python script mainly written by Malte Lautzas. The measured traces were normalized to the vacuum level. Hence, the relative noise power in dB is shown and the vacuum trace is on 0 dB. For the squeezed quadrature a value of -10.6 dB was reached while the anti-squeezed quadrature was 21.2 dB. The dark noise clearance was 17.7 dB for a local oscillator power of 18 mW in front of the beam splitter from the balanced homodyne detector.

When a dark noise correction was done by subtracting the dark noise from all other traces a dark noise corrected squeeze value of -11.5 dB and a dark noise corrected anti-squeeze value of 21.3 dB could be evaluated. For

this calculation it is important to switch the dB values into a linear scale then perform the subtraction and transform the results back to a dB scale. From the dark noise corrected values, the optical loss could be calculated with equation 3.2 and lead to a value of 6.5 %. In accordance with equation 3.3 the initial squeezing could be calculated to 21.6 dB. For this measurement a pump power of 25 mW in front of the squeezer was used. Because of a bad mode matching of the pump field to the squeezer only around 70 % of this power was coupled in the squeezing resonator. The green trace in figure 4.3 visualizes the bad mode matching.

In my master thesis the same measurement was done, but there the optical loss was higher and the resulting squeeze level was lower [46, p.26-27]. The dark noise corrected squeeze value was -8.3 dB and the dark noise corrected anti-squeeze value was 19.4 dB. An optical loss of 13.9 % and an initial squeezing of 20.0 dB were calculated. The pump power and dark noise clearance were in the same order as for the improved measurement. The reason for the higher loss in my master thesis was a bad visibility caused by another implementation of the preparation steps. In subsection 4.2.3 the procedure of doing the mode matchings is described. Therefore, the mode matching of the control field was done while phase sensitive power fluctuations were visible. For the measurement in my master thesis the control field was turned to p-polarization before it was sent into the squeezing resonator by using a half-wave plate to avoid the power fluctuations. Mode matchings are in general much easier to do when the power level is constant. We thought the spatial mode of the control field for s-polarization and p-polarization should be exactly the same and it makes no difference which polarization is used to do the mode matching to the diagnostic mode cleaner. But this was an incorrect assumption. The spatial mode of the control field was different for s-polarization and p-polarization. Figure 4.7 visualizes the difference between a control field in s-polarization and a control field in p-polarization. In figure 4.7 the mode matching to the diagnostic mode cleaner was done for a control field in s-polarization as good as possible. Then the polarization was turned to p-polarization with a half-wave plate in front of the squeezing resonator. A significant additional peak appeared in the mode matching on the diagnostic mode cleaner. This peak was identified with a Thorlabs beam profiler as a higher order height mode. Hence, the spatial mode between squeezing resonator and diagnostic mode cleaner had a different height propagation for s-polarization and p-polarization. Probably the difference was caused by the nonlinear PPKTP crystal.

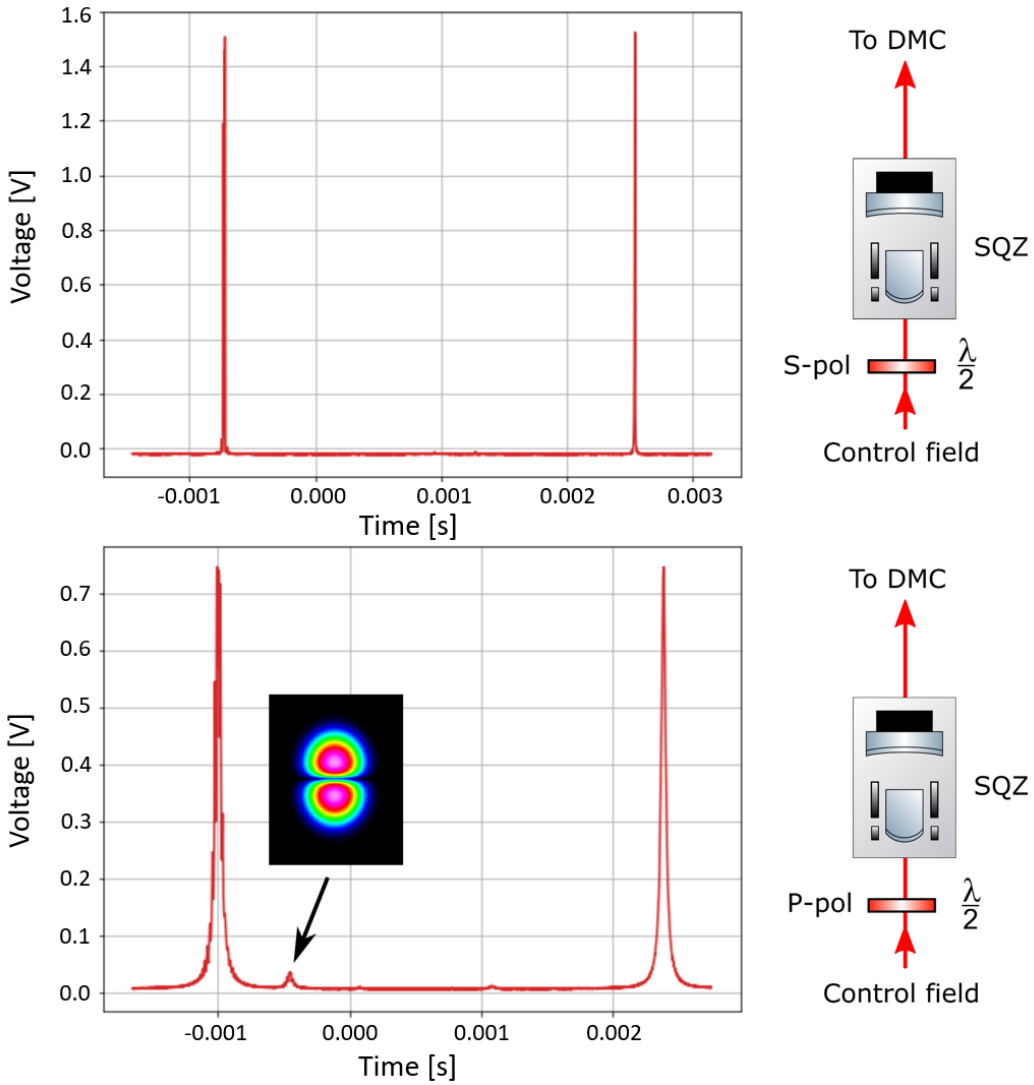

Figure 4.7: Mode matching from the control field to the diagnostic mode cleaner (DMC). Top: the control field was set to s-polarization (s-pol) with a half-wave plate ($\frac{\lambda}{2}$) in front of the squeezing resonator (SQZ). Bottom: the polarization was turned to p-polarization (p-pol) by using the half-wave plate in front of the SQZ. An additional peak in the bottom picture appeared, which could be removed with the height screws of the mode matching mirror set. Obviously, the mode of the control field in transmission of the SQZ had a different height propagation for s-pol and p-pol. Picture created with Inkscape, oscilloscope plot was done with a Python script written by Felix Pein and the mode profile was measured with a beam profiler from Thorlabs.

The generated squeezing was in s-polarization, therefore, it was important to do the mode matching with a control field in s-polarization to be sure that the control field represented the spatial mode of the squeezed field.

4.4 Squeezing measurements with two balanced homodyne detectors

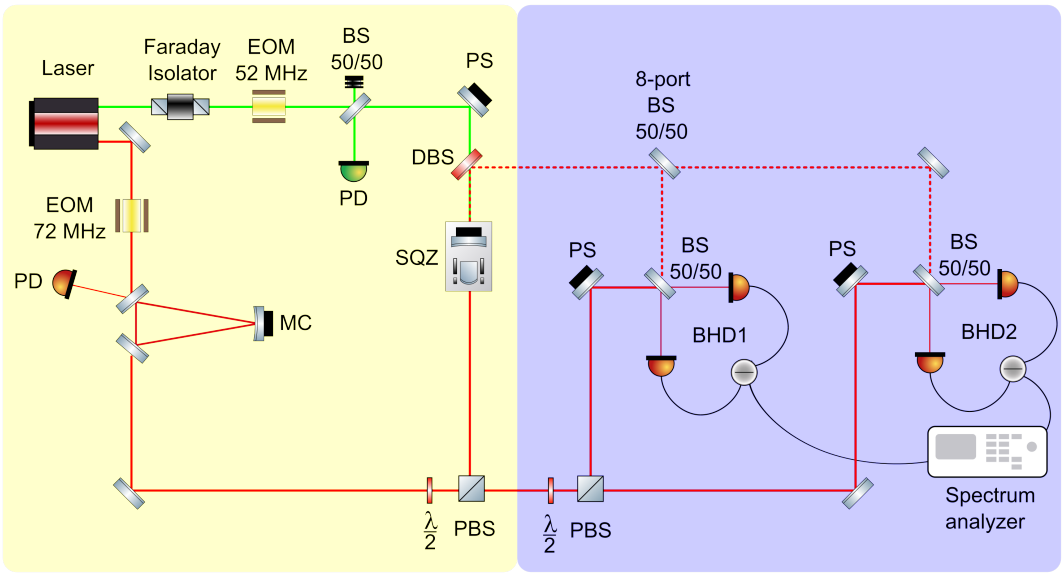

Figure 4.8: Simplified setup for squeezing measurements with two balanced homodyne detectors. The yellow area shows the squeezing generation and the blue area shows an 8-port homodyne detector. The setup is the same as in figure 4.1 with an additional balanced homodyne detector (BHD). The squeezed field was split on a 50/50 beam splitter (8-port BS) to send 50 % of the signal in each BHD. The local oscillator was split with a half-wave plate ($\frac{\lambda}{2}$) and a polarizing beam splitter (PBS). Picture created with Inkscape.

For the planned experiment an 8-port homodyne detection was necessary, which is theoretically explained in chapter 3.4.2. For an 8-port homodyne detection a second balanced homodyne detector was necessary and the signal field was split with a 50/50 beam splitter as can be seen in figure 4.8. With an additional half-wave plate and a polarizing beam splitter, a local oscillator could be sent to both detectors. To characterize the losses in the 8-port paths, a conventional squeezing measurement along the 8-port paths was performed. Therefore, the same 4 traces as in section 4.3 were recorded consecutively for both balanced homodyne detectors. Of course, this was no real 8-port measurement because from definition an 8-port measurement is a simultaneously measurement with both balanced homodyne detectors (BHD). Real 8-port measurements are presented in chapter 7.

The spectrum analyzer had the same settings as in section 4.3. For BHD1 the anti-squeezed trace was 15.3 dB and the squeezed trace was -2.6 dB. The dark noise clearance was 17.0 dB for a local oscillator power of 18 mW in

front of the beam splitter from the balanced homodyne detector. For BHD2 the anti-squeezed trace was 15.7 dB and the squeezed trace was -2.6 dB. The dark noise clearance was 18.6 dB for a local oscillator power of 18 mW in front of the beam splitter from the balanced homodyne detector.

Figure 4.9 shows the normalized results for both balanced homodyne detectors. Formula 3.24 and 3.25 allowed to calculate out the loss from the 50/50 8-port beam splitter. The reconstructed squeeze value without the 50 % beam splitter loss for BHD1 was -10.2 dB and the anti-squeeze value was 18.2 dB. When also a dark noise correction was applied to the data, the dark noise corrected reconstructed values were -11.1 dB for the squeezed quadrature and 18.3 dB for the anti-squeezed quadrature. From this values an optical loss of 6.4 % and an initial squeezing of 18.6 dB could be calculated with equations 3.2 and 3.3. For BHD2 the reconstructed values were -10.1 dB squeezing and 18.7 dB anti-squeezing and the dark noise corrected reconstructed values were -10.7 dB squeezing and 18.7 dB anti-squeezing. From this values an optical loss of 7.4 % and an initial squeezing of 19.0 dB could be calculated with equations 3.2 and 3.3. Both detectors gave more or less the same results. A perfect agreement was very unrealistic to reach because a lot of factors influenced the losses in the two paths and could explain the difference. For example, different mode matchings, different amount or quality of optics, non perfect 50/50 splitting of the signal or slightly different quantum efficiencies of the balanced homodyne detector photo diodes. The reconstructed values were also similar to the results from the conventional squeezing measurement where the whole signal was detected with one balanced homodyne detector in the previous section 4.3.

In my master thesis a similar measurement was done [46, p.28-29]. With BHD1 the squeezed quadrature was measured as -2.3 dB and with BHD2 the anti-squeezed quadrature was measured as 14.2 dB. For the reconstructed dark noise corrected values a squeezed quadrature of 7.0 dB and an anti-squeezed quadrature of 17.2 dB were reported. The calculated optical loss was 18.7 % and the initial squeezing was 18.1 dB. Here a strong optimization is visible, which has the same explanation as was given in section 4.3.

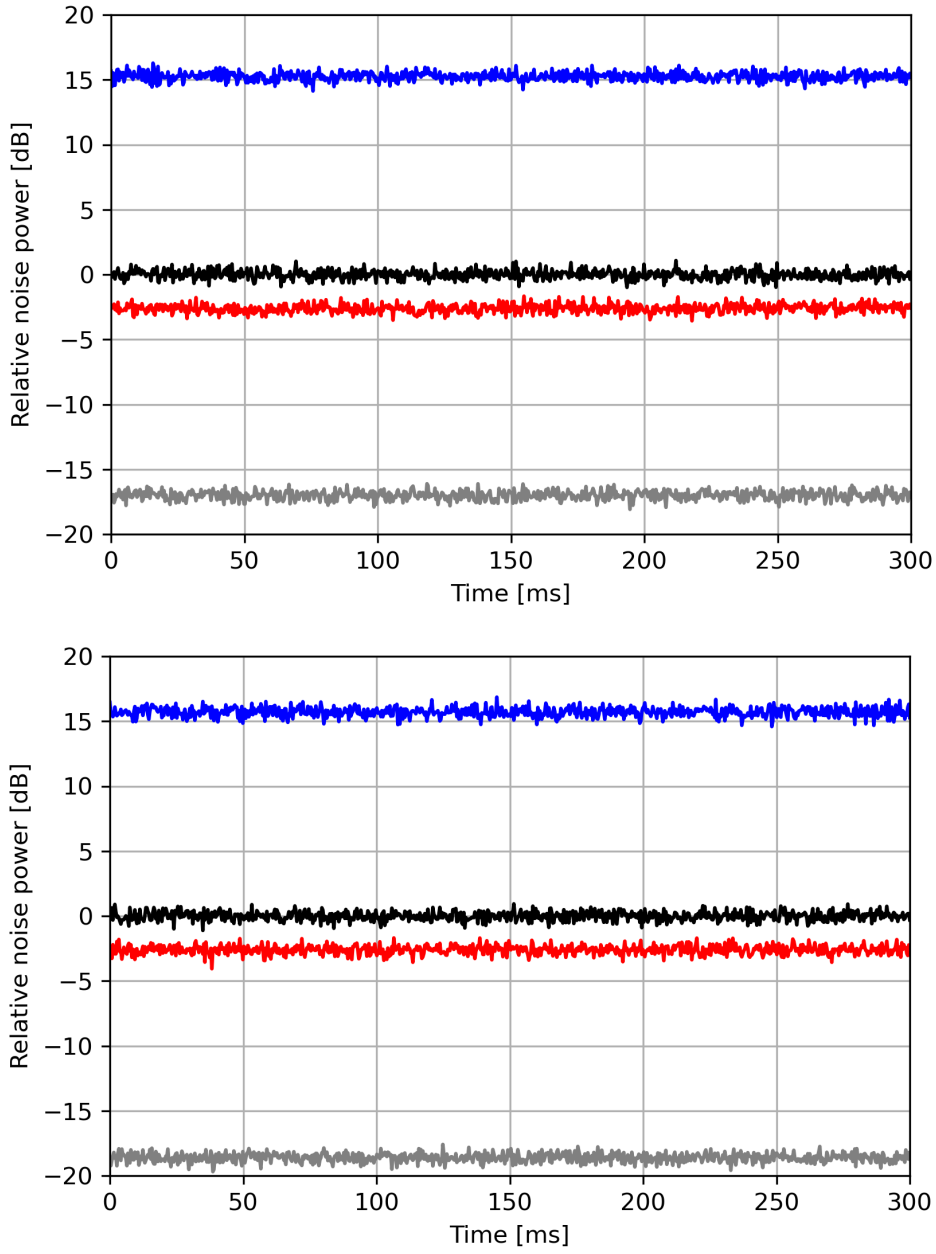

Figure 4.9: Results for a squeezing measurement along the 8-port paths for BHD1 (top) and BHD2 (bottom). The relative noise power in dB is plotted against the measurement time in ms. The anti-squeezed trace (blue) was 15.3 dB for BHD1 and 15.7 dB for BHD2 above the vacuum level (black). The squeezed trace (red) was 2.6 dB below the vacuum level for both BHDs. The dark noise (grey) was 17.0 dB below the vacuum level for BHD1 and 18.6 dB for BHD2. The phase of the local oscillator was stabilized by hand. Settings for the measurement: sideband frequency = 5 MHz, RBW = 300 kHz, VBW = 300 Hz, sweep time = 300 ms and pump power in front of the squeezer = 25 mW. The setup for this measurement is shown in figure 4.8. Data evaluation done in Python with a script written by Malte Lautzas.

4.5 Entanglement measurement

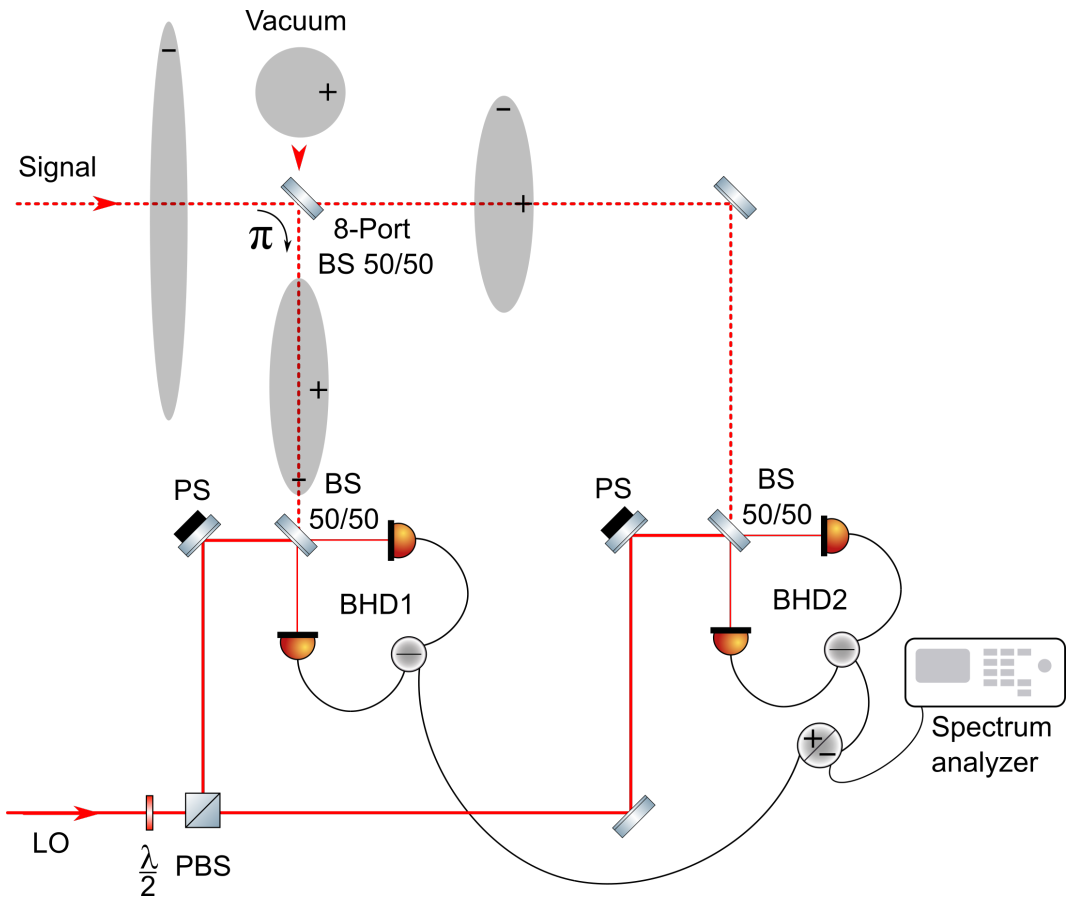

Figure 4.10: Simplified setup for an entanglement measurement. The signal was split on the beam splitter (8-port BS), this introduced 50 % loss (half a vacuum state) for the split signals, which were sent to the balanced homodyne detectors (BHD). This process delivered correlations and anti-correlations between BHD1 and BHD2 (indicated with the + and - signs inside the split states). The sum or difference of the BHD signals was created by a self built electronic device from former group members. The sum and the difference signal were read out with a spectrum analyzer and characterized the states in front of the 8-port BS. Picture created with Inkscape.

So far, the BHDs were used consecutively. For the following measurement both BHDs were used at the same time. The 8-port homodyne detection setup, where the signal field was split at a 50/50 beam splitter, was exactly what is known as v-class entanglement [52][53][54]. This means that there were correlations and anti-correlations between the quadratures in the vacuum smoothed out states on BHD1 and BHD2. By measuring the same quadrature at the same time with both BHDs, the quadratures of the in coupled states of the 8-port beam splitter can be achieved. One beam splitter

input was a squeezed state without the 50 % loss from the 8-port beam splitter, the other beam splitter input was a vacuum state. To characterize the in coupled states, the sum and difference of the BHD signals were read out with a spectrum analyzer. Figure 4.10 visualizes the setup for a v-class entanglement measurement, which was nearly the same setup as in figure 4.8. The only difference was an additional electronic box in figure 4.10, which added or subtracted the BHD signals.

In figure 4.11 the spectrum analyzer measurement is shown. For this measurement the local oscillators in BHD1 and BHD2 were both stabilized to the maximal squeezing at the same time to characterize the maximal squeezing of the squeezed state without the 50 % loss from the 8-port beam splitter. Afterwards both local oscillators were stabilized to the maximal anti-squeezing to characterize the maximal anti-squeezing of the squeezed state without the 50 % loss from the 8-port beam splitter. In addition, measurements were done where one local oscillator was stabilized to the maximal squeezing or anti-squeezing while the other local oscillator was periodically scanned. It is clearly visible that the oscillating traces have a local minimum exactly on the vacuum level at certain time points, as expected for v-class entanglement [54]. The spectrum analyzer had the same settings as in section 4.3. The measured traces were normalized to the vacuum level. Hence, the relative noise power in dB is shown and the vacuum trace is on 0dB. For the squeezed trace a value of -9.0 dB could be reached while the anti-squeezed trace was 17.3 dB. The dark noise clearance was 15.6 dB for a local oscillator powers of 18 mW for BHD1 and 13 mW for BHD2, measured in front of the beam splitters of the balanced homodyne detectors. Different local oscillator powers were necessary to have the same absolute vacuum levels. If the absolute vacuum levels were different, the entanglement measurement was destroyed because the sum and difference of the BHD signals gave not out exactly the in coupled states. This could be seen in the oscillating traces which had no local minimum on the vacuum level anymore.

When a dark noise correction was done by subtracting the dark noise from all other traces a dark noise corrected squeeze value of -10.0 dB and a dark noise corrected anti-squeeze value of 17.4 dB could be evaluated. From the dark noise corrected values the optical loss could be calculated with equation 3.2 and lead to a value of 8.4 %. In accordance with equation 3.3 the initial squeezing could be calculated to 17.8 dB. For this measurement a pump power of 25 mW in front of the squeezer was used. Because of a bad mode matching of the pump field to the squeezer only around 70 % of this power

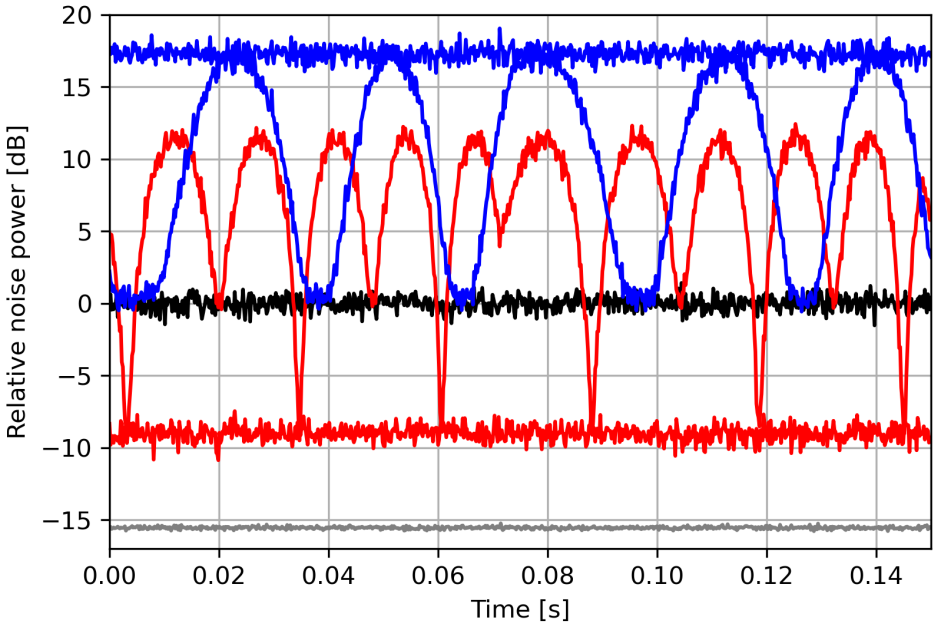

Figure 4.11: Result for a v-class entanglement measurement. The relative noise power in dB is plotted against the measurement time in s. The anti-squeezed trace (blue) was 17.3 dB above the vacuum level (black). The squeezed trace (red) was 9.0 dB below the vacuum level. The dark noise (grey) was 15.6 dB below the vacuum level and was averaged over 10 traces. The red and blue traces were measured by hand locking both LO phases simultaneously to the maximal possible noise level (anti-squeezing) and afterwards to the minimal possible noise level (squeezing). The oscillating signals were created by locking one LO phase to squeezing and afterwards to anti-squeezing while the other LO phase was periodically scanned. Settings for the measurement: sideband frequency = 5 MHz, RBW = 300 kHz, VBW = 300 Hz, sweep time = 150 ms and pump power in front of the squeezer = 25 mW. The setup for this measurement is shown in figure 4.10. Data evaluation done in Python with a script written by Malte Lautzas.

was coupled in the squeezing resonator.

The reported values were in good agreement with the reconstructed values from the squeezing measurement along the 8-port paths in section 4.4. However, the reconstructed squeeze values were a little bit higher and the calculated loss was lower than the entanglement measurement. A possible explanation could be a different visibility because of different mode matchings to the diagnostic mode cleaner. The entanglement measurement was done two months after the 8-port path characterization, so the alignment might be different. But typically the mode matchings were checked before a measurement and they should not differ much. An obvious difference

between the entanglement measurement and the squeezing measurements along the 8-port paths was the electronic device to add or subtract the BHD signals in figure 4.10. This device was self built from former group members. It looked pretty old and we did not have much information about it. Probably this device introduced some extra noise and destroyed the entanglement a little bit and this was the reason for the deviation between the reconstructed values in section 4.4 and the values in this chapter.

In conclusion, the squeezed-light source could be optimized and was characterized with different methods. An optical loss below 10 % was achieved, which was a good basis for the cat state measurements.

Chapter 5

Measurements with noise envelope phase lock

The results presented in the previous chapter 4 were measured while the local oscillator phases were stabilized by hand. For doing a short squeezing measurement, which was typically 300 ms, this procedure worked fine. But for the generation of Schrödinger kitten states a data acquisition over minutes or maybe even hours was necessary. It was not possible to hold the phases stable by hand for such time scales. Therefore, an automatic locking technique was needed. Typically locking methods like the Pound-Drever-Hall technique [50] need a strong coherent field. But for the Schrödinger kitten state generation, a single photon detector was part of the experiment, so strong coherent fields had to be avoided. An alternative idea to stabilize the phases of the local oscillators without a strong coherent field was given by Daniela Abdelkhalek and Axel Schönbeck [45, p.106-108]. They created a LabVIEW code, which controlled the local oscillator phase shifter in a way that the signal on the BHD had a maximal variance (anti-squeezing) or minimal variance (squeezing). Unfortunately, this LabVIEW program did only work for short time scales and it was not possible to improve it to be long term stable. Axel Schönbeck suggested another idea by using an envelope detector [55]. With such a detector, the variance of a BHD signal could be read out and an analog servo proportional-integral-derivative (PID) locking technique could be used to stabilize the phases to the maximal squeezed quadrature or maximal anti-squeezed quadrature. The experimental realization was done by Malte Lautzas in his master thesis [48]. In this chapter the noise envelope locking technique is explained and the measurements from chapter 4 are shown again with noise envelope stabilized phases.

5.1 Noise envelope locking technique

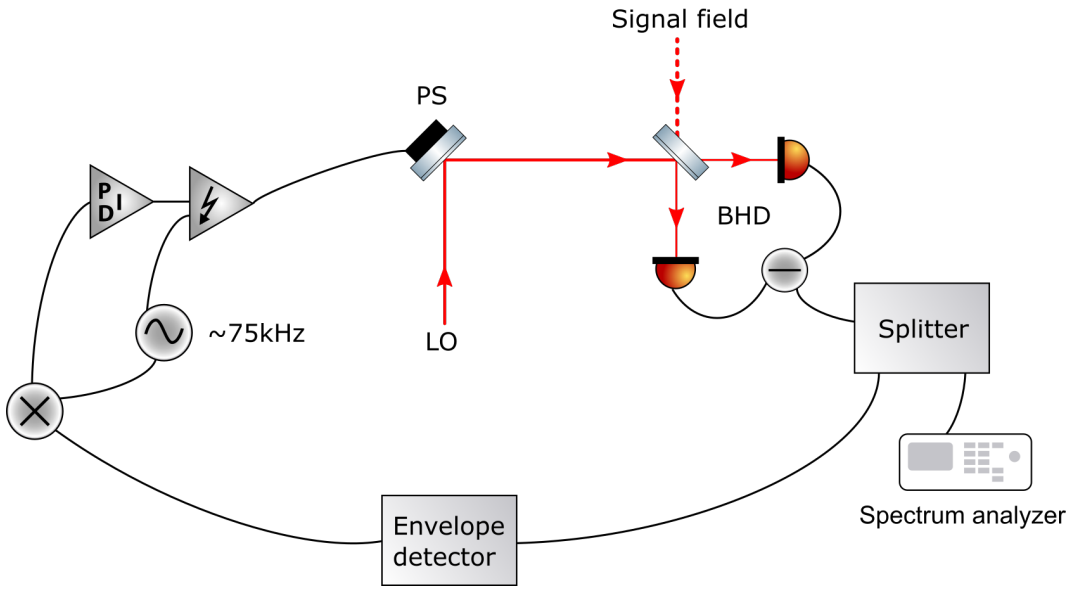

Figure 5.1: Noise envelope locking technique for phase stabilization. The phase of the local oscillator (LO) was stabilized to maximal noise (anti-squeezed quadrature) or minimal noise (squeezed quadrature). Therefore, the balanced homodyne detector (BHD) signal was sent into an envelope detector, which could read out the variance of the signal. The signal from the envelope detector was mixed with a frequency of 75 kHz, which was also sent over a high voltage amplifier to the phase shifter (PS). With this configuration an error signal was created in the mixer, which could be sent into a proportional-integral-derivative controller to stabilize the high voltage on the PS to a maximal or minimal noise level on the BHD. The BHD signal was split to be still available for measurements with a spectrum analyzer. Picture created with Inkscape.

Figure 5.1 shows the basic idea of the noise envelope locking technique. A phase modulation of 75 kHz was imprinted on the phase shifter, which controlled the measured quadrature in the balanced homodyne detector. The balanced homodyne detector signal was split with a signal splitter from "Mini-Circuits" to be available for the envelope detector and for a spectrum analyzer at the same time. The envelope detector read out the variance of the signal and sent it into a mixer together with the modulation frequency of 75 kHz. The output of the mixer was used as an error signal, which was sent into an analog PID controller to lock the phase shifter position via a high voltage on a piezoelectric element. The stabilization point depended on the phase relation between the modulation frequency on the phase shifter and the modulation frequency which was sent into the mixer. A phase flip by

180° could switch between a stabilization to the squeezed quadrature and anti-squeezed quadrature.

5.2 Noise envelope stabilized squeezing measurement with one balanced homodyne detector

For a conventional squeezing measurement with noise envelope lock the same preparations were necessary as are described in chapter 4.2. The measurement procedure was done analog to chapter 4.3. But now instead of stabilizing the LO phase by hand, the noise envelope locking technique from figure 5.1 was used. Figure 5.2 shows the result of a conventional squeezing measurement with noise envelope lock. The measured traces were normalized to the vacuum level. Hence the relative noise power in dB is shown and the vacuum trace is on 0 dB. For the squeezed quadrature a value of -9.7 dB could be reached while the anti-squeezed quadrature was at 20.7 dB. The dark noise clearance was 17.5 dB for a local oscillator power of 20 mW in front of the beam splitter from the balanced homodyne detector. When a dark noise correction was done by subtracting the dark noise from all other traces a dark noise corrected squeeze value of -10.5 dB and a dark noise corrected anti-squeeze value of 20.8 dB was evaluated. From the dark noise corrected values the optical loss could be calculated with equation 3.2 and lead to a value of 8.3 %. Additionally, with equation 3.3 the initial squeezing could be calculated to 21.2 dB. For this measurement a pump power of 26 mW in front of the squeezer was used. Because of a bad mode matching of the pump field to the squeezer only around 70 % of this power was coupled in the squeezing resonator.

For the hand locked conventional squeezing measurement in figure 4.6 a measured squeeze level of -10.6 dB could be reached and the calculated loss was 6.5 %. So, the results were better without the noise envelope locking technique. Between these measurements more then half a year passed. In principle differences in the mode matchings to the diagnostic mode cleaner could explain a loss difference, but the mode matchings were checked from time to time and they looked not so different to explain around 2 % higher loss. Another explanation might be some dust or dirt on the optics in the squeezing path. The experiment was placed in a clean room area, but this gave no absolute guarantee to avoid all kind of particles. Moreover, for the noise envelope stabilized measurement the signal of the BHD had to

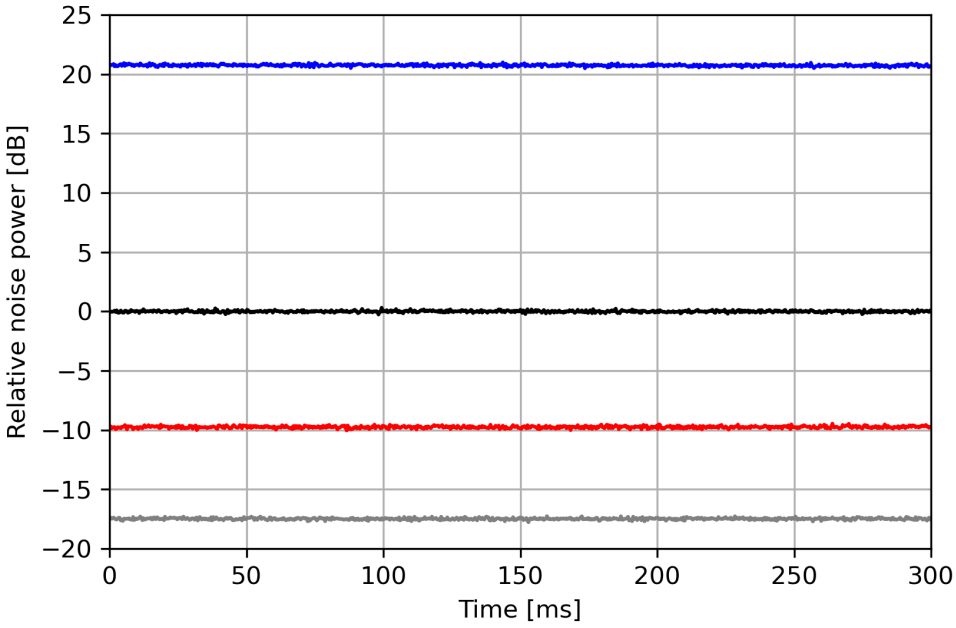

Figure 5.2: Result of the conventional squeezing measurement with noise envelope lock. The relative noise power in dB is plotted against the measurement time in ms. The anti-squeezed trace (blue) was 20.7 dB above the vacuum level (black). The squeezed trace (red) was 9.7 dB below the vacuum level. The dark noise (grey) was 17.5 dB below the vacuum level. Settings for the measurement: sideband frequency = 5 MHz, RBW = 300 kHz, VBW = 300 Hz, sweep time = 300 ms, average 10 traces and pump power in front of the squeezer = 26 mW. The setup for this measurement is shown in figure 4.1. Data evaluation done in Python with a script written by Malte Lautzas.

be split to be available for the noise envelope lock and the spectrum analyzer at the same time, as can be seen in figure 5.1. Therefore, a splitter from the company "Mini-Circuits" was used and this splitter seemed to introduce some extra noise, which reduced the amount of squeezing. But a hand locked squeezing measurement without using this splitter was done on the same day as the noise envelope stabilized conventional squeezing measurement was recorded and it showed -9.9 dB squeezing and 19.4 dB anti-squeezing. After dark noise correction, the squeeze level was -10.5 dB and the anti-squeeze level was 19.5 dB. The loss calculated from the dark noise corrected values was 7.9 %. So, the splitter alone could not explain the entire additional loss. For certain modulation frequencies the squeezing was also damaged, but it was always tried to choose a modulation frequency which made no problems. Nevertheless, a good working modulation frequency might still introduced some extra noise, which reduced the reachable

squeezing. The additional loss was probably caused by a combination of the discussed possibilities. But even when the reachable squeezing was lower, the setup had a clear advantage with the noise envelope lock: the local oscillator phases could be stabilized over longer time scales. This allowed the usage of the average function of the spectrum analyzer to get more precise results. For the noise envelope stabilized result in figure 5.2 the traces were averaged 10 times. It is clearly visible that the statistical error in figure 5.2 was smaller compared to the hand locked single traces in figure 4.6. To quantify the improvement the statistical error for the single hand locked squeezed trace was 0.17 % relative error while the relative error for the averaged noise envelope stabilized squeezed trace was 0.04 %. Errors were automatically calculated in the Python data evaluation script, written by Malte Lautzas, with help of the package "Uncertainties: a Python package for calculations with uncertainties" from Eric O. Lebigot.

5.3 Noise envelope stabilized squeezing measurements with two balanced homodyne detectors

The noise envelope stabilized squeezing measurement along the 8-port paths was done analog to chapter 4.4. But now both BHDs used the noise envelope locking technique from figure 5.1. For BHD1 the anti-squeezed trace was 16.2 dB and the squeezed trace was -2.4 dB. The dark noise clearance was 16.2 dB for a local oscillator power of 20 mW in front of the beam splitter from the balanced homodyne detector. For BHD2 the anti-squeezed trace was 17.5 dB and the squeezed trace was -2.5 dB. The dark noise clearance was 18.6 dB for a local oscillator power of 20 mW in front of the beam splitter from the balanced homodyne detector. Figure 5.3 shows the normalized results for both balanced homodyne detectors. Formula 3.24 and 3.25 allowed to calculate out the loss from the 50/50 8-port beam splitter. The reconstructed squeeze value without the 50 % beam splitter loss for BHD1 was -8.5 dB and the anti-squeeze value was 19.2 dB. When also a dark noise correction was applied to the data, the dark noise corrected reconstructed values were -9.2 dB for the squeezed quadrature and 19.3 dB for the anti-squeezed quadrature. From this values an optical loss of 11.1 % and an initial squeezing of 19.8 dB could be calculated with equations 3.2 and 3.3.

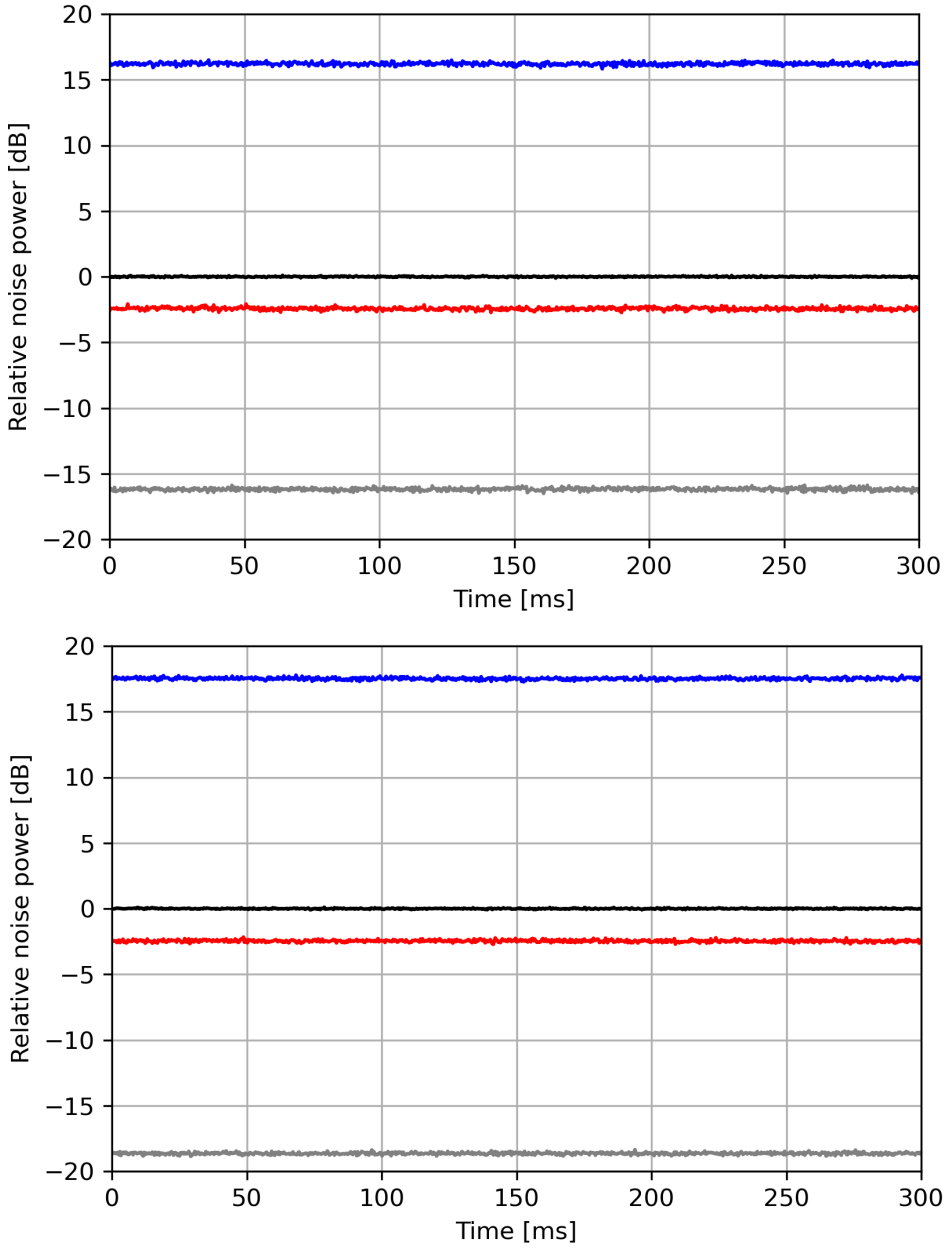

Figure 5.3: Results for a squeezing measurement along the 8-port paths with noise envelope lock for BHD1 (top) and BHD2 (bottom). The relative noise power in dB is plotted against the measurement time in ms. The anti-squeezed trace (blue) was 16.2 dB for BHD1 and 17.5 dB for BHD2 above the vacuum level (black). The squeezed trace (red) was 2.4 dB below the vacuum level for BHD1 and 2.5 dB for BHD2. The dark noise (grey) was 16.2 dB below the vacuum level for BHD1 and 18.6 dB for BHD2. Settings for the measurement: sideband frequency = 5 MHz, RBW = 300 kHz, VBW = 300 Hz, sweep time = 300 ms, average 10 traces and pump power in front of the squeezer = 25 mW. The setup for this measurement is shown in figure 4.8. Data evaluation done in Python with a script written by Malte Lautzas.

For BHD2 the reconstructed values were -8.7 dB squeezing and 20.5 dB anti-squeezing and the dark noise corrected reconstructed values were -9.1 dB squeezing and 20.5 dB anti-squeezing. From this values an optical loss of 11.6 % and an initial squeezing of 21.1 dB could be calculated with equations 3.2 and 3.3. The results of both BHDs were very similar. Reasons for a deviation were already discussed in chapter 4.4. For the noise envelope stabilized measurements in figure 5.3 the traces were averaged 10 times, which reduced the statistical error compared to the single trace hand locked measurements in figure 4.9. The squeeze level in the noise envelope stabilized measurement was lower and the calculated optical loss was higher than the hand locked measurements. Possible reasons for this deviation were already discussed in section 5.2.

5.4 Noise envelope stabilized entanglement measurement

The noise envelope stabilized entanglement measurement was done analog to chapter 4.5. But now both BHDs used the noise envelope locking technique from figure 5.1. Figure 5.4 shows the result of a v-class entanglement measurement with the noise envelope lock. The measured traces were normalized to the vacuum level. Hence, the relative noise power in dB is shown and the vacuum trace is on 0 dB. For the squeezed trace a value of -7.4 dB could be reached while the anti-squeezed trace was 16.7 dB. The dark noise clearance was 15.0 dB for local oscillator powers of 19 mW for BHD1 and 15 mW for BHD2, measured in front of the beam splitters of the balanced homodyne detectors. Different local oscillator powers were necessary to have the same absolute vacuum level, which was discussed in chapter 4.5. When a dark noise correction was done by subtracting the dark noise from all other traces a dark noise corrected squeeze value of -8.0 dB and a dark noise corrected anti-squeeze value of 16.8 dB could be evaluated. From the dark noise corrected values the optical loss could be calculated with equation 3.2 and lead to a value of 14.2 %. Additionally, with equation 3.3 the initial squeezing could be calculated to 17.5 dB. For this measurement a pump power of 26 mW in front of the squeezer was used. Because of a bad mode matching of the pump field to the squeezer only around 70 % of this power was coupled in the squeezing resonator. For the noise envelope stabilized entanglement measurement in figure 5.4 the traces were averaged 10 times, which

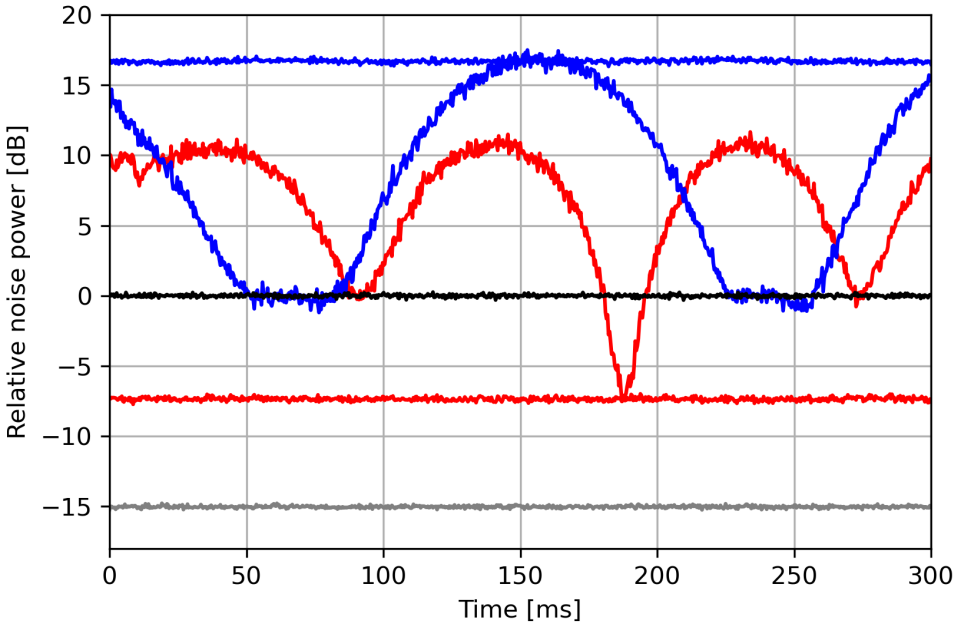

Figure 5.4: Result for a v-class entanglement measurement with noise envelope lock. The relative noise power in dB is plotted against the measurement time in ms. The anti-squeezed trace (blue) was 16.7 dB above the vacuum level (black). The squeezed trace (red) was 7.4 dB below the vacuum level. The dark noise (grey) was 15.0 dB below the vacuum level. The oscillating signals were created by locking one LO phase to squeezing or anti-squeezing while the other LO phase was periodically scanned. Settings for the measurement: sideband frequency = 5 MHz, RBW = 300 kHz, VBW = 300 Hz, sweep time = 300 ms, average 10 traces and pump power in front of the squeezer = 26 mW. The setup for this measurement is shown in figure 4.10. Data evaluation done in Python with a script written by Malte Lautzas.

reduced the statistical error compared to the single trace hand locked measurements in figure 4.11. The squeeze level in the noise envelope stabilized entanglement measurement was lower and the calculated optical loss was higher than the hand locked measurement. Possible reasons are the signal splitter, mode matchings and some dust on the optics as discussed in section 5.2. The noise envelope stabilized entanglement measurement resulted to lower squeeze level and higher loss values compared to the reconstructed squeeze values from the noise envelope stabilized squeezing measurement along the 8-port paths in section 5.3. This was probably caused by the electronic device to add or subtract the balanced homodyne detector signals in figure 4.10.

In conclusion, the squeezed-light source with noise envelope phase stabilization showed smaller squeeze and higher loss values compared to the

hand locked results in chapter 4, but the noise envelope phase stabilization allowed to measure over longer time scales, which was an essential requirement for the cat state measurements.

Chapter 6

Avalanche photo diode characterization

To create Schrödinger kitten states, a single photon subtraction from a squeezed state of light was applied (see chapter 3.2). To realize a single photon subtraction a single photon detector was used. The most common types are avalanche photo diodes (APD), which use an amplification of charge carrier to make the signal of a single photon visible. In chapter 3.3 the theoretical background about single photon detectors can be read. In this chapter the characterization of different APDs is shown. We had two silicon APDs in our group and we temporarily had an InGaAs APD. The results for the silicon APDs were accrued in the bachelor thesis from Julian Hörsch [56]. The investigation of the InGaAs APD was done together with Stephan Grebien and Malte Lautzas. This chapter begins with an introduction of the experimental setup and the procedure for a measurement of the quantum efficiency. The basic idea is to compare the signal strength from the APD with a reference power, which is sent to the APD. Afterwards the quantum efficiency results and other relevant parameters like dark counts and dead times are presented for all three APDs.

6.1 Experimental setup

Figure 6.1 shows the setup for a quantum efficiency measurement. For greater clarity not every used component is shown. The same laser as in chapter 4 was used, but for the quantum efficiency measurements only the laser beam with a wavelength of 1064 nm was needed. At the beginning, the laser beam was sent through a mode cleaner (MC). Details about the MC and its length stabilization with a Pound-Drever-Hall locking scheme were already given in chapter 4.2.1. To be able to control the power of the laser beam it was sent through a half-wave plate and a polarizing beam splitter (PBS). The light

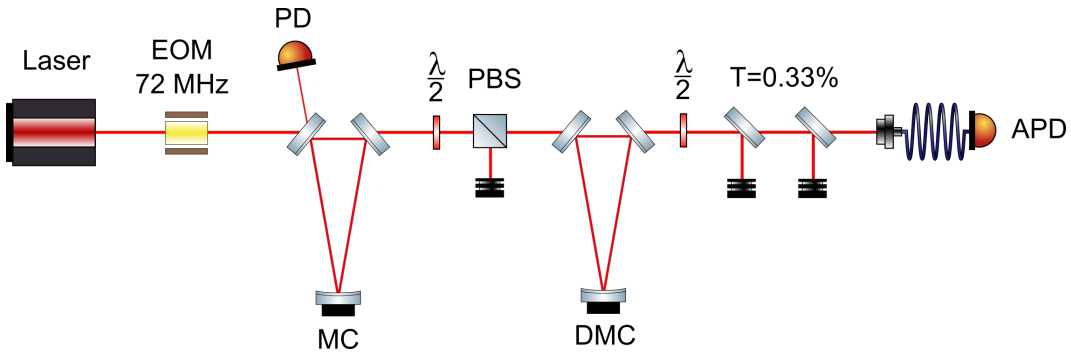

Figure 6.1: Simplified setup for a quantum efficiency measurement. The laser beam (1064 nm) was sent through an electro optical modulator (EOM) and passed a mode cleaner (MC), which was stabilized to resonance by a photo diode (PD) in reflection with the Pound-Drever-Hall technique. Afterwards the light passed a half-wave plate ($\frac{\lambda}{2}$) and a polarizing beam splitter (PBS), which allowed the control of the power. In transmission of the PBS the light was in p-polarization and was sent through a diagnostic mode cleaner (DMC). Then the polarization was turned to s-polarization with a ($\frac{\lambda}{2}$) plate. The beam was attenuated via transmission through two mirrors with T = 0.33 % for each mirror. Finally, the light was coupled into a fiber and was detected by an avalanche photo diode (APD). Picture created with Inkscape.

in transmission of the PBS was in p-polarization. The beam passed a diagnostic mode cleaner (DMC). Afterwards the polarization was turned to s-polarization with a half-wave plate. The laser beam was transmitted through two attenuation mirrors. This mirrors had each a transmission of 0.33 % for s-polarized light. Finally, the light was coupled into a fiber and could be detected by an APD.

6.2 Measurement procedure

The first step was to activate the Pound-Drever-Hall lock of the MC. Afterwards mode matchings to the DMC had to be done. On the one hand the beam from the MC had to be matched to the DMC, on the other hand a good mode matching from the DMC into the fiber coupler was necessary. To reach a good matching between DMC and fiber coupler a trick was used: some light was sent through the backside of the fiber. Figure 6.2 illustrates this reversed fiber mode matching technique. The mode from the fiber was matched to the DMC with two lenses and two mirrors. When this mode matching was good, the mode matching from the DMC to the fiber was also good. To perform a mode matching the length of the DMC was scanned by applying a periodic voltage to the integrated piezoelectric element. The

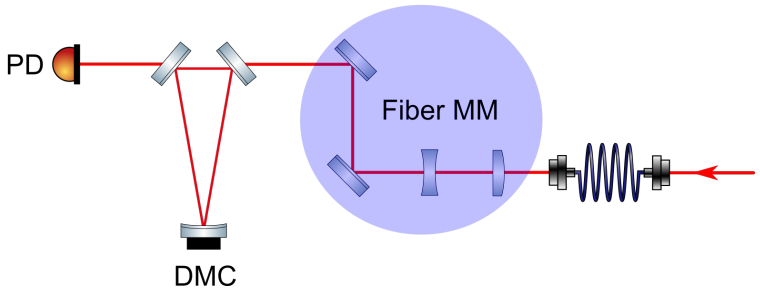

Figure 6.2: Reversed fiber mode matching technique. To get a good mode matching into the fiber a trick was used: some light was sent through the backside of the fiber. With two lenses and two mirrors the fiber mode matching (Fiber MM, blue area) could be performed by aligning the beam from the fiber to the length scanned diagnostic mode cleaner (DMC). The modes were monitored with a photo diode (PD) in transmission of the DMC. When the mode from the fiber was matched to the DMC, the mode from the DMC was also matched to the fiber. Picture created with Inkscape.

photo diode signal in transmission of the DMC was read out with an oscilloscope. The mode matching between fiber and DMC was around 91 %. The mode matching from MC to DMC was around 98 %.

The power of the laser beam in front of the DMC was set to a value in the range of $0.2\,\mu W - 20\,\mu W$. To control the power the half-wave plate in front of the PBS was used. To measure the power a power meter was used (Ophir Nova II). As discussed in chapter 4.1 this power meter had a large estimated relative error of $\pm 10\,\%$. Hence, no high precision measurements of the quantum efficiency were possible, however, that was not a problem because the goal of the APD characterizations in this chapter was to get a rough estimation about the quantum efficiency magnitude. The power which reached the APD had to be much smaller. The typical order which can be handled by an APD is a power in the pico watt range. It was impossible to set such small powers with the power meter, so the power range of $0.2\,\mu W - 20\,\mu W$ was chosen and with the attenuation mirrors it was reduced to 11 ppm of the adjusted intensity, which brought the power to the correct order for an APD. The non perfect mode matchings to the DMC and optical loss on every optical component could further reduce the power, but for a rough estimation of the quantum efficiency this was neglected.

The APD signal was read out with an oscilloscope (Keysight InfiniVision DSOX3024T). The impedance on the oscilloscope channel should be set to 50 Ohm [41, p.2]. Triggering to the oscilloscope channel was activated with the trigger mode “edge than edge”. The mode coupling option was set to “normal”. After pressing the time-axis button, the APD pulse was visible in

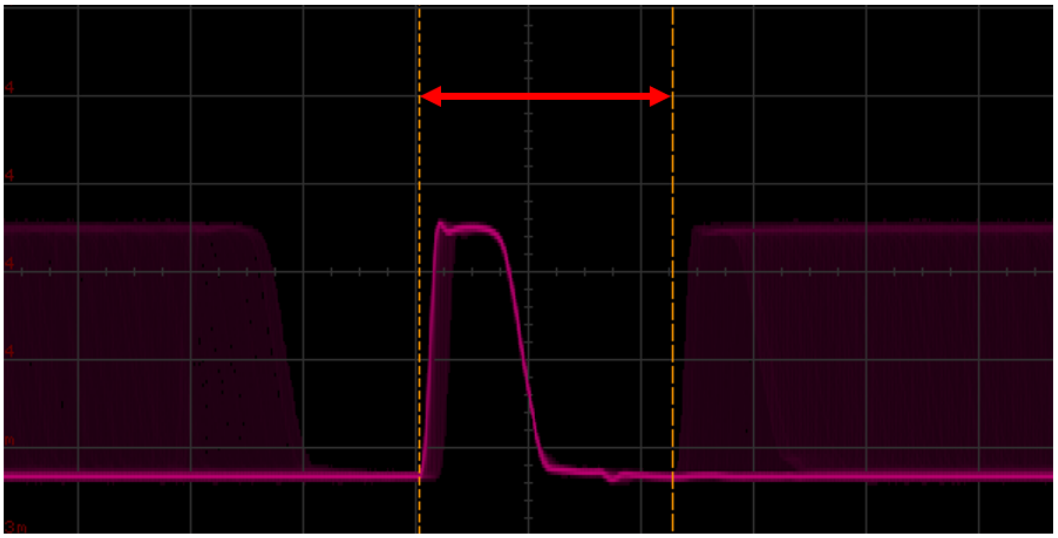

Figure 6.3: APD dead time measurement principle. The dead time of an APD could be estimated on the oscilloscope. Therefore, the time interval between the beginning of the triggered pulse and the next possible pulse was measured (red arrow). The vertical measurement cursors (yellow dashed lines) were used to read out this time interval on the oscilloscope monitor. Picture saved with Keysight InfiniVision DSOX3024T.

the center of the oscilloscope. An example screenshot from the oscilloscope is shown in figure 6.3. The oscilloscope was able to perform a counter measurement for the used channel, which counted the pulses per second.

For the quantum efficiency measurement, the maximal count rate was read out with the oscilloscope by manually turning the DMC to resonance by using a potentiometer, which controlled the voltage on the piezoelectric element in the DMC. It was also possible to measure the dead time with the oscilloscope by using the measurement cursors and determine the time interval where no pulse appeared. An illustration about the dead time measurement is shown in figure 6.3. The dark count rate of the APD was also measured. Therefore, the fiber was disconnected from the APD and a protection cap was placed on the fiber coupler. Hence absolutely no light could reach the detector and the intrinsic dark count rate of the APD could be observed on the oscilloscope. Finally, the quantum efficiency could be calculated with equation 3.9.

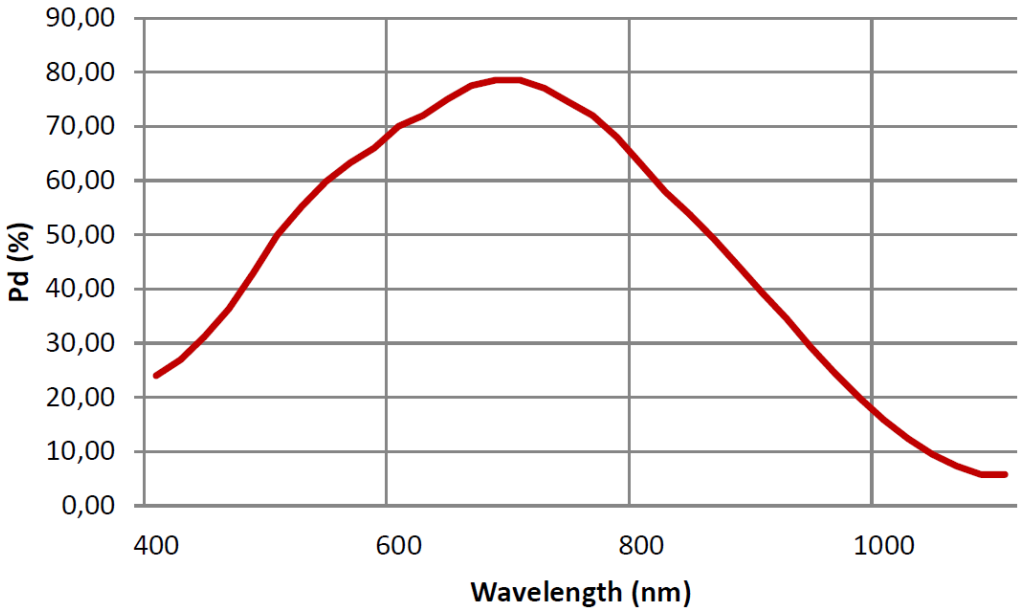

Figure 6.4: Quantum efficiency for the COUNT NIR silicon avalanche photo diode. The photon detection efficiency Pd in % is plotted against the wavelength in nm. For 1064 nm the photon detection efficiency is around 5 % – 7 %. Picture taken from data sheet [41, p.5].

6.3 Characterization of the first detector

The first detector characterized was a silicon APD from "Laser Components". It is part of the series COUNT NIR and has the model number COUNT 50N-FC. The 50 stands for a dark count rate of 50 counts per second and the FC predicates that the APD is fiber coupled. The dead time should be 45 ns. These and more information about the detector can be found in the data sheet [41]. The measured dark count rate was around 35 counts per second and the measured dead time was 45 ns. The measured values are in good agreement with the data sheet values, but for the quantum efficiency a large deviation between data sheet and measurement can be observed. Figure 6.4 shows the quantum efficiency of the COUNT NIR in dependence of the wavelength, which is given in the data sheet [41, p.5]. For 1064 nm a value between 5 % and 7 % can be estimated. The measured value was only around 1 %. A possible explanation for such small quantum efficiency could be that the COUNT NIR is only specified for the wavelength range from 400 nm to 1000 nm [41, p.1-2]. So, the used wavelength of 1064 nm was far away from the specified area. This might gave additional losses, for example, through the fiber coupler, which contained a lens that was optimized and coated for the range from 440 nm to 1000 nm [41, p.3]. Of course, another possible explanation

might be a systematic error in the experimental setup. To investigate if the experimental setup worked correctly, another APD was characterized, as it is shown in the following section.

6.4 Characterization of the second detector

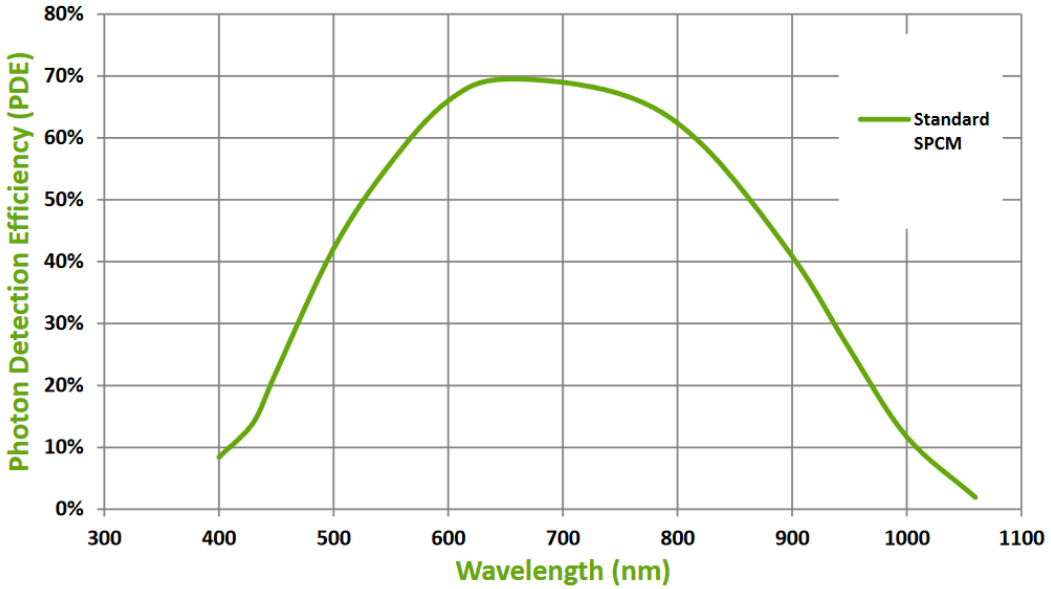

Figure 6.5: Quantum efficiency for the AQRH silicon avalanche photo diode. The photon detection efficiency PDE is plotted against the wavelength in nm. For 1064 nm the photon detection efficiency is around 1 % – 2 %. Picture taken from data sheet [57, p.7].

Another silicon APD from "Perkin Elmer" (now called "Excelitas Technologies") was available in our group, which was used in former experiments by Christoph Baune [33]. The model number is SPCM-AQRH-13-FC. The 13 has no physical meaning, it is just a consecutive type number and the FC predicates again that the APD is fiber coupled. The dark count rate should be 250 counts per second and the dead time should be 22 ns. These and more information about the detector can be found in the data sheet [57]. The measured dark count rate was around 260 counts per second and the measured dead time was 28 ns. The measured dark count rate is in good agreement with the data sheet value. The measured dead time is a little bit higher than the data sheet value, but this should not be a problem because the value is still smaller than the dead time from the COUNT NIR. Figure 6.5 shows the quantum efficiency of the AQRH in dependence of the wavelength, which is given in the data sheet [57, p.7]. For 1064 nm a value between 1 % and

2 % can be estimated. The measured value was around 1 %. For the AQRH, which is specified for a wavelength range from 400 nm to 1060 nm, the measured value is close to the expected value. For this detector the operating wavelength of 1064 nm is only 4 nm outside the specification, which probably does not contribute much extra loss. Therefore, this measurement can be seen as a confirmation that the experimental setup worked in principle. The most probable reason for the COUNT NIR deviation between data sheet and measurement is indeed the usage 64 nm outside its specification.

6.5 Characterization of the third detector

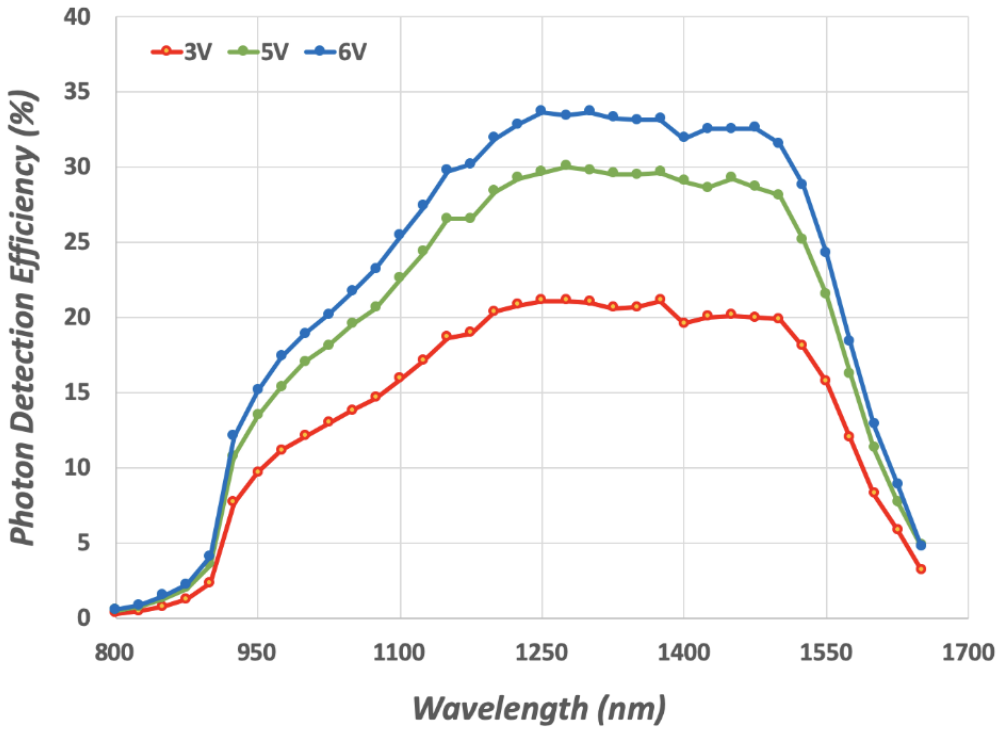

Figure 6.6: Quantum efficiency for the PDM IR InGaAs avalanche photo diode. The photon detection efficiency in % is plotted against the wavelength in nm. For 1064 nm the photon detection efficiency is around 13 % for 3 V, around 18 % for 5 V and around 20 % for 6 V. Picture taken from data sheet [58, p.1].

To get a higher quantum efficiency for 1064 nm, an InGaAs APD was bought from "MPD", which was called "PDM IR" and also had a fiber coupled input. In contrast to our silicon APDs, the PDM IR had a USB connection, which allowed the use of specialized computer software to adjust several parameters. For example, the dead time could be set to a value between

1 μs and 3000 μs, the operating temperature could be set to 4 different values between 225 K and 243 K and different bias voltages could be chosen. The quantum efficiency depends on the bias voltage and is shown in figure 6.6 for 3 V, 5 V and 6 V. The dark count rate also depends on the parameters used and should be maximal 1000 counts per second for 2 V. These and more information about the detector can be found in the data sheet [58]. Figure 6.6 shows a quantum efficiency for 1064 nm of around 13 % for 3 V, around 18 % for 5 V and around 20 % for 6 V, but with our setup we could only measure around 3 % for 3 V and around 5 % for 5 V. The 6 V setting was not investigated. The measurements were done for different temperature settings (229 K, 233 K and 243 K) and different dead times (10 μs, 20 μs, 30 μs and 40 μs). The dead time had to be high enough to suppress after pulsing. A marker for having after pulsing was a much higher dark count rate as expected. In this case the dead time was increased until the dark count rate dropped to a reasonable value. Which dead time was needed depended on the other selectable parameters. The company was contacted because of the low quantum efficiency results. Thereafter they also did a quantum efficiency measurement and confirmed that the quantum efficiency around 1064 nm is really much smaller as shown in the data sheet [58, p.1]. They gave us the possibility to refund the detector and we agreed. Therefore, this detector is not available for further measurements, but at least we got another confirmation that the results presented in this chapter are valid.

For the cat state measurements in the following chapter, the COUNT NIR was used because it has a much lower dark count rate compared to the AQRH while the quantum efficiency of both silicon APDs is in the same order of around 1 %. Therefore, the signal to noise ratio is better for the COUNT NIR, which gives better cat states than the AQRH would give.

Chapter 7

8-Port measurements of Schrödinger kitten states

So far either continuous homodyne detection was used (chapter 4 and chapter 5) or a discrete single photon detection was used (chapter 6). For this chapter both techniques were combined to generate Schrödinger kitten states. The characterization was done with an 8-port homodyne detector. The theoretical background about the generation of Schrödinger kitten states and 8-port homodyne detection is given in chapter 3.2 and chapter 3.4.2. At the beginning of this chapter the experimental setup is shown and explained. Afterwards the measurement procedure and the data evaluation are presented. By exchanging the single photon detector strong improvements could be achieved. Finally, the result of a post processing of the measured data is reported, where the amplitude of the Schrödinger kitten state was increased. The measurement and evaluation of Schrödinger kitten states were part of the master theses from Stephan Grebien and Felix Pein [40][59]. The realization of this experiment was strongly inspired by the doctor theses from Christoph Baune and Jonas Schou Neergaard-Nielsen [33][39]. The post processing was done by Jaromír Fiurásek from the Palacký University Olomouc.

7.1 Experimental setup

Figure 7.1 shows the setup for a Schrödinger kitten state measurement. For greater clarity not every used component is shown. The setup for the squeezing generation and the 8-port homodyne detection was the same as described in chapter 4. For the Schrödinger kitten state generation, a single photon was subtracted from the squeezed field. Therefore, a small amount of the squeezed field was tapped off. This was done by using a half-wave plate and a polarizing beam splitter to be able to control the splitting ratio. Typically values between 1 % and 10 % were tapped off. The tapped off signal

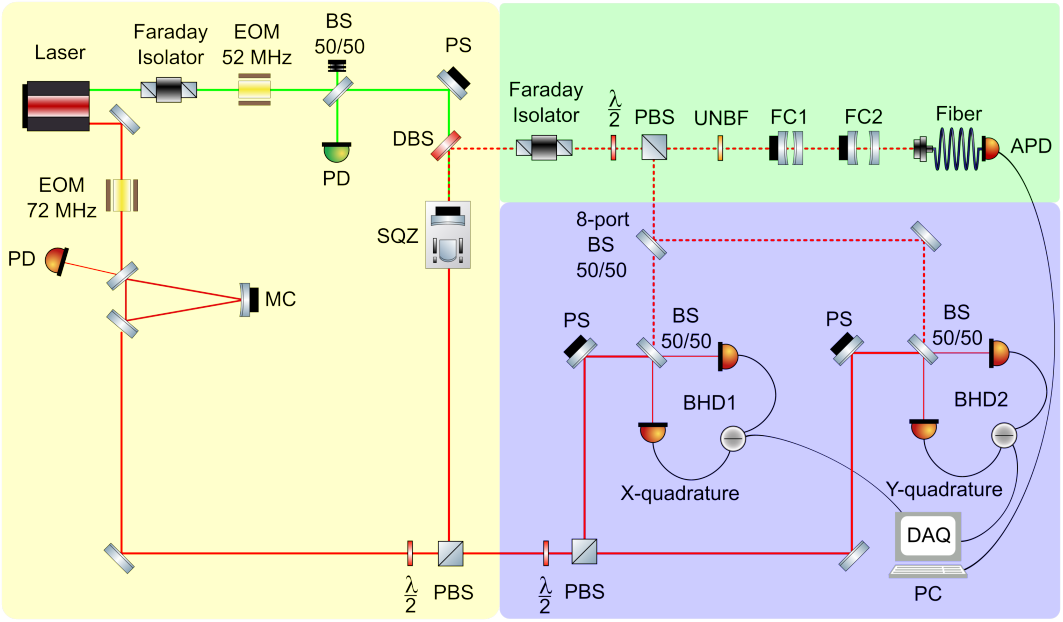

Figure 7.1: Simplified setup for an 8-port cat state measurement. The squeezing generation (yellow) and 8-port homodyne detection (blue) is the same as in figure 4.8. The green area is new and was needed to subtract a single photon from the squeezed field. First the squeezed field passed a Faraday isolator, which filtered out back scattered light from the homodyne detectors. Then a half-wave plate ($\frac{\lambda}{2}$) and polarizing beam splitter (PBS) was used to tap off a small part of the signal towards the fiber coupled avalanche photo diode (APD). An ultra narrow bandpass filter (UNBF) and two filter cavities (FC) were in front of the APD to be sure that only light reached the APD which was also detectable from the homodyne detectors. The data acquisition (DAQ) of the orthogonal phase locked homodyne detector signals was done with a computer (PC) and was triggered by the APD signal. Picture created with Inkscape.

was sent through an ultra narrow bandpass filter (UNBF) with a transmission of 85 %. Afterwards it passed two filter cavities (FC) and was coupled in a fiber, which was connected to an avalanche photo diode (APD). As APD the Laser Components module COUNT NIR was used, which was characterized in chapter 6.3.

Filter cavities were needed because the used APD had a broadband detection range over a wavelength interval of several hundred nanometer, as can be seen in figure 6.4, but the used homodyne detectors had only a bandwidth of a few hundred MHz as displayed in figure 7.2. The APD should only trigger the data acquisition for modes which could be seen from the homodyne detectors. But the squeezing resonator had a free spectral range (FSR) of 4.6 GHz. Hence, it could create also squeezed modes, which were not detectable by the homodyne detectors. To filter out these modes in front of the APD, two filter cavities were used with a FSR of 56.8 GHz for FC1 and

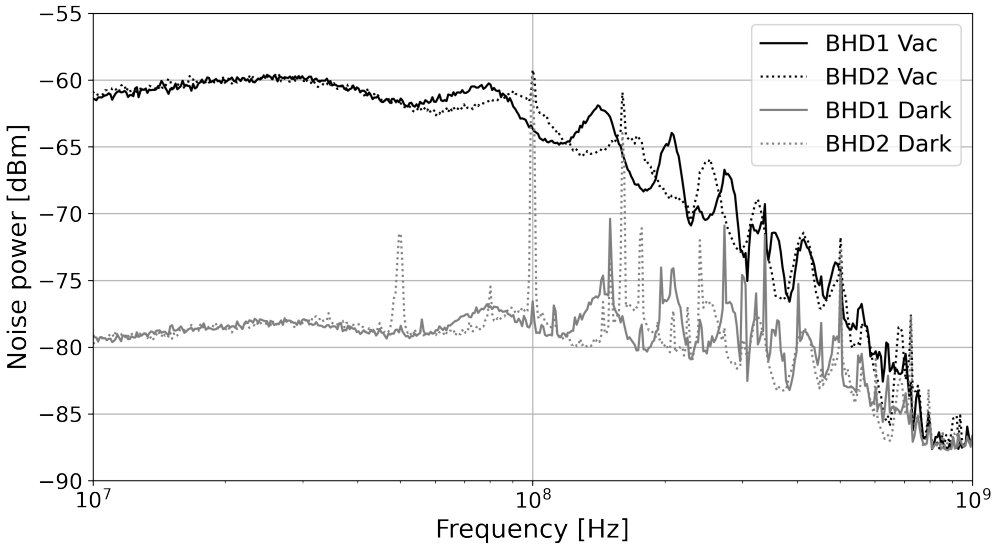

Figure 7.2: Balanced homodyne detector (BHD) bandwidth characterization. The noise power in dBm was plotted against the frequency in Hz. For both BHDs the vacuum noise (black) and the dark noise (grey) were measured. Up to a few hundred MHz a significant distance between dark noise and vacuum noise was visible. For higher frequencies the vacuum noise converged to the dark noise level and the BHDs got blind. Settings for the measurement: RBW = 1 MHz, VBW = 1 kHz, sweep time = 2 s and the local oscillator was around 18 mW in front of the 50/50 beam splitter. Data plot done in Python with a script written by Felix Pein.

47.8 GHz for FC2. But these two filter cavities had a common multiple with a GHz squeezing mode and still unwanted photons could reach the APD. Therefore, an ultra narrow band pass filter with a FWHM of 0.64 nm was also used. Figure 7.3 shows the principle of the filter cavities. The mechanical filter cavity design was taken from Axel Schönbeck [60, p.50-51]. The software "Finesse" was used to find suitable mirrors. For both mirrors in both cavities a radius of curvature of 25 mm and a reflectivity of 99 % were chosen. The corresponding finesse is 313. The quotient from FSR to finesse gives the linewdith (FWHM), which is 181 MHz for FC1 and 153 MHz for FC2. The linewidth of the squeezing resonator was a little bit smaller. It was characterized a long time ago as FWHM = 110 MHz [45, p.102][46, p.31].

Also a Faraday isolator, with a transmission of 97 %, was placed in the squeezing path. Without this Faraday isolator a lot of clicks from the local oscillators appeared on the APD and made the kitten state measurements impossible. Figure 7.4 illustrates what happens without Faraday isolator.

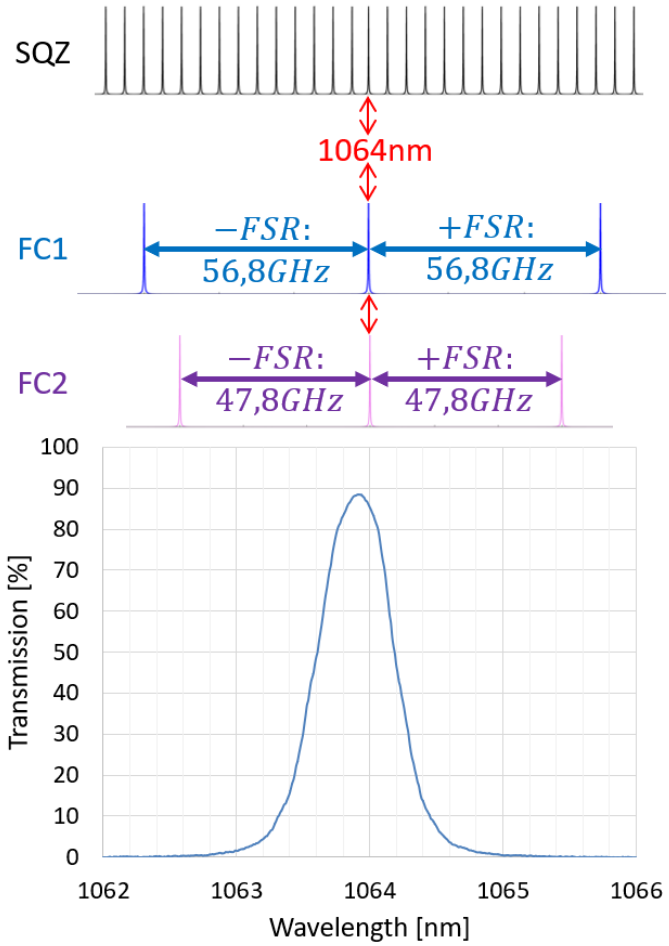

Figure 7.3: Filter cavity principle. On the top area of the picture the principle idea of the filter cavities is shown. The squeezing resonator (SQZ) created not only squeezing inside the linewidth around 1064 nm, but also at several other wavelengths, which fulfilled the resonance condition of the squeezing resonator (FSR = 4.6 GHz). All these GHz modes were filtered out. Therefore, two filter cavities (FC) were used with a FSR of 56.8 GHz for FC1 and 47.8 GHz for FC2. At a certain point out of the picture both filter cavities had a common multiple with a GHz squeezing mode. To filter out this case, an ultra narrow band pass filter with a FWHM of 0.64 nm was used (bottom picture). Top picture created with Finesse and Microsoft Power Point. Bottom picture taken from manufacturer's test report.

A small amount of the local oscillator powers seem to be scattered into the signal modes. This light passed the 8-port beam splitter and was reflected from the polarizing beam splitter (PBS) into the squeezer (SQZ). Then the back scattered light was reflected from the SQZ and copropagated to the signal field. Some power of the back scattered light was transmitted by the PBS and passed the two filter cavities (FC) and coupled into the fiber to the avalance photo diode (APD). Placing the Faraday isolator, at the position shown in figure 7.1, solved this problem.

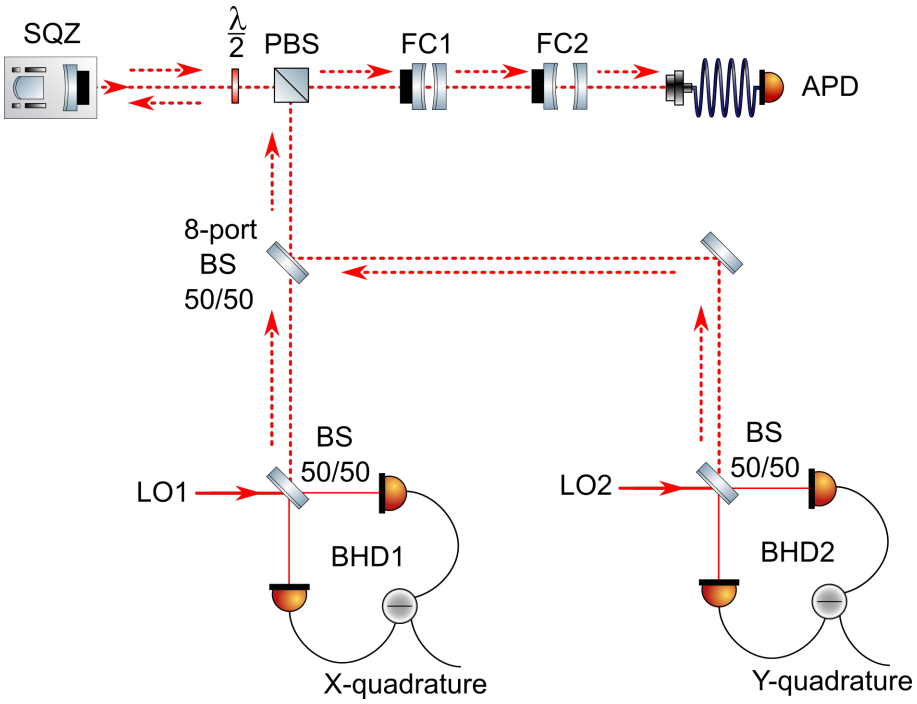

Figure 7.4: Situation without Faraday isolator. Some power from the local oscillators (LO) was scattered back from the balanced homodyne detectors (BHD). The 8-port beam splitter (BS) was passed and the back scattered light was reflected from the polarizing beam splitter (PBS) into the squeezer (SQZ). Then the back scattered light was reflected from the SQZ and copropagated to the signal field. Some power of the back scattered light was transmitted by the PBS and passed the two filter cavities (FC) and coupled into the fiber to the avalance photo diode (APD). On the APD a lot of clicks were visible, which came from the back scattered light. To filter out the back scattered light a Faraday isolator had to be placed between the SQZ and the PBS. Picture created with Inkscape.

7.2 Measurement procedure

For a Schrödinger kitten state measurement the same preparations as for squeezing measurements were necessary like activating the Pound-Drever-Hall locks, set the correct squeezing-crystal temperature and doing the mode matchings for the balanced homodyne detectors. Detailed explanations about this steps were already given in chapter 4.2. Additionally, the single photon subtraction path had to be prepared. From time to time the mode matchings to the filter cavities and to the fiber coupler were checked. But these mode matchings were quite stable and it was not necessary to do it before every measurement. Typical mode matching values which could be reached were around 90 % to the first filter cavity and around 99 % to the second filter cavity. The mode matching to the fiber coupler was around 92 %. For this fiber

mode matching the same trick as in chapter 6.2 was used: some light was sent through the backside of the fiber, which was matched to the second filter cavity. To be able to observe the mode matchings several flip mirrors and photo diodes were placed in the single photon subtraction path, which are not shown in figure 7.1.

The filter cavities needed the correct length to be on resonance for the 1064 nm mode, which was detected from the balanced homodyne detectors. To find the correct length of the filter cavities, the control field was used, which was sent through the backside of the squeezing resonator. The filter cavites were set to the correct length by manually tuning the voltage of the integrated piezoelectric elements until the control field was fully transmitted by both filter cavities. The control field came from the same laser as the local oscillator. Therefore, the control field represented exactly the mode which should be transmitted by the filter cavities. The control field could only be used for finding the correct length while the APD was blocked, because the intensity of the control field would destroy the APD. When the filter cavities had the correct length, the control field had to be blocked. Afterwards the APD could be unblocked. The filter cavities could be hold on resonance without control field by using the APD signal. Therefore, the APD signal was sent into an oscilloscope to monitor the click rate. When the click rate got smaller the filter cavity lengths were fine tuned by changing the voltage to the piezoelectric elements manually until the click rate reached the maximum value. The APD signal was also necessary as trigger for the 8-port balanced homodyne detection, which was recorded with a data acquisition card. Hence, the APD signal was split with a signal splitter (self built device from former group members), to be available for the oscilloscope monitoring and data acquisition card at the same time.

The maximal click rate on the APD depended on several parameters like tap off to the APD, optical loss and the adjusted initial squeezing. Furthermore, room light and stray light could create additional clicks. In addition, the APD had an intrinsic dark count rate of around 35 clicks per second, measured in chapter 6.3. For the Schrödinger kitten state measurement, the tap off was set to 10 % and an initial squeezing around 3 dB was taken, measured at a sideband frequency of 5 MHz with a resolution bandwidth of 300 kHz. Of course, the initial squeezing over the whole spectrum from figure 7.5 was accordingly smaller. The corresponding pump power was around 5 mW. The click rate on the APD for this configuration was around 12.000 clicks per second. The optical table was covered with a black plastic foil to avoid room

light clicks. The effective dark count rate was around 150 clicks per second. It was a little bit higher than the intrinsic dark count rate of 35 clicks per second. Possible explanations were additional clicks from stray light of the laser beams or other light sources on the optical table like control lamps on the photo diodes or the plastic foil did not cover the table completely.

The last step before the Schrödinger kitten state measurements could be started was the installation of the data acquisition system. The measurements was done with a data acquisition card from Teledyne SP Devices: ADQ32 with a sampling rate of 2.5 GSPS and 12 bit vertical resolution [61]. It contained two input channels and a trigger channel. The APD signal was sent into the trigger channel and the two balanced homodyne detector signals were connected to the input channels. Figure 7.5 shows the squeezing spectra measured along the 8-port paths, which were used for the data acquisition. The squeezing spectra were captured for a cat state measurement configuration, which was typically a local oscillator power around 18 mW, pump power around 5 mW and the tap off was a few percent. The visible amount of squeezing was quite small because of the 50 % loss from the signal splitting in combination with a low initial squeezing. Some sharp peaks and oscillations at high frequencies were visible. The sharp peaks were caused by electronic pick up, for example, from devices in the lab like signal generators for the Pound-Drever-Hall locks. The oscillations were introduced by signal splitting electronics, which belonged to the homodyne detectors.

The balanced homodyne detector signals were also needed for the noise envelope phase locks, which were introduced in chapter 5. Therefore, signal splitters were used, which divided the BHD signals into three parts. So, the BHD signals could be sent into the data acquisition card and into the envelope detectors at the same time. The third output of the signal splitters was sent into spectrum analyzers to monitor the phase locks. For the 8-port balanced homodyne detection, the phase of BHD1 was stabilized to the maximal anti-squeezed quadrature and the phase of BHD2 was stabilized to the maximal squeezed quadrature. The theoretical background about 8-port balanced homodyne detection is presented in chapter 3.4.2.

When everything was locked the data acquisition could begin. Therefore, a control software in the programming language "C" was created by Stephan Grebien, which was based on an application programming interface received from the manufacturer. Some settings could be adjusted by the experimentalist like how many samples were acquired and which delay from the trigger was considered.

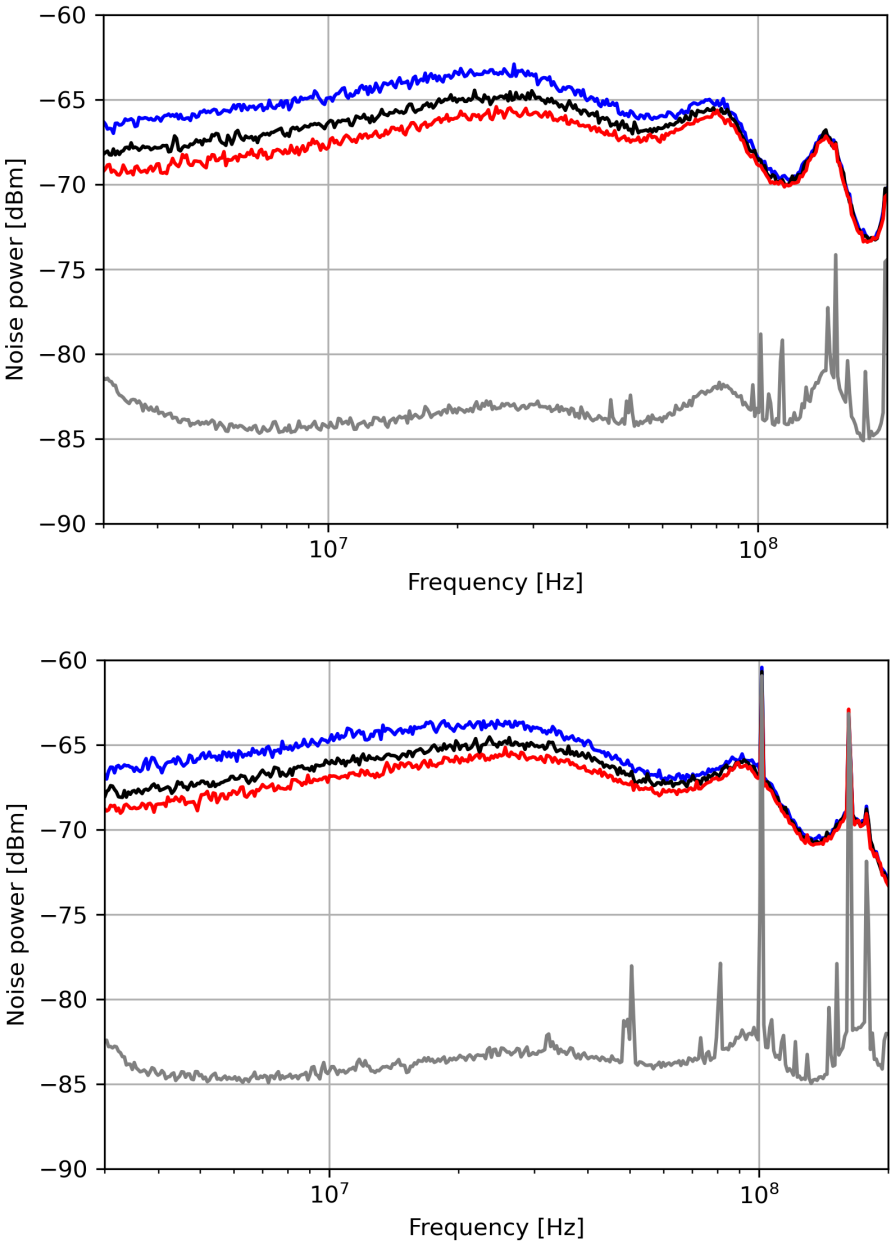

Figure 7.5: Squeezing spectra along the 8-port paths for BHD1 (top) and BHD2 (bottom). The noise power in dBm is plotted against the frequency in Hz. The anti-squeezed trace (blue), vacuum level (black), squeezed trace (red) and dark noise (grey) are shown. Both BHDs looked similar. The sharp peaks were caused by electronic pick up. The oscillations were introduced by signal splitting electronics. The phase of the local oscillator was stabilized with the noise envelope phase lock. Settings for the measurement: RBW = 300 kHz, VBW = 300 Hz, sweep time = 1.8 s and pump power in front of the squeezer = 5 mW. The setup for this measurement is shown in figure 4.8. Data plot done in Python with a script written by Felix Pein.

The amount of samples defined the size of the measurement window around a trigger event. The delay was required to compensate different optical lengths, cable lengths and response times between APD and BHDs. To identify the necessary delay and amount of samples, some test measurements were done. Therefore, different settings were tried out until an interesting area was visible in the recorded time window. What interesting means is shown in the next section.

7.3 Data evaluation

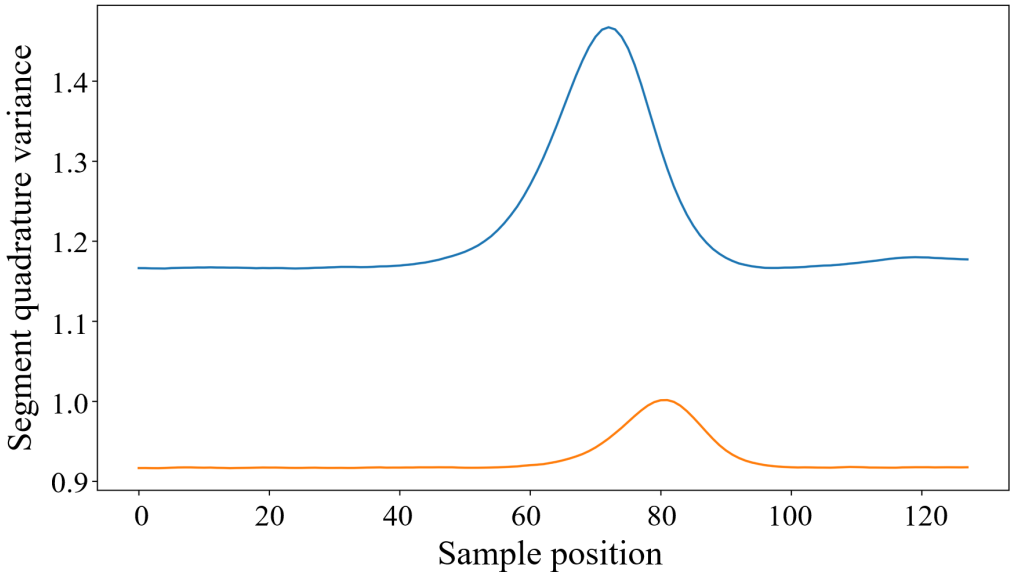

Figure 7.6: Schrödinger kitten state localization. The segment quadrature variance is plotted against the sample position. The whole measurement window contained 128 samples, which corresponded to 51.2 ns. Most of the time the segment quadrature variance was on a constant level, which represented the anti-squeeze value (blue) and the squeeze value (orange). But for a certain time interval the segment quadrature variance strongly increased. This was the interesting area where the kitten state was located. Slightly different sample positions of the interesting area in the squeezed and anti-squeezed quadrature could be explained by different cable lengths from the homodyne detectors to the data acquisition card. Plot created with a Python script written by Stephan Grebien.

The data evaluation was done analog to [33, p.71-73][39, p.95-99]. Each click on the APD activated the data acquisition and a certain time window was saved on the computer. For the APD measurement 128 samples were used. That corresponded to 51.2 ns. But only a small part of this time window represented the kitten state. To localize the kitten state inside the recorded

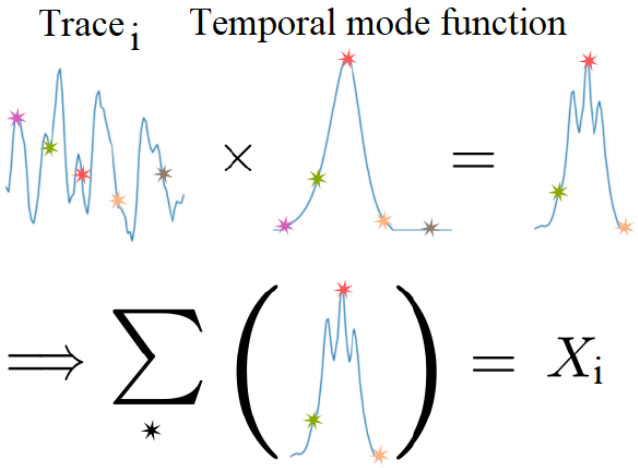

Figure 7.7: Quadrature extraction principle. Each measured trace was pointwise multiplied with the temporal mode function. Afterwards the sum over all resulting points was taken, which leaded to one quadrature value for each trace. Also vacuum traces were multiplied with the temporal mode function. In this case, the sum over all resulting points leaded to vacuum quadrature values, which can be used for a normalization. Exactly the same procedure was applied to the second homodyne detector to get the corresponding orthogonal quadratures. The shown data points are only some example points and did not represent the temporal resolution of the data acquisition card. Picture taken from [40, p.40].

traces a certain property of odd kitten states was used: an odd kitten state has larger quadrature variances compared to a squeezed state as can be seen in figure 2.7. Therefore, the relevant sample positions could be identified by calculating the variance at each sample position over all recorded traces. The result is called segment quadrature variance and can be seen in figure 7.6. Most of the time the segment quadrature variances were constant and represented the anti-squeeze and squeeze values. For a certain time interval, the segment quadrature variance strongly increased. This was the interesting area where the kitten state was located. Slightly different sample positions of the interesting area in the squeezed and anti-squeezed quadrature could be explained by different cable lengths from the homodyne detectors to the data acquisition card.

The segment quadrature variance from figure 7.6 could be used to estimate a temporal mode function, which was needed for the further evaluation. Therefore, the interesting area of the segment noise was cut out and normalized to unity. The square root was applied to achieve the temporal mode function. It allowed to extract one single quadrature value from each recorded trace. Therefore, the temporal mode function was multiplied

pointwise with the acquired traces and the outcome was summed up. Figure 7.7 illustrates the extraction of the X quadratures from one homodyne detector signal. The corresponding Y quadratures were received from the second homodyne detector signal with the same method. Typically several million clicks were used to start the data acquisition. Hence, several million quadrature pairs (X,Y) could be extracted. The probability distribution over all these quadrature values represents the Q-function, as can be seen in equation 3.21. For the measurements shown in this thesis, a vacuum normalization to 1 was used. Therefore, 10 million vacuum traces were recorded with each homodyne detector, which were also transformed to quadrature values as shown in figure 7.7. For the normalization, the difference between signal quadrature and mean value of the vacuum quadratures was divided by the standard deviation of the vacuum quadratures.

The first kitten state measurement evaluations as histogram were done with a Python script written by Stephan Grebien during his master thesis [59, p.47-48]. Later Jaromír Fiurásek joined the team and shared a MATLAB script for the data evaluation, which had even more features. For example, it could give out the density matrix of the measured state by using a maximum likelihood estimation [62]. The resulting density matrices for the kitten state measurements presented in this thesis are shown in appendix A.1. Furthermore the MATLAB script contained the post processing procedure to grow up the kitten states, which is discussed in section 7.5. Felix Pein wrote a Python script to plot the received density matrix as Q-function, Wigner function and photon statistics [40, p.62-65]. Following equations were used for that: 2.18, 2.19, 2.48 and 2.49.

Figure 7.8 left side shows the measurement result with an APD, where 10 million clicks were taken to activate the data acquisition. The Q-function looked similar to the simulated odd Schrödinger kitten state with $\alpha = 1$ and 25 % loss from figure 3.5. The Wigner function had a negativity, which is a sign of the nonclassicality of the state. The negativity was at the origin, which is a characteristic property of an odd cat state as can be seen in the simulated odd cat in figure 2.5. The photon statistics had dominantly contributions at odd photon numbers. While a pure odd cat state only has odd photon numbers, as can be seen in figure 2.5, the measured state also had a non vanishing contribution of even photon numbers, which was caused due to the optical loss. Another point which is noticeable is a certain asymmetry in the intensity distributions. In addition, a slightly rotation angle in the histogram is visible in figure 7.9 top left. Investigations about possible reasons

for asymmetry and rotation were done when a better single photon detector was available, which is the topic of the next section.

7.4 Exchange of the single photon detector

With the APD it was already possible to measure a state which was similar to an odd cat state. Because of the low quantum efficiency of around 1 % (see chapter 6.3), the data rate with an APD as a single photon detector was quite small. For this thesis a growing of cat states in post processing was planned, so a lot of data points were needed.

An obvious improvement of the data rate was the usage of another single photon detector, which had a higher quantum efficiency than the currently used APD. For the used wavelength of 1064 nm, the APD technology is in general not the best. Therefore, other single photon technologies were searched and a promising device could be found: a superconducting nanowire single photon detector (SNSPD), for the theoretical background of these technology look to chapter 3.3.2. These kind of detectors reach very high quantum efficiencies above 85 % at 1064 nm [63]. At the same time it has other nice properties like very small dark count rates. However, the price of these detectors is quite high and could not be spent as part of the project budgetary. But it was possible to borrow such SNSPD from Boris Hage from the University of Rostock. This detector was built by the company "Single Quantum". It was custom made and no official data sheet exists, but Boris Hage told us following parameters: quantum efficiency around 90 % for 1064 nm, dead time around 70 ns - 80 ns, timing jitter below 100 ps and a dark count rate around 1 click per second. We could work with this detector for several weeks. Hence, it was enough time to measure a lot of cat states and try out different things like varying parameters as pump power, tap off and local oscillator power.

In this thesis only one large data set is shown, where 1300 million clicks were used to activate the data acquisition. It was a long time measurement over some hours, which was acquired by Felix Pein on 01.07.2021. The principle measurement procedure was exactly the same as reported in section 7.2. The only differences were concerning the SNSPD. Due to the high quantum efficiency the event rate was much higher. A direct comparison for constant parameters with the APD showed a factor 50 more clicks per second on the SNSPD.

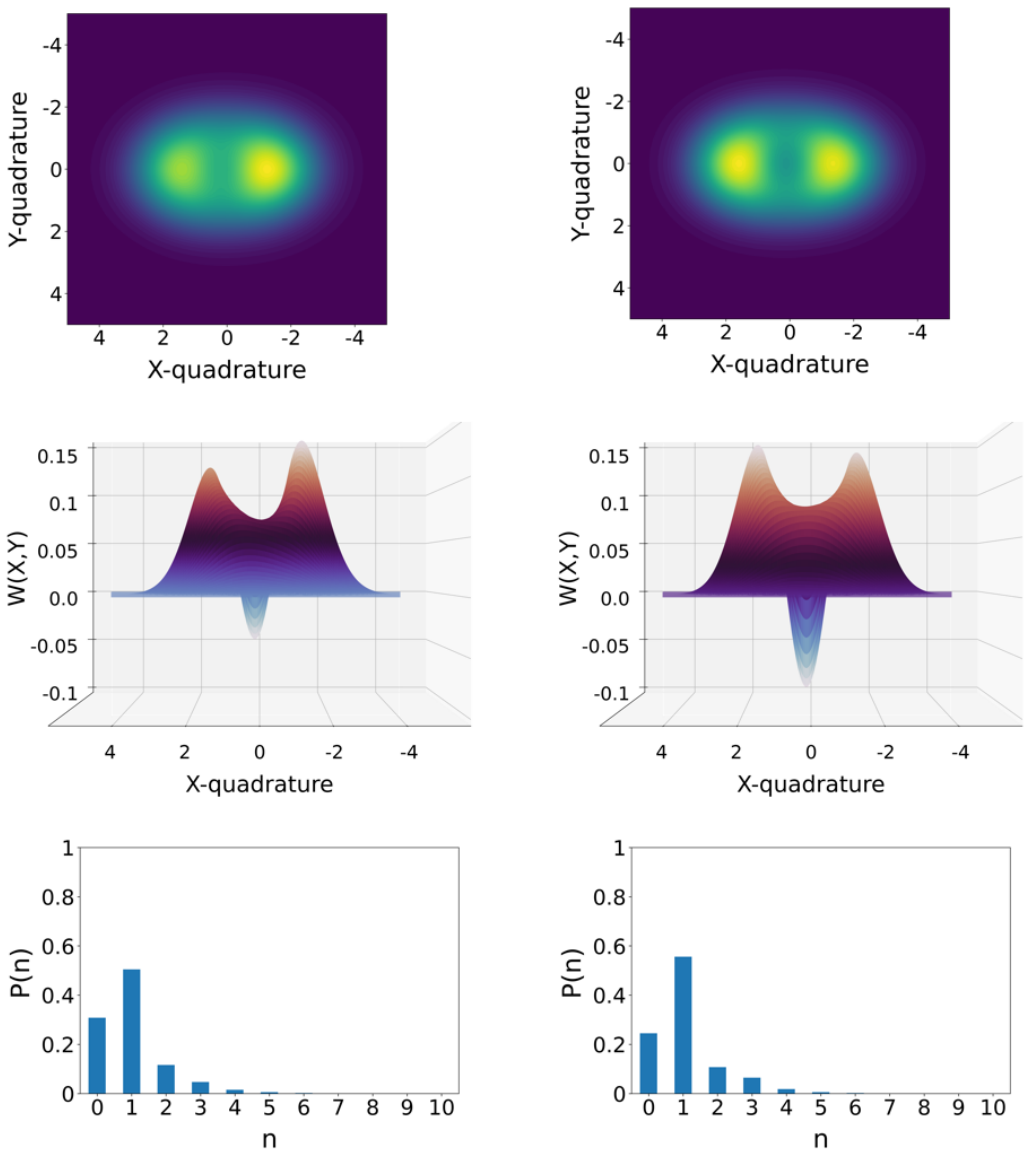

Figure 7.8: Schrödinger kitten state measurement results for APD (left) and SNSPD (right). The Q-function (top), Wigner function (middle) and photon statistics (bottom) are shown. The purity of the Schrödinger kitten state measured with SNSPD was higher than the APD measurement. This could be seen in all representations. The Q-function showed less noise in the center, the Wigner function had a larger negativity and in the photon statistics the vacuum contribution was smaller. Settings for the measurement: sampling rate 2.5 GSPS, pump power in front of the squeezer = 5 mW. The setup for this measurement is shown in figure 7.1. Data evaluation done with a MATLAB script written by Jaromír Fiurásek. Plots created with a Python script written by Felix Pein.

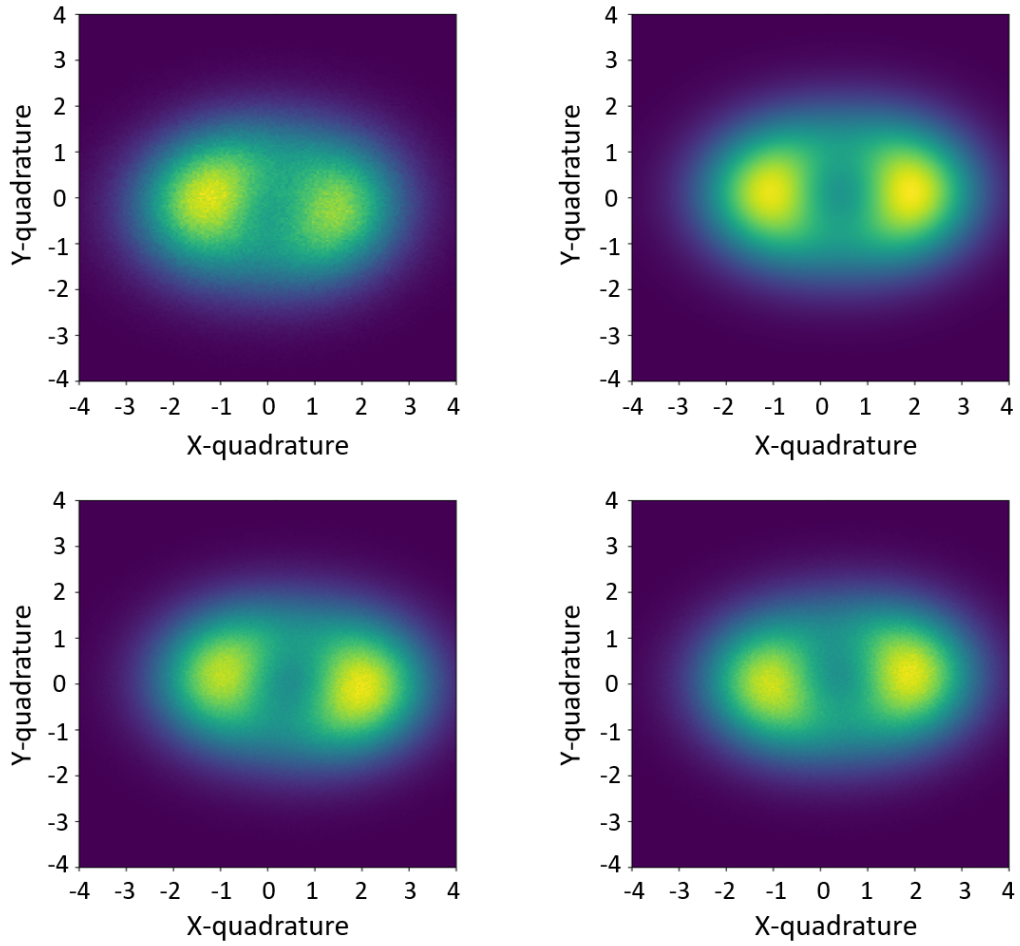

Figure 7.9: Schrödinger kitten state histograms. The APD measurement with 10 million data points shows a slightly rotation (top left). The total SNSPD measurement with 1300 million data points shows no rotation (top right). However, in partial data sets of 50 million data points also rotations are visible for the SNSPD with different orientation (bottom left and bottom right). Data evaluation done with a Python script written by Stephan Grebien and Felix Pein.

A higher factor of around 90 would be expected when the quantum efficiency from the APD is 1 % and the quantum efficiency from the SNSPD is 90 %. There are various possible explanations for the lower improvement factor. First the quantum efficiency measurement of the APD in chapter 6.3 was a rough estimation and no high precision measurement. Therefore, a result of around 1 % quantum efficiency could also be 1.2 % or maybe even more, which would already strongly decrease the improvement factor. Additionally, the quantum efficiency of the SNSPD might be smaller as the expected 90 %. On the one hand the quantum efficiency of the SNSPD depended on the polarization of the incoming signal. A half-wave plate and quarter-wave

plate were placed in front of the fiber coupler to maximize the click rate, but maybe not enough fine tuning was spent in this optimization and some percent quantum efficiency were lost. On the other hand, the quantum efficiency of the SNSPD depended on the applied bias voltage. This voltage should be high to reach a high quantum efficiency, but at the same time it had to be small enough to have a stable running detector. The bias voltage was set to 70 % of the maximal possible setting point. For this setting the detector was stable and the count rate was high, but maybe this setting was connected to a quantum efficiency below the maximal possible value. In principle there was one more parameter connected to single photon detectors which could explain the reduced improvement factor. Due to the high quantum efficiency the count rate might be so high that dead time effects played a role and suppressed some events. With the formula from equation 3.8 a dead time correction could be applied to recover these lost events. But for the used click rates in our experiment, the dead time effects were neglectable small. Probably the reason for the improvement factor of only 50 was a combination of the discussed possibilities. But a factor of 50 was still a strong improvement for the measurements, it allowed to reduce the tap off by several percent, which reduced the optical loss of the cat state and led to cat states with a higher purity. At the same time the data rate was still more than a factor 10 higher than the APD.

For the long time measurement presented in this thesis following parameters were used. The pump power was around 5 mW and the local oscillators were around 18 mW, which is the same configuration as was used for the APD measurement. The tap off was set to 2.5 %, which gave around 150 000 clicks per second on the SNSPD. The effective dark count rate was a few hundred clicks per second. Due to the low intrinsic dark count rate of 1 clicks per second the reason for these dark counts were other light sources in the lab like room light, stray light and control lamps on photo diodes. In principle the effective dark count rate could be reduced by better shielding the fiber coupler, but compared to a click rate of 150 000 clicks per second a dark count rate of a few hundred clicks per second could be neglected and no time was spent in optimizations. Also, the data acquisition settings had to be adjusted because the SNSPD had another delay as the APD. The amount of samples was set to 80.

The data evaluation was the same as reported in section 7.3. Figure 7.8 right side shows the results with a SNSPD. It is clearly visible that the purity of the Schrödinger kitten state could be increased by exchanging the single

photon detector. In comparison to the APD results in figure 7.8 left side the Q-function showed less noise in the center, the Wigner function had a larger negativity and in the photon statistics the vacuum contribution was smaller. Felix Pein tried to quantify the loss differences with various fitting models, but the results were inconsistent and did not match to the expected loss reduction from the tap off change and signal to noise ratio improvement. For example a fit to a Q-function with loss model [40, p.61-62] leaded to a total loss of 34 % for the APD kitten state measurement while it was still 31 % for the SNSPD measurement. But the tap off was reduced from 10 % to 2.5 % and at the same time the loss contribution through dark counts was improved from above 1 % to below 1 %. Probably the asymmetry, which was visible in the APD and the SNSPD measurement, made fitting difficult and reduced the validity of the out coming parameters. Hence, the reported loss values can only be seen as a rough estimation. The fitting process also gave out a value for the amplitude α which was 1.0 for the APD measurement and 1.1 for the SNSPD measurement.

The high event rate of the SNSPD gave the possibility to get very fast enough data points to compare cat states for different parameter settings in the experimental setup. This allowed us to try out different things to investigate the asymmetry problem. A possible explanation for the asymmetry might be a mixing of the odd cat state with a coherent state with a very small α. Therefore, the reason of a copropagating weakly coherent state at 1064 nm was searched. An obvious candidate for a coherent state at 1064 nm is the local oscillator. As discussed in section 7.1 a Faraday isolator had to be installed because some light of the local oscillator was scattered to the squeezing resonator. Even if this Faraday isolator had a good suppression there might be some leakage and, consequently, some local oscillator in the signal mode. But if the asymmetry was really caused by the local oscillator, the local oscillator power should have an influence to the asymmetry. Kitten state measurements with different local oscillator powers were done, but no systematic changes in the asymmetry could be observed. Therefore, the local oscillator was unlikely as reason.

Another 1064 nm field on the optical table was the control field. As discussed in section 7.2 the control field was blocked during the measurements with a beam dumb. In principle these beam dumps were quite trustworthy, but to be absolutely sure that no light from the control field entered the squeezing resonator, a plate was placed behind the beam dump to have a

double blocking stage. Nevertheless, no improvements were visible referring to the asymmetry.

Another idea was tried out: filtering the pump field with a laser line filter FL05532-1 from Thorlabs. The pump field was generated from 1064 nm light through second harmonic generation, so there might be some 1064 nm light inside the pump field. The laser line filter would suppress the 1064 nm contamination. But kitten state measurements with this laser line filter still showed the asymmetry. Hence, this idea, which was suggested by Boris Hage, did not explain the asymmetry. Also, using different pump powers or different tap off values did not help.

Maybe the origin of the coherent state was inside the squeezing resonator due to a conversion process from the pump field. In this case the asymmetry might be influenced with parameters from the squeezing resonator like the used coatings and resulting intra cavity losses. But systematically manipulating these parameters would be rather complicated and time consuming. Therefore, this possibility could not be investigated. In the end there was no way to control or remove the asymmetry during the measurements.

Furthermore, in the APD measurement from figure 7.9 top left a slightly rotation of the cat state is visible. As opposed to this in the SNSPD measurement from figure 7.9 top right no rotation is visible. But when only partial data sets of 50 million data points from the SNSPD measurement were evaluated, then also slightly rotations get visible, as can be seen in the bottom area of figure 7.9 for 2 example partial data sets. However, over all 1300 million data points these rotations seem to average out. A parameter could be identified which influenced the rotation angle. It was the stabilization point of the anti-squeezed noise envelope phase lock. By changing this locking point with an offset button of the used servo, the rotation angle could be controlled. But even when the locking point was in a good position and no rotation was visible at the beginning of a measurement it came to some drifts while the measurement was running. It was not possible to fix this while the SNSPD was available.

7.5 Growing of cat states in post processing

1200 million quadrature pairs from the long time measurement presented in the previous section 7.4 were used for the post processing to achieve cat states with larger amplitudes. Therefore, this 1200 million quadrature pairs were split in two data sets with 600 million each. The two sets were overlapped

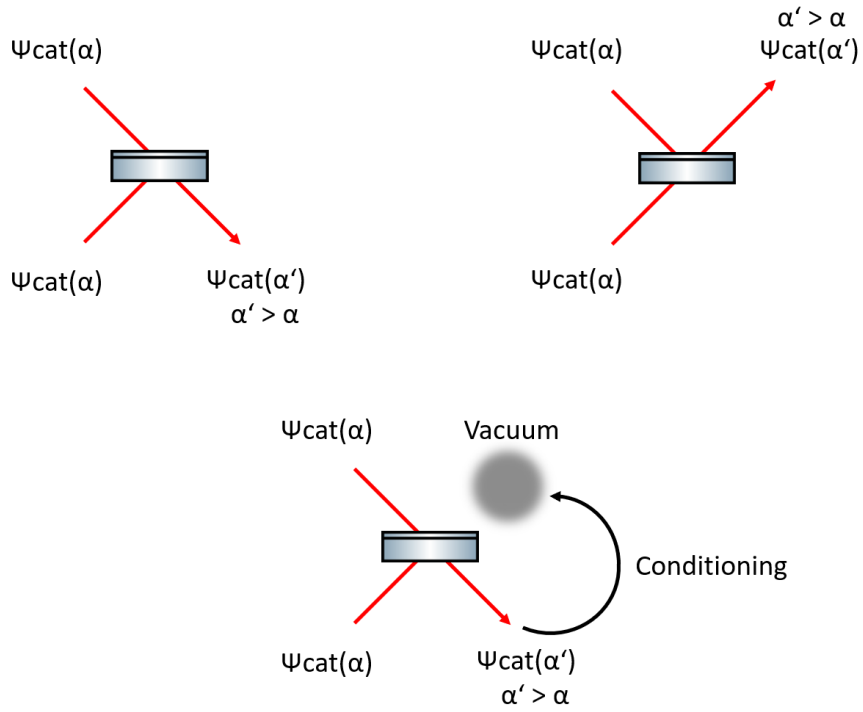

Figure 7.10: Post processing basic idea. The top side of the picture shows what can happen, when a cat state is superimposed with another indistinguishable cat state on a 50/50 beam splitter. Either a cat state with larger amplitude appears in the bottom beam splitter output port and the top port is empty or it is the other way round and a cat state with larger amplitude appears in the top port and the bottom port is empty. The outcome is randomly distributed and cannot be predicted. The bottom side of the picture illustrates how a cat state could be identified in one beam splitter output port, for example, the bottom one. Therefore, the top output port was used for a vacuum conditioning. Consequently, in the bottom output only the quadrature pairs were considered, when the corresponding quadrature pair in the top port was inside the vacuum circle. Picture created with Inkscape referring to [10, p.380].

on a beam splitter by using equation 3.17. One beam splitter output port was used for a vacuum conditioning. That means when the quadrature pair in this conditioning port was inside a defined circle around zero, the other beam splitter output port was accepted and stored. When the conditioning port result was outside the circle, the quadrature pair in the other output port was thrown away. Hence, the post processing reduced the amount of quadrature pairs, but the remaining quadrature pairs represented a cat state with a larger amplitude analog to the pure experimental realization in [10]. Plenty of 7.4 million quadrature pairs survived the post processing. They were divided in 2 equal parts again to repeat the procedure and further increase the amplitude. Only 370 000 quadrature pairs were remaining, which

was not enough to do a third step. Figure 7.10 illustrates the basic idea of the post processing. The post processing was done by Jaromír Fiurásek, it was integrated in the MATLAB data evaluation script mentioned in section 7.3. The density matrices after post processing are shown in appendix A.1.

Figure 7.11 shows the results of the post processing. The measured state from figure 7.8 right side is shown again for comparison. Additionally, the results in terms of Q-functions and Wigner functions are shown for both growing steps. It can be seen that the post processing increased the amplitude α because the intensity hills in Q and Wigner function drifted apart. While the initial state had an α of 1.1, the first step post processing could increase it to 1.7 and after the second step it was already 2.6. But the negativity in the Wigner function was destroyed after the post processing because the higher amplitudes were more sensitive for optical loss. Additionally, the loss seemed to be increased by the post processing. At least Felix Pein's fitting code [40, p.61-62] gave out following values: 31 % for the measured state, 37 % after the first step and 42 % after the second step. But as discussed before in section 7.4 the fitting parameter are not fully trustable. However, an increasing loss sounded reasonable because accordingly to Jaromír Fiurásek the post processing could also amplify the noise.

In the photon statistics also changes were visible, as can be seen in figure 7.12. After the post processing more higher photon number states were populated. The modal value was 1 for the measured state. After the first step post processing the modal value was 2 and after the second step it was 4. Due to the high loss, even and odd photon numbers were populated approximately equally. Nevertheless, the development of the modal value could be seen as a hint that an odd cat state was transferred into an even cat state, as expected [10, p.379]. Also, the scaling factor of the amplitudes was close to the predicted factor of $\sqrt{2}$ per step [12, p.8]. In conclusion, the post processing gave plausible results.

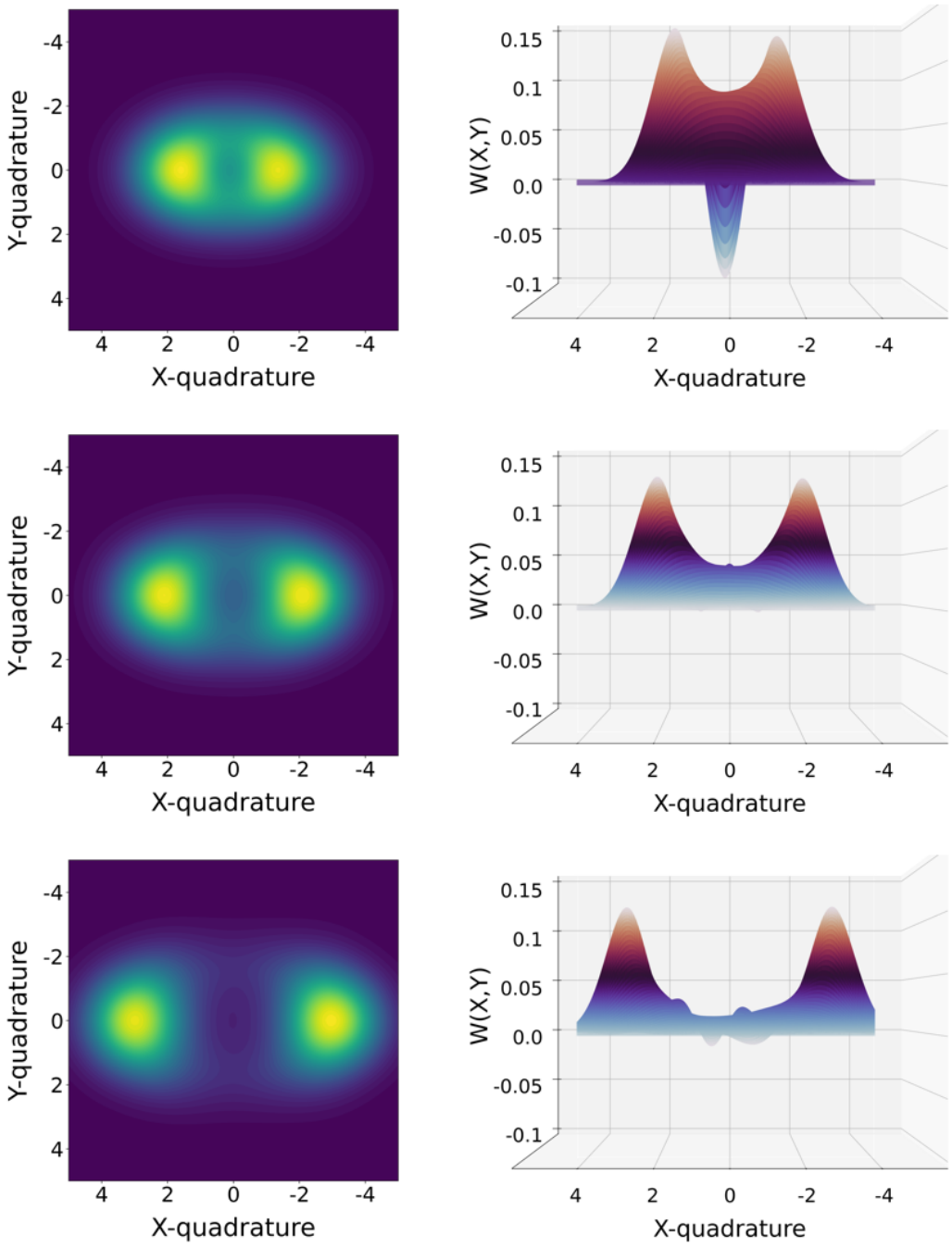

Figure 7.11: Schrödinger kitten state results of the post processing (first step: middle row, second step: bottom row) and comparison to the measured state (top row) are presented. The Q-functions (left column) and Wigner functions (right column) are shown. It is clearly to see that the post processing increased the amplitude α because the intensity hills in Q and Wigner function drifted apart. The initial state had an α of 1.1. After the first step post processing it was already 1.7 and after the second step it was 2.6, but the negativity in the Wigner function was destroyed after the post processing because the higher amplitudes were more sensitive for optical loss. Post processing done with a MATLAB script written by Jaromír Fiurásek. Plots created with a Python script written by Felix Pein.

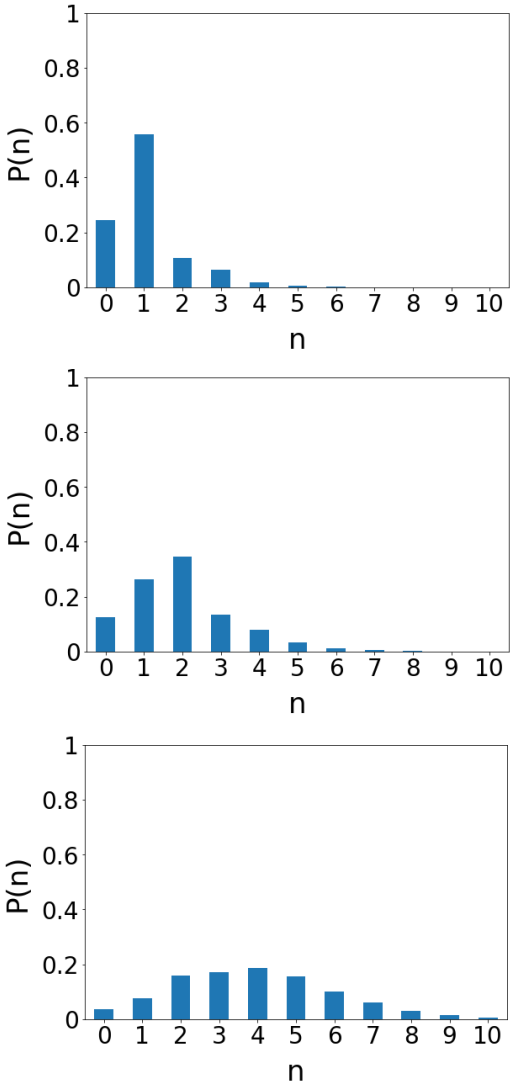

Figure 7.12: Schrödinger kitten state photon statistics of the post processing (first step: middle, second step: bottom) and comparison to the measured state (top) are presented. The modal value was 1 for the measured state. After the first step post processing the modal value was 2 and after the second step it was 4. Post processing done with a MATLAB script written by Jaromír Fiurásek. Plots created with a Python script written by Felix Pein.

Chapter 8

Discussion and outlook

In this chapter the central results of the thesis are summarized and discussed. The same chronology as in the thesis is used. First the continuously measurements of squeezed states are presented, then the discrete measurements with single photon detectors are discussed and, finally, the hybrid measurements with both techniques at the same time are processed. At the end of this chapter an outlook is given, which shows how the experiment could be expanded in the future.

8.1 Discussion

The highest squeeze value which could be observed in this thesis was 10.6 dB measured at 1064 nm. For this measurement, a conventional balanced homodyne detection was used and the phase of the local oscillator was stabilized by hand. This value looked quite small in comparison to the squeeze record of 15.0 dB measured at 1064 nm [64]. But it was never the plan to reach the squeeze record and not too much time was spent into the loss minimization. For example, the mode matchings to the diagnostic mode cleaner for achieving a good visibility were only around 99.0 %. For coming closer to the squeeze record the goal would be 99.9 %. Another avoidable loss source came from the 5 lenses which were placed between squeezing resonator and balanced homodyne detector. To come closer to the squeeze record a more efficient setup with a smaller amount of optics need to be used. Nevertheless, a squeeze value above 10 dB was still a good result because it indicated that the optical loss had to be below 10 %, which was already a good basis for the further experiment. Jan Südbeck installed an identically constructed squeezing resonator on another optical table and reached a very similar squeeze value of 10.7 dB [65, p.61-62].

To be able to do measurements over longer time scales, the phase of the local oscillator was stabilized with the noise envelope locking technique [55].

Therefore, a modulation frequency was applied to the local oscillator phase shifter. An error signal was generated, which could be used to stabilize the phase shifter to the maximal noise level (anti-squeezing) or minimal noise level (squeezing). The advantage of this technique was that no copropagating coherent fields were necessary, which was recommended for the cat state measurements because a single photon detector was part of the experiment, which should not get in contact with a strong coherent field.

For the single photon detection, initially a COUNT NIR avalanche photo diode (APD) from Laser Components was used. The quantum efficiency was measured and was around 1 % for the wavelength of 1064 nm. The data sheet predicts a higher quantum efficiency of around $5\,\% - 7\,\%$, but also tells that the fiber coupler is just optimized for the wavelength range from 440 nm to 1000 nm [41, p.3]. Probability for 1064 nm the fiber coupler introduced additional loss, which was the reason for the low measured quantum efficiency. To confirm that the experimental setup worked correctly, another detector (AQRH) was characterized, which is specified up to 1060 nm [57, p.1]. Hence, it was better suitable for the operating wavelength of 1064 nm. The measured quantum efficiency at 1064 nm was also around 1 %, but for the AQRH this value is in good agreement to the data sheet, which predicts $1\,\% - 2\,\%$ quantum efficiency at 1064 nm [57, p.2]. In conclusion, the measured quantum efficiencies seems to be valid. For the further measurements, the COUNT NIR was used because it showed only around 35 dark counts per second, which was much better than the AQRH with around 260 dark counts per second.

Schrödinger kitten states could be created by subtracting a single photon from a weakly squeezed state analog to [6]. The characterization was done via an 8-port homodyne detection, which could directly measure the Q-function of a quantum state of light [28, p.153]. For this measurement 10 million quadrature pairs were acquired. By fitting a Q-function with loss to the data an $\alpha = 1.0$ and approximate loss of 34 % was received. The amplitude was similar as in other experiments where Schrödinger kitten states were created by subtracting a single photon from a weakly squeezed state as well [6]. Also, the density matrix could be extracted from the measured 8-port data via a maximum likelihood estimation [62]. The density matrix allowed to plot the Wigner function and photon statistics of the measured Schrödinger kitten states.

The Schrödinger kitten state measurements could be improved by exchanging the single photon detector. Instead of the avalanche photo diode a

superconducting nanowire single photon detector (SNSPD) was used, which can reach a much higher quantum efficiency of above 90 % at 1064 nm, furthermore, it had more or less no dark counts. Therefore, the signal to noise ratio was better, which reduced the loss coupled in through dark counts and, additionally, the tap off to the detector could be reduced, which also saved some percent loss. A Schrödinger kitten state with $\alpha = 1.1$ and approximate loss of 31 % could be measured. The data rate with SNSPD was much higher compared to the APD measurements.

Some unexpected features were visible in the measured data: an asymmetric intensity distribution and small rotations. For the rotation the reason could be identified. It was caused by fluctuations in the setting point of the noise envelope phase lock for the anti-squeezed quadrature. But it was not possible to solve this issue. The reason for the asymmetry could not be clarified. Roman Schnabel suggested following idea: it might be connected to the squeeze operation itself. Lossy squeezed states inside the squeezing resonator might be amplified by induced emission to weak coherent states. To proof this idea further investigations would be necessary like systematically changing parameters of the squeezing resonator. For example, the intra cavity loss could be manipulated by using different coupling mirrors with varying reflectivity for 1064 nm. But this would be a lot of effort because exchanging a coupling mirror is connected with much realignment to repair the mode matchings of the light fields to the squeezing resonator and from the squeezing resonator to the diagnostic mode cleaners.

The asymmetry brought two disadvantages. On the one hand it reduced the purity of the measured Schrödinger kitten states because something else is mixed in. On the other hand, it caused difficulties for fitting the data. Therefore, the reported cat state characterization, in terms of amplitudes α and loss values, is not fully trustable. Even when the fits are not fully trustable to characterize the loss. A comparison of our measured states with simulated lossy states by eye also gave a rough total loss estimation in the order of $30\,\% - 40\,\%$.

In general the loss values look quite high referring to the quantified loss sources like below 10 % loss from the squeezed-light source + 3 % loss from the Faraday isolator + tap off (10 % for APD or 2.5 % for SNSPD) and a dark count contribution of the single photon detector (a little bit above 1 % for APD or below 1 % for SNSPD). But beside these loss sources there were other noise sources, which were not quantified like noise through the data acquisition because of a finite resolution or noise due to the measurements over

a broad spectrum. On the one hand the squeezing spectra contained oscillations and some extra peaks from electronic devices in the lab. Therefore, the loss characterization, which was done at a sideband frequency of 5 MHz with a resolution bandwidth of 300 kHz, is not valid for the whole spectrum. Furthermore, the Schrödinger kitten state generation over a broadband spectrum mixed different Schrödinger kitten states together, which also smoothed out the measured state. The observed rotations in partial data sets, caused by non perfect phase locking, further smoothed out the results. Maybe the not quantified noise sources were so strong that above 30 % total loss estimation is still realistic.

The high quantum efficiency of the SNSPD made it possible to collect large amounts of data in a reasonable time window. Around 1300 million quadrature pairs could be measured and were used for a post processing to grow the cat states. Therefore, 1200 million quadrature pairs were taken and split into two sets with 600 million data points. By emulating the interference of the data points on a 50/50 beam splitter and doing a vacuum conditioning in one output port, a higher cat state amplitude in the other output port could be reached. The first step increased the amplitude from $\alpha = 1.1$ to $\alpha = 1.7$. But the post processing strongly reduced the amount of quadrature pairs from 1200 million to 7.4 million. The remaining amount of quadrature pairs were large enough to do a second step. Thereby the amplitude could be further increased to $\alpha = 2.6$ and the amount of quadrature pairs was further reduced to 370 000. For a third step this amount of quadrature pairs was too small. The scaling factor of the amplitudes α was close to the predicted factor of $\sqrt{2}$ per step [12, p.8]. The post processing destroyed the negativity in the Wigner functions. Two effects could play a role. On the one hand the post processing seemed to increase the loss because the impurities of the states were also amplified. On the other hand, a higher cat state amplitude is much more sensitive to optical loss and the negativity is already destroyed for smaller loss values.

The presented experiment can be improved with different approaches. The optical loss can be reduced by using better or less optics or by improving the mode matchings to the diagnostic mode cleaners. A better data acquisition card could be bought, which has a higher sampling rate and more bits to improve the resolution. Alternatively, with the used data acquisition card an optimization might be possible because the measurement range is 500 mV [61, p.3], but the homodyne detector signals were only around 20 mV peak to

peak. During the measurements, no suitable amplifier was available. Therefore, the 12 bit vertical resolution was not fully used. By implementing an amplifier to increase the detector signals to the given measurement range a better resolution would be reached.

Better locking performances would also be an enhancement. The noise envelope phase locks had to be relocked a few times per hour and they caused some rotations of the measured Schrödinger kitten states. Therefore, a more stable phase lock would reduce the phase noise. At the same time measurements over longer time scales would be possible and the tap off to the single photon detector could be further reduced, which would also improve the purity of the measured Schrödinger kitten states. For much smaller tap off values the observed dark counts could play a role. But for the SNSPD the observed few hundred dark counts were triggered by light sources from the lab, which could be filtered out by better shielding of the fibre coupler. The filter cavities were locked by hand, so an automatic locking system would also be a simplification for the measurement procedure. Another lock which had to be relocked from time to time was the pre mode cleaner. It was stabilized only with a Pound-Drever-Hall lock, which controlled a piezoelectric actuated mirror. By implementing a temperature controller, as it is meanwhile standard in other experiments in our group, the long term stability could be increased.

Also, some oscillations in the squeezing spectra could be observed, which were introduced by signal splitting electronics. Maybe a better solution could be found, which avoids these oscillations and gives a more flat and equal spectrum in both homodyne detectors. Maybe the discussed possibilities would increase the purity of the measured cat states so far that also after the post processing a clear negativity might be visible in the Wigner functions.

This thesis shows Schrödinger kitten states with an amplitude α above 2, which is the threshold for qubit applications [13, p.1]. They were generated by superimposing smaller Schrödinger kitten states on an emulated beam splitter with 2 iterations. The resulting grown Schrödinger kitten states are unlikely for an application as qubit due to strong decoherence by optical loss and other noise sources. The grown states are only available as already measured data points inside a computer. For an experimental usable state, a setup with 4 squeezing resonators and a 4 single photon detector coincidence would be necessary, which is challenging to realize.

8.2 Outlook

The long term goal is to transfer the cat state experiment into an entanglement distillation. The basic idea of a distillation is to extract a low amount of strongly nonclassical states from a high amount of weakly nonclassical states [22]. Distillation could be useful for quantum cryptography [23][24][25] by increasing the possible distance of quantum key distribution [19][26]. But distillation is not always possible. It could be shown that it is not possible to distill Gaussian states with Gaussian operations [66][67][68]. Gaussian states are quantum states of light with a Gaussian Wigner function [69, p.2]. For example, squeezed states of light are Gaussian states. Gaussian operations are operations which transform a Gaussian state into another Gaussian state [69, p.2]. Some examples for Gaussian operations are beam splitters, homodyne detectors and squeezing resonators.

The impossibility to distill Gaussian states with Gaussian operations is a "no-go" theorem [19, p.178]. To make a distillation possible, the no-go theorem has to be circumvented. This could be done by using a non Gaussian state instead of a Gaussian state. A Gaussian state is transformed into a non Gaussian state by phase noise. Phase noise is coupled in by using fibers or can artificially created by using a piezoelectric actuated mirror which imprints a disturbance frequency [69, p.3-4]. For such non Gaussian states, a distillation against phase noise can be performed. This kind of distillation from non Gaussian states with Gaussian operations was already done in our working group from the former group members Daniela Abdelkhalek and Alexander Franzen [26][45][69][70].

Another method to circumvent the no-go theorem is using a non Gaussian operation instead of a Gaussian operation. A typical example of a non Gaussian operation is a single photon detection [19, p.178]. Through the single photon detection a distillation from Gaussian states against optical loss can be performed. This kind of distillation was already done for entangled states by Takahashi et al. [19]. Figure 8.1 shows the setup of these entanglement distillation. A v-class entangled state was prepared by overlapping a squeezed state with a vacuum state on a 50/50 beam splitter. From both beam splitter outputs a small amount was tapped of to a single photon detector. The rest of the signals was sent to conventional balanced homodyne detectors, which read out the same quadrature. The entanglement could be seen by adding or subtracting the signals from the balanced homodyne detectors.

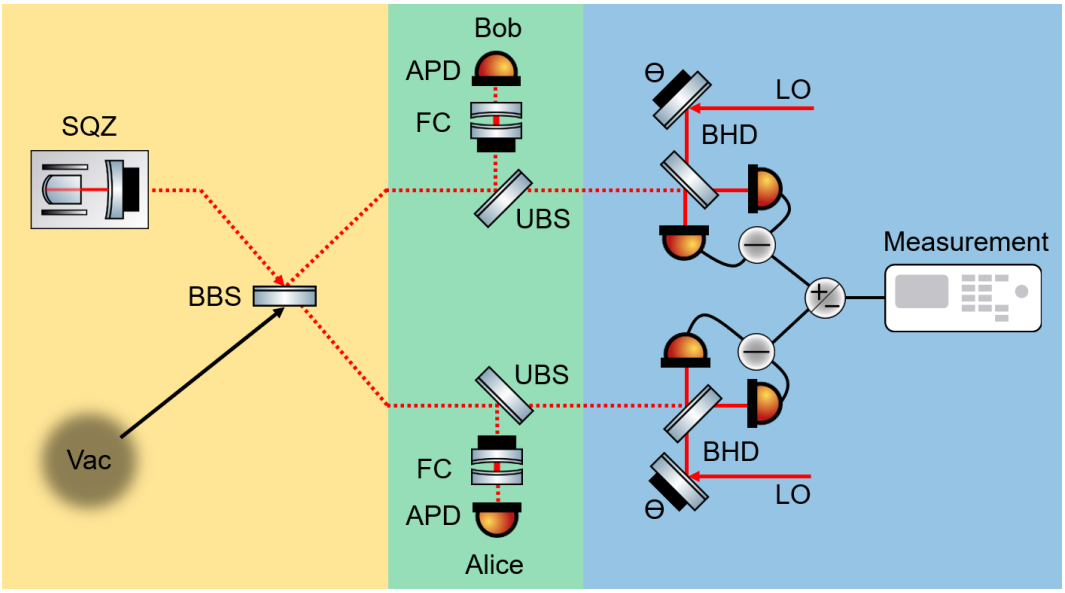

Figure 8.1: Setup of an entanglement distillation from Gaussian states with non Gaussian operations. An entangled state is prepared (yellow) by generating a squeezed state (SQZ) and overlap it with a vacuum state (Vac) on a balanced beam splitter (BBS). Alice and Bob both tapped off a small amount of their signal with an unbalanced beam splitter (UBS) and sent it through a filter cavity (FC) to a single photon detector (APD) to do the distillation (green). The state verification (blue) was done with conventional balanced homodyne detectors (BHD). Therefore, Alice and Bob read out the same quadrature Θ, which could be chosen by controlling the phase of the local oscillator (LO) with a piezoelectric actuated mirror. The entanglement could be seen by reading out the added (+) or subtracted (-) BHD signals with a measurement device. Picture created with Microsoft Power Point referring to [19, p.178].

Figure 8.2 shows the results of the entanglement distillation from Gaussian states with non Gaussian operations, realized by Takahashi et al. [19]. The entanglement strength is shown as logarithmic negativity for different initial squeeze values. The entanglement strength was increased, when the balanced homodyne detector measurements were conditioned to a single photon subtraction with one single photon detector or a two photon subtraction with both single photon detectors. For the single photon subtraction, the magnification of the entanglement strength was even higher than the two photon subtraction. The Wigner functions of the conditioned states looked also different. For a single photon subtraction the Wigner function looked like an odd cat state with a negativity at the origin. For a two photon subtraction the Wigner function looked like a deformed Gaussian state. Without conditioning to the single photon detectors the Wigner function represented a Gaussian state.

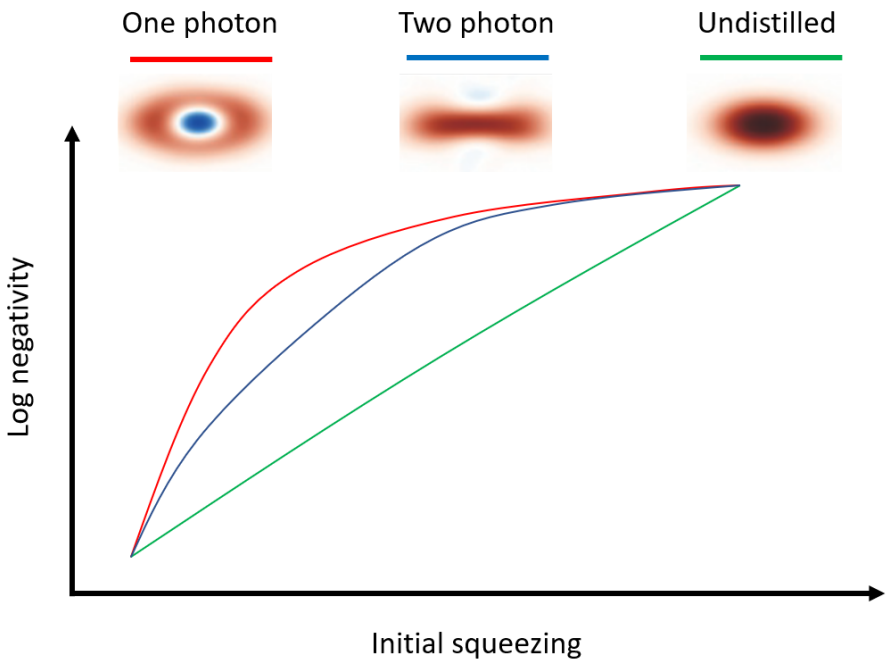

Figure 8.2: Results of an entanglement distillation from Gaussian states with non Gaussian operations. The logarithmic (Log) negativity is shown in dependence of the initial squeezing. A single photon subtraction (red) increased the entanglement strength compared to the undistilled case (green). A two photon subtraction (blue) also increased the entanglement strength, but a little bit smaller than the single photon subtraction. The Wigner function of the single photon subtracted state had a negativity and looked like an odd cat state. The Wigner function of the two photon subtracted state looked like a deformed Gaussian state. The undistilled data were represented by a Gaussian Wigner function. Picture created with Microsoft Power Point referring to [19, p.179].

For our planned entanglement distillation the setup will be a little bit different as shown in figure 8.1. Instead of a conventional homodyne detection, an 8-port homodyne detection will be used for Alice and for Bob. Both will split their signal on a 50/50 beam splitter and measure the amplitude and phase quadrature at the same time. Therefore, in total 4 balanced homodyne detectors will be necessary. The advantage of this method is the possibility to do a further distillation in post processing. Accordingly to Jaromir Fiurásek, the post processing will only work for two photon subtracted states. With the cat state setup in figure 7.1 and the superconducting nanowire detector already some experience with two photon subtraction could be collected. The superconducting nanowire detector from the University of Rostock (Boris Hage's working group) contained 4 channels. For the measurements presented in this thesis only one channel was used, but measurements with two

channels were already performed and evaluated. By subtracting two photons from a squeezed state, an improvement in the squeeze factor could be reached (squeezing distillation). These results will be part of Stephan Grebien's doctor thesis.

In figure 8.1 v-class entanglement is generated by overlapping a squeezed state with a vacuum state on a 50/50 beam splitter. The long term goal for our experiment will be the usage of s-class entanglement. Therefore, two orthogonal squeezed states are superimposed on a 50/50 beam splitter [71]. Of course, for that a second squeezing resonator has to be built and installed on the optical table. The advantage of s-class entanglement is a stronger entanglement strength [53], which is useful for applications in quantum cryptography [25].

Appendix

A.1 Density matrices

$$\begin{pmatrix}
0.308 & -0.050 & 0.122 & -0.023 & 0.036 & -0.006 & 0.011 & -0.002 \\
-0.050 & 0.505 & 0.024 & 0.135 & 0.010 & 0.032 & 0.003 & 0.008 \\
0.122 & 0.024 & 0.116 & 0.004 & 0.040 & 0.002 & 0.012 & 0.001 \\
-0.023 & 0.135 & 0.004 & 0.047 & -0.001 & 0.014 & -0.001 & 0.004 \\
0.036 & 0.010 & 0.040 & -0.001 & 0.015 & -0.001 & 0.005 & 0.0 \\
-0.006 & 0.032 & 0.002 & 0.014 & -0.001 & 0.006 & 0.0 & 0.002 \\
0.011 & 0.003 & 0.012 & -0.001 & 0.005 & 0.0 & 0.002 & 0.0 \\
-0.002 & 0.008 & 0.001 & 0.004 & 0.0 & 0.002 & 0.0 & 0.001
\end{pmatrix}$$

$$\begin{pmatrix}
0.245 & -0.039 & 0.106 & -0.004 & 0.041 & 0.0 & 0.014 & 0.0 \\
-0.039 & 0.556 & 0.046 & 0.186 & 0.020 & 0.053 & 0.007 & 0.015 \\
0.106 & 0.046 & 0.108 & 0.019 & 0.044 & 0.005 & 0.015 & 0.001 \\
-0.004 & 0.186 & 0.019 & 0.064 & 0.008 & 0.019 & 0.003 & 0.005 \\
0.041 & 0.020 & 0.044 & 0.008 & 0.018 & 0.002 & 0.006 & 0.0 \\
0.0 & 0.053 & 0.005 & 0.019 & 0.002 & 0.006 & 0.001 & 0.002 \\
0.014 & 0.007 & 0.015 & 0.003 & 0.006 & 0.001 & 0.002 & 0.0 \\
0.0 & 0.015 & 0.001 & 0.005 & 0.0 & 0.002 & 0.0 & 0.001
\end{pmatrix}$$

$$\begin{pmatrix}
0.124 & 0.001 & 0.045 & 0.0 & 0.020 & 0.001 & 0.008 & 0.001 \\
0.001 & 0.263 & -0.002 & 0.155 & 0.0 & 0.067 & 0.0 & 0.026 \\
0.045 & -0.002 & 0.345 & 0.001 & 0.163 & 0.0 & 0.061 & -0.001 \\
0.0 & 0.155 & 0.001 & 0.136 & 0.0 & 0.066 & 0.0 & 0.027 \\
0.020 & 0.0 & 0.163 & 0.0 & 0.079 & 0.0 & 0.031 & -0.001 \\
0.001 & 0.067 & 0.0 & 0.066 & 0.0 & 0.033 & 0.0 & 0.014 \\
0.008 & 0.0 & 0.061 & 0.0 & 0.031 & 0.0 & 0.012 & 0.0 \\
0.001 & 0.026 & -0.001 & 0.027 & -0.001 & 0.014 & 0.0 & 0.006
\end{pmatrix}$$

$$\begin{pmatrix}
0.037 & -0.001 & 0.018 & -0.001 & 0.022 & 0.002 & 0.019 & 0.002 \\
-0.001 & 0.077 & 0.011 & 0.043 & 0.006 & 0.017 & -0.003 & 0.013 \\
0.018 & 0.011 & 0.160 & -0.023 & 0.108 & -0.015 & 0.057 & -0.009 \\
-0.001 & 0.043 & -0.023 & 0.171 & 0.008 & 0.148 & 0.001 & 0.087 \\
0.022 & 0.006 & 0.108 & 0.008 & 0.185 & 0.006 & 0.131 & 0.001 \\
0.002 & 0.017 & -0.015 & 0.148 & 0.006 & 0.156 & -0.001 & 0.095 \\
0.019 & -0.003 & 0.057 & 0.001 & 0.131 & -0.001 & 0.099 & -0.003 \\
0.002 & 0.013 & -0.009 & 0.087 & 0.001 & 0.095 & -0.003 & 0.060
\end{pmatrix}$$

Figure A.1: Density matrices for the results presented in this thesis. From up to down: measurement with APD, measurement with SNSPD, post processing first step and post processing second step. Density matrices are extracted from the measured Q-functions by using a MATLAB script written by Jaromír Fiurásek, which is based on maximum likelihood estimation.

Bibliography

[1] E. Schrödinger. "Die gegenwärtige Situation in der Quantenmechanik". In: *Die Naturwissenschaften* 23 (1935), p. 807–849.

[2] C. Qiu et al. "Atom–light superposition oscillation and Ramsey-like atom–light interferometer". In: *Optica* 3 (2016), p. 775–780.

[3] S. Massar and E. S. Polzik. "Generating a Superposition of Spin States in an Atomic Ensemble". In: *Phys. Rev. Lett.* 91 (2003), p. 060401.

[4] S. Zhdanovich, J. W. Hepburn, and V. Milner. "Strong-field effects in Rabi oscillations between a single state and a superposition of states". In: *Phys. Rev. A* 84 (2011), p. 053428.

[5] C. Gerry and P. Knight. *Introductory Quantum Optics*. Campridge Univ. Press, 2005.

[6] J. S. Neergaard-Nielsen et al. "Generation of a Superposition of Odd Photon Number States for Quantum Information Networks". In: *Phys. Rev. Lett.* 97 (2006), p. 083604.

[7] A. Ourjoumtsev et al. "Generating Optical Schrödinger Kittens for Quantum Information Processing". In: *Science* 312 (2006), p. 83–86.

[8] P. Lahti, J.-P. Pellonpää, and J. Schultz. "Realistic eight-port homodyne detection and covariant phase space observables". In: *Journal of Modern Optics* 57 (2010), p. 1171–1179.

[9] C. K. Hong, Z. Y. Ou, and L. Mandel. "Measurement of subpicosecond time intervals between two photons by interference". In: *Phys. Rev. Lett.* 59 (1987), p. 2044–2046.

[10] D.V. Sychev et al. "Enlargement of optical Schrödinger's cat states". In: *Nature Photon* 11 (2017), p. 379–382.

[11] A. P. Lund et al. "Conditional production of superpositions of coherent states with inefficient photon detection". In: *Phys. Rev. A* 70 (2004), p. 020101.

[12] A. Laghaout et al. "Amplification of realistic Schrödinger-cat-state-like states by homodyne heralding". In: *Phys. Rev. A* 87 (2013), p. 043826.

[13] T. C. Ralph et al. “Quantum computation with optical coherent states”. In: *Phys. Rev. A* 68 (2003), p. 042319.

[14] M. A. Nielsen and I. L. Chuang. *Quantum Computation and Quantum Information*. 10th Anniversary Edition. Campridge Univ. Press, 2010.

[15] T. D. Ladd et al. “Quantum computers”. In: *Nature* 464 (2010), p. 45–53.

[16] A. I. Lvovsky et al. “Quantum State Reconstruction of the Single-Photon Fock State”. In: *Phys. Rev. Lett.* 87 (2001), p. 050402.

[17] K. Wakui et al. “Photon subtracted squeezed states generated with periodically poled KTiOPO4”. In: *Optics Express* 15 (2007), p. 3568–3574.

[18] C. Baune, J. Fiurášek, and R. Schnabel. “Negative Wigner function at telecommunication wavelength from homodyne detection”. In: *Phys. Rev. A* 95 (2017), p. 061802.

[19] H. Takahashi et al. “Entanglement distillation from Gaussian input states”. In: *Nature Photon* 4 (2010), p. 178–181.

[20] Y. Kurochkin, A. S. Prasad, and A.I. Lvovsky. “Distillation of The Two-Mode Squeezed State”. In: *Phys. Rev. Lett.* 112 (2014), p. 070402.

[21] U.L. Andersen et al. “Hybrid discrete- and continuous-variable quantum information”. In: *Nature Phys* 11 (2015), p. 713–719.

[22] C.H. Bennett et al. “Purification of Noisy Entanglement and Faithful Teleportation via Noisy Channels”. In: *Phys. Rev. Lett.* 76 (1996), p. 722–725.

[23] C.H. Bennett and G. Brassard. “Quantum cryptography: Public key distribution and coin tossing”. In: *Theoretical Computer Science* 560 (1984), p. 175–179.

[24] A.K. Ekert. “Quantum cryptography based on Bell’s theorem”. In: *Phys. Rev. Lett.* 67 (1991), p. 661–663.

[25] T. Gehring et al. “Implementation of continuous-variable quantum key distribution with composable and one-sided-device-independent security against coherent attacks”. In: *Nat Commun* 6 (2015), p. 8795.

[26] D. Abdelkhalek et al. “Efficient entanglement distillation without quantum memory”. In: *Nat Commun* 7 (2016), p. 11720.

[27] H.-A. Bachor and T. C. Ralph. *Basic Optical Components, in A Guide to Experiments in Quantum Optics*. 2. edition. Wiley-VCH Verlag GmbH, Weinheim, Germany, 2004.

[28] U. Leonhardt. *Measureing the Quantum State of Light*. 1. edition. Campridge Univ. Press, 1997.

[29] D.F. Walls and G.J. Milburn. *Quantum Optics*. 2. edition. Springer, 2008.

[30] J. R. Johansson, P. D. Nation, and F. Nori. "QuTiP: An open-source Python framework for the dynamics of open quantum systems". In: *Comp. Phys. Comm.* 183 (2012), p. 1760–1772.

[31] J. R. Johansson, P. D. Nation, and F. Nori. "QuTiP 2: A Python framework for the dynamics of open quantum systems". In: *Comp. Phys. Comm.* 184 (2013), p. 1234–1240.

[32] E. Wigner. "On the Quantum Correction For Thermodynamic Equilibrium". In: *Phys. Rev.* 40 (1932), p. 749–759.

[33] C. Baune. *Frequency up-conversion of nonclassical states of light*. Doctoral thesis, Leibniz Universität Hannover, 2016.

[34] J. Bauchrowitz, T. Westphal, and R. Schnabel. "A graphical description of optical parametric generation of squeezed states of light". In: *American Journal of Physics* 81 (2013), p. 767–771.

[35] R. Schnabel. "Squeezed states of light and their applications in laser interferometers". In: *Physics Reports* 684 (2017), p. 1–51.

[36] R.W. Boyd. *Nonlinear Optics*. 3. edition. Academic Press, 2008.

[37] S. Steinlechner. *Quantum metrology with squeezed and entangled light for the detection of gravitational waves*. Doctoral thesis, Leibniz Universität Hannover, 2013.

[38] M.M. Fejer et al. "Quasi-phase-matched second harmonic generation: tuning and tolerances". In: *IEEE Journal of Quantum Electronics* 28 (1992), p. 2631–2654.

[39] J.S. Neergaard-Nielsen. *Generation of single photons and Schrödinger kitten states of light*. Doctoral thesis, University of Copenhagen, 2008.

[40] F. Pein. *Wigner functions of Schrödinger's kitten states from 8-port homodyne detection*. Master thesis, Universität Hamburg, 2021.

[41] Laser Components. *Single Photon Counting Module COUNT NIR Series*. Datasheet, 2017-07.

[42] M. Diepold et al. "Improved X-ray detection and particle identification with avalanche photodiodes". In: *Rev. Sci. Instrum.* 86 (2015), p. 053102.

[43] R.H. Hadfield. "Single-photon detectors for optical quantum information applications". In: *Nature Photon* 3 (2009), p. 696–705.

[44] C.M. Natarajan, M.G. Tanner, and R.H. Hadfield. "Superconducting nanowire single-photon detectors: physics and applications". In: *Supercond. Sci. Technol.* 25 (2012), p. 063001.

[45] D. Abdelkhalek. *Efficient entanglement distillation based on emulation*. Doctoral thesis, Leibniz Universität Hannover, 2017.

[46] J. Göttsch. *Setup of a squeezed light source and its characterisation by 8-port homodyne detection*. Master thesis, Universität Hamburg, 2017.

[47] M. Faden. *Optimierung einer Quetschlichtquelle*. Bachelor thesis, Universität Hamburg, 2019.

[48] M. Lautzas. *Phase-stabilised eight-port homodyne detection for hybrid quantum experiments*. Master thesis, Universität Hamburg, 2021.

[49] B. Hage. *Purification and Distillation of Continuous Variable Entanglement*. Doctoral thesis, Leibniz Universität Hannover, 2010.

[50] E.D. Black. "An introduction to Pound–Drever–Hall laser frequency stabilization". In: *American Journal of Physics* 69 (2001), p. 79–87.

[51] A. Schönbeck. *Compact squeezed-light source at 1550 nm*. Doctoral thesis, Universität Hamburg, 2018.

[52] T. Eberle et al. "Strong Einstein-Podolsky-Rosen entanglement from a single squeezed light source". In: *Phys. Rev. A* 83 (2011), p. 052329.

[53] J. DiGuglielmo et al. "Experimental characterization of Gaussian quantum-communication channels". In: *Phys. Rev. A* 76 (2007), p. 012323.

[54] C. Baune et al. "Unconditional entanglement interface for quantum networks". In: *Phys. Rev. A* 93 (2016), p. 010302.

[55] K. McKenzie et al. "Quantum noise locking". In: *J. Opt. B: Quantum Semiclass. Opt.* 7 (2005), p. 421–428.

[56] J.M. Hörsch. *Characterisation of photon counters at 1064nm*. Bachelor thesis, Universität Hamburg, 2018.

[57] Excelitas Technologies. *SPCM-AQRH Single Photon Counting Module*. Datasheet, 2020-08.

[58] MPD. *PDM-IR 900 nm – 1700 nm Infrared Photon Detection Module*. Datasheet, 2019-09.

[59] S.A. Grebien. *8-port homodyne detection of Schrödinger kitten states of light*. Master thesis, Universität Hamburg, 2021.

[60] A. Schönbeck. *Hochkonversion von einzelnen Photonen im nichtklassischen Regime*. Master thesis, Leibniz Universität Hannover, 2014.

[61] Teledyne SP Devices. *ADQ32 Datasheet*. Datasheet, 2021-06-04.

[62] K. Banaszek et al. "Maximum-likelihood estimation of the density matrix". In: *Phys. Rev. A* 61 (1999), p. 010304.

[63] Single Quantum. *Single Quantum Eos SNSPD Closed-Cycle System*. Datasheet, 2018-08.

[64] H. Vahlbruch et al. "Detection of 15 dB Squeezed States of Light and their Application for the Absolute Calibration of Photoelectric Quantum Efficiency". In: *Phys. Rev. Lett.* 117 (2016), p. 110801.

[65] J. Gniesmer. *Advanced Techniques for Squeezed-Light-Enhanced Gravitational-Wave Detection*. Doctoral thesis, Leibniz Universität Hannover, 2019.

[66] G. Giedke and J.I. Cirac. "Characterization of Gaussian operations and distillation of Gaussian states". In: *Phys. Rev. A* 66 (2002), p. 032316.

[67] J. Fiurášek. "Gaussian Transformations and Distillation of Entangled Gaussian States". In: *Phys. Rev. Lett.* 89 (2002), p. 137904.

[68] J. Eisert, S. Scheel, and M. B. Plenio. "Distilling Gaussian States with Gaussian Operations is Impossible". In: *Phys. Rev. Lett.* 89 (2002), p. 137903.

[69] B. Hage et al. "On the distillation and purification of phase-diffused squeezed states". In: *New J. Phys.* 9 (2007), p. 227.

[70] A. Franzen. *Präparation von destillierten und purifizierten gequetschten Zuständen*. Doctoral thesis, Leibniz Universität Hannover, 2008.

[71] T. Eberle, V. Händchen, and R. Schnabel. "Stable control of 10 dB two-mode squeezed vacuum states of light". In: *Optics Express* 21 (2013), p. 11546–11553.

Acknowledgements

A big thanks goes to Roman Schnabel for supervising this thesis and giving me the opportunity to do a doctoral thesis. I want to thank Daniela and Lorena who supervised my master thesis and taught me a lot of things in the experimental lab work and gave me a good basis for the implementation of the Schrödinger kitten state experiment.

Also, a big thanks goes out to all the students who did their master (Malte, Stephan and Felix) or bachelor (Julian and Maximilian) theses on my experiment and gave me a lot assistance for the realization of the project. Further people who contributed to the realization of the project are Boris Hage who borrowed us the amazing superconducting nanowire detector and Jaromír Fiurásek who did the post processing for us. Thank you! Without your help the results in this thesis would not exist.

Thanks to the Deutsche Forschungsgemeinschaft for financing this project and thanks to Henning Moritz for doing the 2. survey of this thesis. I want to thank Dieter for all his help in electronic topics. Thanks to the PHYSnet for helping us with the data storage. And of course, a big thank you to the whole Non-linear quantum optics working group for all your help to realize my project and for the nice and funny time over the last years.

Resources

Following resources were used to create this thesis:
Calculations of the mode matchings were done with *JamMt* written by Nico Lastzka.
Pictures were drawn with *Inkscape* or *Microsoft Power Point*. A *component library* written by Alexander Franzen and Jan Südbeck was used.
Most of the data evaluation were done with *Python* by using the *Anaconda Navigator*. Additionally, *gnuplot* and *Microsoft Excel* were used sometimes. Most of the scripts were written by my master students (Malte Lautzas, Stephan Grebien and Felix Pein). Additionally, scripts from other group members and former group members of the "Non-linear quantum optics" group were used.
List of used Python packages: *numpy*, *pandas*, *matplotlib.pyplot*, *scipy.stats*, *qutip*, *mpltoolkits.mplot3d*, *openqlab*, *uncertainties*, *time*.
The editor *ConText* was used to run the gnuplot scripts.
The post processing was done by Jaromír Fiurásek in *MATLAB*.
The superconducting nanowire detector was borrowed from Boris Hage of the University of Rostock. It contained a laptop to control the detector with following software: *freezecontrol2.1.7d.rostock-qo* and *biascontrol1.0.3.rostock-qo*.
The PDM IR detector contained a control software: *VisualPDM-IR (x64)*.
The signal generator boxes (AD9959) are controlled with the software *AD9959 USB control v1.1*.
The thesis was written with LaTeX. Additionally, *TeXstudio* and *MiKTeX Console 4.0* were used. A template from:
"https://www.latextemplates.com/template/masters-doctoral-thesis"
was taken (10.09.2020).
For literature archiving *Mendeley* was used.
For technical drawings of mechanical components *Inventor* was used.
Finesse was used for simulating the filter cavities.
For testing data acquisition and digital cavity locking *LabVIEW* was used.
The first cat states were measured with a data acquisition card from Signatec *PX14400A*, which contains a software *PX14400/PX12500 Scope Application Version 2.7*.

For the final data acquisition a data acquisition card from Teledyne SP Devices *ADQ32* was used. Stephan Grebien wrote a control software in *C*, which is based on the *ADQAPI* from the manufacturer.
For data storage the *PHYSnet* implemented storage blocks.
For characterizing a laser beam different beam profiler from Thorlabs were used with the software *Thorlabs Beam 7.0*.
A lot of electronic components which were built from former group members of the "Non-linear quantum optics" group were used.
For lab book documentation *Confluence* was used.

Eidesstattliche Versicherung / Declaration on oath

Hiermit versichere ich an Eides statt, die vorliegende Dissertationsschrift selbst verfasst und keine anderen als die angegebenen Hilfsmittel und Quellen benutzt zu haben.

Hamburg, den 13.01.2022

Unterschrift des Doktoranden